

# SUPERFLUID ${}^3\text{He}$ : A LABORATORY MODEL SYSTEM FOR QUANTUM FIELD THEORY\*

V. B. Eltsov

*Low Temperature Laboratory, Helsinki University of Technology, Box 2200, FIN-02015 HUT, Finland  
and P. L. Kapitza Institute for Physical Problems, 117334 Moscow, Russia*

M. Krusius

*Low Temperature Laboratory, Helsinki University of Technology, Box 2200, FIN-02015 HUT, Finland*

G. E. Volovik

*Low Temperature Laboratory, Helsinki University of Technology, Box 2200, FIN-02015 HUT, Finland  
and L. D. Landau Institute for Theoretical Physics, 117334 Moscow, Russia*

The early Universe is believed to have undergone a sequence of rapid phase transitions. Defect formation in these transitions has been suggested as one possible source for the anisotropy in the cosmic background radiation and the large-scale structure in the distribution of visible mass. So far controlled laboratory experiments have not been performed on homogeneous second order phase transitions as a function of transition speed and a freeze-out of topological defects has not been convincingly demonstrated. Recently a new phenomenon was discovered in superfluid  ${}^3\text{He}$ -B: the formation of quantized vortices within bulk liquid in the presence of ionizing radiation. This “mini bang” allows one to explore the superfluid transition within the clean bulk medium on the microsecond time scale. Such experiments appear to provide the first quantitative test of the theories on defect formation in a time-dependent second order phase transition. Also other superfluid  ${}^3\text{He}$  experiments can be found which establish analogies to phenomena in high energy physics, such as baryogenesis by strings and by textures, and generation of primordial magnetic fields. Here and in most other cases it is quantized vortex lines and other topological defects which provide a connection to quantum field theory and its applications in cosmology. Their analogies in relativistic quantum field theory include such objects as  $Z$  and  $W$  cosmic strings, Alice strings, torsion and spinning strings, strings terminating on walls and walls terminating on strings, gravimagnetic monopoles, axion and pion strings, etc.

arXiv:cond-mat/9809125v3 [cond-mat.other] 3 Oct 2000

---

\*Figures are of reduced quality. See <ftp://boojum.hut.fi/pub/ve/review.pdf> for the full quality figures.

## CONTENTS

1. Superfluid $^3\text{He}$ and quantum field theory	4
2. Quench-cooled superfluid transition: a model of defect formation in non-equilibrium phase transitions	4
2.1. Rapid phase transitions	4
2.2. Cosmic large-scale structure	5
2.3. Kibble-Zurek mechanism	5
2.4. Experimental verification of KZ mechanism	6
2.5. Principle of superfluid $^3\text{He}$ experiments	7
2.5.1. Outline of experimental method	8
2.5.2. Interpretation of $^3\text{He}$ experiments	8
2.6. Measurement of vortex lines in $^3\text{He-B}$	9
2.6.1. Critical velocity for vortex formation	9
2.6.2. Rotating states of the superfluid	10
2.6.3. NMR measurement	11
2.7. Vortex formation in neutron irradiation	12
2.8. Threshold velocity for vortex loop escape	14
2.8.1. Properties of threshold velocity	15
2.8.2. Superflow instability vs KZ mechanism	15
2.8.3. Influence of $^3\text{He-A}$ on threshold velocity	16
2.9. Other defect structures formed in neutron irradiation	17
2.9.1. Radiation-induced supercooled $A \rightarrow B$ transition	17
2.9.2. $A \rightarrow B$ transition via KZ mechanism	17
2.9.3. Threshold velocity, AB interfaces, and the KZ mechanism	19
2.9.4. Spin-mass vortex	19
2.10. Vortex formation in gamma radiation	22
2.11. Bias dependence of loop extraction	22
2.11.1. Experimental velocity dependence	22
2.11.2. Analytic model of vortex loop escape	23
2.12. Calorimetry of vortex network	25
2.13. Simulation of loop extraction	27
2.13.1. Initial loop distribution	27
2.13.2. Network evolution under scaling assumptions	29
2.13.3. Direct simulation of network evolution	30
2.14. Superfluid transition as a moving phase front	32
2.14.1. Neutron absorption and heating	33
2.14.2. Thermal gradient and velocity of phase front	34
2.15. Quench of infinite vortex tangle	35
2.15.1. Vorticity on microscopic and macroscopic scales	35
2.15.2. Scaling in equilibrium phase transitions	36
2.15.3. Non-equilibrium phase transitions	37
2.16. Implications of the quench-cooled experiments	37
3. Other $^3\text{He}$ – quantum field theory analogues involving topological defects	38
3.1. Three topological forces acting on a vortex and their analogues	38
3.2. Iordanskii force	39
3.2.1. Superfluid vortex vs spinning cosmic string	39
3.2.2. Gravitational Aharonov-Bohm effect	40
3.2.3. Asymmetric cross section of scattering on a vortex	41
3.2.4. Iordanskii force: vortex and spinning string	41
3.3. Spectral flow force and chiral anomaly	42
3.3.1. Chiral anomaly	42
3.3.2. Anomalous force acting on a continuous vortex and baryogenesis from textures	44
3.3.3. Anomalous force acting on a singular vortex and baryogenesis with strings	45
3.4. Analog of magnetogenesis: vortex textures generated by normal-superfluid counterflow	47
3.5. Vortex mass: chiral fermions in strong magnetic field	49
3.5.1. “Relativistic” mass of the vortex	49
3.5.2. Bound states contribution to the mass of singular vortex	49
3.5.3. Kopnin mass of continuous vortex: connection to chiral fermions in magnetic field.	50
3.5.4. Associated hydrodynamic mass	51
4. Vortices in $^3\text{He}$ and their analogues in high energy physics	52
4.1. Vortices in $^3\text{He-B}$	53
4.1.1. Symmetry breaking in $^3\text{He-B}$ and analogous phases in high energy physics	53
4.1.2. Mass vortex vs axion string	53

4.1.3.	Spin vortex vs pion string	54
4.1.4.	Spin vortex as domain wall bounded by string	54
4.1.5.	Nonaxisymmetric vortex vs Witten superconducting string	54
4.2.	Vortices in $^3\text{He-A}$	54
4.2.1.	Symmetry breaking in $^3\text{He-A}$ and analogous phases in high energy physics	54
4.2.2.	Chiral fermions	55
4.2.3.	Topological classification	55
4.2.4.	Z and W strings	55
4.2.5.	Alice string – half-quantum vortex	56
4.2.6.	Torsion string	57
4.2.7.	Spinning string	57
4.2.8.	Disgyration as negative-mass string	57
4.2.9.	Continuous vortices — textures	57
4.2.10.	Vortex sheet	58
4.2.11.	Strings terminating on walls	59
4.2.12.	Gravimagnetic monopole	59
5.	Conclusion	60
	Acknowledgements	60
	References	60

## 1. SUPERFLUID $^3\text{He}$ AND QUANTUM FIELD THEORY

In recent times condensed matter and elementary particle physics have been experiencing remarkable convergence in their developments, as many-body aspects have become increasingly more important in particle physics: The Early Universe is the ultimate testing ground where theories on interacting particle systems can be worked out for different energy regimes, or epochs of the expansion after the Big Bang. Compact astro-physical objects provide other “laboratories” with a narrower range of conditions in which to test theories. Finally actual collider experiments are being set up to study interacting particle systems, such as the quark-gluon plasma in heavy ion collisions or the pion condensate.

Collective phenomena in interacting many-body systems is of course what condensed matter physics is about, but elementary particle systems are adding to the picture extreme quantum behavior plus relativistic motion. So far systems, where both of these features would be of importance, are not available in the laboratory. During the last few years it has turned out that valuable analogues can nevertheless be constructed from comparisons with non-relativistic quantum systems of the condensed matter. The best examples of stable coherent quantum systems are the superfluids and superconductors. Lately the optically cooled bosonic alkali atom clouds have been added to this list. In their degenerate states, the various forms of Bose-Einstein condensates, the first vortex structures have now been discovered. Among these systems the largest variety of topological defects have so far been identified in the different superfluid phases of liquid  $^3\text{He}$ .

The liquid  $^3\text{He}$  phases provide attractive advantages as a model system for the study of various general concepts in quantum field theory: The liquid is composed of neutral particles in an inherently isotropic environment — no complications arise from electrical charges or a symmetry constrained by a crystalline lattice. This allows one to concentrate on the consequences from a most complex symmetry breaking, which gives rise to a multi-dimensional order parameter space, but is well described by a detailed microscopic theory. Experimentally the  $^3\text{He}$  superfluids are devoid of extrinsic imperfections. In fact, with respect to external impurities or defects they are the purest of all condensed matter systems. The superfluid coherence length is large such that even surface roughness can be reduced sufficiently to transform the container walls to almost ideally behaving boundaries. Phase transitions of both first and second order exist, which can be utilized for the investigation of defect formation. There are topologically stable defects of different dimensionality and type, which often can be detected with NMR methods with single-defect sensitivity.

Reliable observational input in cosmology is still in

short supply. Connections to laboratory systems have received renewed interest since here questions concerning basic principles might be answered. A good example are the different intrinsic mechanisms by which defects can be formed in a coherent quantum system, such as a superfluid. Another important aspect has been the use of superfluid  $^3\text{He}$  to model the complicated physical vacuum of quantum field theory — the modern ether. The bosonic and fermionic excitations in  $^3\text{He}$  are in many respects similar to the excitations of the physical vacuum — the elementary particles. This approach has been quite successful in constructing a physical picture of the interactions of elementary particles with strings and domain walls.

This review attempts to illustrate to what extent general physical principles of quantum field theory can be verified from analogues, constructed on the basis of measurements and calculations on  $^3\text{He}$  superfluids. The review has been split in two parts: The first part deals with a detailed description of defect formation and evolution in a rapidly quenched second-order phase transition. The second part gives a unified, but less detailed account of several other examples where analogues to  $^3\text{He}$  superfluids seem to provide useful answers.

## 2. QUENCH-COOLED SUPERFLUID TRANSITION: A MODEL OF DEFECT FORMATION IN NON-EQUILIBRIUM PHASE TRANSITIONS

### 2.1. Rapid phase transitions

A rapid phase transition is generally associated with a large degree of inhomogeneity. After all, this is the process by which materials like steel or amorphous solids are prepared. This disorder we attribute to heterogeneous extrinsic influence which is usually present in any system which we study: impurities, grain boundaries, and other defects depending on the particular system. To avoid disorder and domain formation, we generally examine phase transitions in the adiabatic limit, as close to equilibrium as possible. But suppose we had an ideally homogeneous infinite system with no boundaries. It is rapidly cooling from a symmetric high temperature state to a low temperature phase of lower symmetry, which we call the broken-symmetry phase, for example by uniform expansion. What would happen in such a transition? Are defects also formed in this case?

Such a measurement, as a function of the transition speed, is difficult and has not been carried out in the laboratory so far. Nevertheless, if we believe the standard theory of cosmology then one experiment exists and we might anticipate an answer from there. In the “Big Bang” the Universe started off in a homogeneous state. It then rapidly cooled through a sequence of phase transitions, in which the four fundamental forces of nature

separated out. We know today that the Universe must have settled down in an inhomogeneous state with large-scale structure.

## 2.2. Cosmic large-scale structure

The clumped distribution of the visible mass in the Universe has become evident from galaxy surveys — maps which show that galaxies form clusters and these in turn super clusters, such as the “Great Wall”, which are the largest structures discovered to date (Geller and Huchra 1989). The clustering takes the form of long chains or filaments, which are separated by large voids, regions empty of visible mass. It is not yet known how these filaments are organized — whether they form a random network or are ordered in a more regular pattern. Recent extended galaxy surveys could indicate that there exists a repeating length scale, the separation between filaments, which is on the scale of 100 Mpc or more<sup>1</sup> (Einasto et al. 1997).

Another image of large-scale structure has been preserved in the cosmic microwave background radiation, from the time when the Universe had cooled to a few eV, when nuclei and electrons combined to form atoms and the Universe became transparent to photons. Since then the background radiation has cooled in the expanding Universe. It now matches to within 3 parts in 10<sup>5</sup> the spectrum of a black body at 2.728 K, as measured with the Far InfraRed Absolute Spectrometer (FIRAS) on board of the satellite Cosmic Background Explorer (COBE) in 1990. A second instrument on COBE, the Differential Microwave Radiometer (DMR), revealed in 1992 that the background radiation shows a spatial variation, an anisotropy of 30  $\mu$ K in amplitude, when probed with an angular resolution of 7°. The anisotropy represents the density fluctuations in the structure of the Universe when it was only 300 000 years old and, although small, it might eventually explain what seeded the large-scale structure visible today. Cosmic background radiation is one of the few observational foundations of the standard theory of cosmology. Both balloon and satellite missions with high angular resolution and amplitude sensitivity are planned to provide extended surveys of the anisotropy.

## 2.3. Kibble-Zurek mechanism

One possible source for the large-scale structure and the anisotropy of cosmic background radiation is thought

to be the inhomogeneity which was created in the non-equilibrium phase transitions of the Early Universe. In 1976 Tom Kibble proposed that even in a perfectly homogeneous phase transition of second order defects will form, if the transition proceeds faster than the order parameter of the broken-symmetry phase is able to relax (Kibble 1976). In such a non-equilibrium transition the new low-temperature phase starts to form, due to fluctuations of the order parameter, simultaneously and independently in many parts of the system. Subsequently during further cooling, these regions grow together to form the new broken-symmetry phase. At the boundaries, where different causally disconnected regions meet, the order parameter does not necessarily match and a domain structure is formed.

If the broken symmetry is the U(1) gauge symmetry, then domains with a random phase of the order parameter are formed. Such a domain structure reduces to a network of linear defects, which are vortex lines in superfluids and superconductors or perhaps cosmic strings in the Early Universe. If the symmetry break is more complicated, as is the case in the <sup>3</sup>He superfluids, then defects of different dimensionality and structure may be formed.

Indeed, numerical simulations of a rapid quench through a second order phase transition indicated that defects seemed to form. In 1985 Wojciech Zurek proposed a conceptually powerful phenomenological approach how to understand a phase transition far out of equilibrium, when the outcome from the transition becomes time dependent (Zurek 1985, 1996). He characterizes the transition speed with a quench time

$$\tau_Q = \left( \frac{1}{T_c} \left| \frac{dT}{dt} \right|_{T=T_c} \right)^{-1}, \quad (1)$$

which allows him to approximate temperature and time with a linear dependence during the thermal quench.

The quench time  $\tau_Q$  is compared to the order parameter relaxation time  $\tau$ , which in a Ginzburg-Landau system at a second order phase transition is of the general form

$$\tau(T) = \tau_0(1 - T/T_c)^{-1}. \quad (2)$$

In superfluid <sup>3</sup>He,  $\tau_0$  is on the order of  $\tau_0 \sim \xi_0/v_F$ , where  $\xi_0$  is the zero temperature limiting value of the temperature ( $T$ ) and pressure ( $P$ ) dependent superfluid coherence length  $\xi(T, P)$ . Close to  $T_c$ , it is of the form  $\xi(T, P) = \xi_0(P)(1 - T/T_c)^{-1/2}$ . The second quantity,  $v_F$ , is the velocity of the thermal quasiparticle excitations which are excited above the superfluid energy gap.

As sketched in Fig. 1, this means that below  $T_c$  the order parameter coherence spreads out with the velocity  $c(T) \sim \xi/\tau = \xi_0(1 - T/T_c)^{1/2}/\tau_0$ . The freeze-out of

---

<sup>1</sup>1 Mpc = 10<sup>6</sup> parsec = 3.262·10<sup>6</sup> light years.

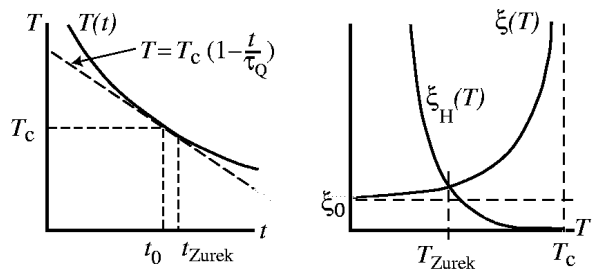


FIG. 1. Principle of KZ mechanism. Rapid thermal quench below  $T_c$ : (Left) Temperature  $T(t)$  and its linear approximation  $T = T_c(1 - t/\tau_Q)$  during the quench, as a function of time  $t$ . (Right) Superfluid coherence length  $\xi(T)$  and order parameter relaxation time  $\tau(T)$  diverge at  $T_c$ . At the freeze-out point  $t_{\text{Zurek}}$ , when phase equilibrium is achieved, the edge of the correlated region, the causal horizon, has moved out to a distance  $\xi_H(t_{\text{Zurek}})$ , which has to equal the coherence length  $\xi(t_{\text{Zurek}})$ .

defects occurs at  $t = t_{\text{Zurek}}$ , when the causally disconnected regions have grown together and superfluid coherence becomes established in the whole volume. At the freeze-out temperature  $T(t_{\text{Zurek}}) < T_c$ , the causal horizon has travelled the distance  $\xi_H(t_{\text{Zurek}}) = \int_0^{t_{\text{Zurek}}} c(T) dt = \xi_0 \tau_Q (1 - T_{\text{Zurek}}/T_c)^{3/2} / \tau_0$  which has to be equal to the coherence length  $\xi(t_{\text{Zurek}})$ . This condition establishes the freeze-out temperature  $T_{\text{Zurek}}/T_c = 1 - \sqrt{\tau_0/\tau_Q}$  at the freeze-out time  $t_{\text{Zurek}} = \sqrt{\tau_0 \tau_Q}$ , when the domain size has reached the value

$$\xi_v = \xi_H(t_{\text{Zurek}}) = \xi_0 (\tau_Q/\tau_0)^{1/4}. \quad (3)$$

In superfluid  $^3\text{He}$  we may have  $\xi_0 \sim 20$  nm,  $\tau_0 \sim 1$  ns, and in the best cases a cool-down time of  $\tau_Q \sim 1$   $\mu\text{s}$  can be reached. From these values we expect the domain structure to display a characteristic length scale of order  $\xi_v \sim 0.1$   $\mu\text{m}$ . In a U(1)-symmetry-breaking transition, vortex lines are formed at the domain boundaries: This leads to a whole network of randomly organized vortices, where the average inter-vortex distance and radius of curvature are on the order of the domain size  $\xi_v$ . In general, we can expect a rapid quench to lead to a defect density (defined as vortex length per unit volume)

$$l_v = \frac{1}{a_l \xi_v^2}, \quad (4)$$

where the numerical factor  $a_l \sim 1-10$  depends on the details of the model system. Numerical simulation calculations (Ruutu et al. 1998a) give  $a_l \approx 2$  for  $^3\text{He-B}$ . Here Ginzburg-Landau theory provides a good description close to  $T_c$ .

## 2.4. Experimental verification of KZ mechanism

Defect formation in model systems via the Kibble-Zurek (KZ) process has been studied in numerous numerical simulations (Vachaspati and Vilenkin 1984; Hindmarsh and Kibble 1995a; Bray 1994). Generally these have been on 1- or 2-dimensional systems, but even 3-dimensional simulations now exist (Antunes et al. 1999). The results invariably fit the Zurek scaling model.

In real laboratory experiments the situation is more complicated. Although the KZ mechanism is intuitively easy to accept, in practice its experimental verification is a difficult task and involves many careful considerations. To start with, one has to accept that most experiments are flawed with a number of extrinsic sources for defect formation. In general defect formation in a phase transition is more usual than its absence. For instance, it has been shown that even slow cooling of liquid  $^4\text{He}$  across the  $\lambda$  transition produces primordial vortices which remain pinned as remanent vorticity at the walls of the container (Awschalom and Schwarz 1984). There are no claims in the literature yet that any experiment would have produced a perfectly vortex-free bulk sample of superfluid  $^4\text{He}$ .

A second point to note is that the KZ model describes a second order transition where the energy barrier, which separates the symmetric high-temperature phase from the broken-symmetry states at low-temperatures, vanishes at  $T_c$ . Thus the transition becomes an instability. A first order transition is different: Here the barrier remains finite and the low temperature phase has to be nucleated, usually by overcoming the barrier via thermal activation. Nucleation may occur in different parts of the system nearly simultaneously, depending on the properties of the system, the quench time  $\tau_Q$ , and the nucleation mechanism. Such a situation, which often is simply called bubble nucleation, also leads to domain formation and to a final state which is qualitatively similar to that expected after the second order transition and the KZ mechanism.

The original KZ theory describes a homogeneous transition which occurs simultaneously in the whole system, ie. there are no gradients in density or temperature, for instance. However, a rapid quench through the transition is generally forced by strong gradients. On some level gradients will always appear in any laboratory system and their influence has to be investigated.

The first experiments were performed on liquid crystals (Chuang et al. 1991; Bowick et al. 1994), where the transition from the isotropic to the nematic phase was examined. This is a weakly first order transition of rod-like molecules from a disordered to an ordered state, where defects of different dimensionalities can be formed. The results were generally found to be consistent with the Kibble-Zurek interpretation. However, a liquid-crystal

transition at room temperature is rather different from the ideal KZ case, it does not lead into a coherent quantum state, and also it is not one of pure second order.

A second type of experiments was performed on liquid  $^4\text{He}$  (Dodd et al. 1998), by releasing the pressure on a convoluted phosphor-bronze bellows and expansion cooling the normal liquid through the  $\lambda$  transition into the superfluid phase. For a mechanical pressure system the quench time is of order  $\tau_Q \sim 10$  ms. The depressurization is followed by a dead time  $\sim 50$  ms, which is required for damping down the vibrations after the mechanical shock. The vortex density after the transition is determined from the attenuation in second sound propagation through bulk liquid. Expansion cooling of  $^4\text{He}$  across  $T_\lambda$  requires careful elimination of all residual flow which might result from the expansion itself, foremost the flow out of the filling capillary of the cell, but also that around the convolutions of the bellows. Such flow will inevitably exceed the critical velocities, which approach zero at  $T_\lambda$ , and leads to vortex nucleation (Sec. 2.6.1). After the initial attempts, where a fill line was still present, later improved measurements failed to yield any evidence of vortex line production, in apparent contradiction with the KZ prediction (Dodd et al. 1998).

The early  $^4\text{He}$  expansion experiments were analyzed by Gill and Kibble (1996) who concluded that the initially detected vortex densities were unreasonably large and must have originated from extrinsic effects. The absence of vorticity in the later results was concluded not to be evidence against the KZ mechanism (Karra and Rivers 1998; Rivers 2000): Although the pressure drop in expansion cooling is large, 20 – 30 bar, the change in relative temperature  $\epsilon = 1 - T/T_\lambda$  is small,  $|\Delta\epsilon| < 0.1$ . The final temperature  $\epsilon_f < 0.06$  is thus below  $T_\lambda$  but still above the Ginzburg temperature  $T_G$ , ie. in the region where thermal fluctuations might be sufficiently effective to wipe out domain formation.  $T_G$  is defined as the temperature at which  $k_B T_G$  equals the energy of a vortex loop of the size  $\xi_v$ , which is expected after the quench according to Eq. (3).

The first measurements have also been reported on trapped flux in superconducting rings which have been rapidly heated above  $T_c$  and then quench cooled back into the superconducting state. According to the KZ scenario one will here find from one quench to the next a varying number of flux quanta which remain trapped in the ring (Zurek 1985). Preferably such rings are fabricated from thin films, to reduce the heat capacity and the thermal relaxation time. Also one either uses a grid of loops or prepares the loop from many segments separated by Josephson junctions, to amplify the total trapped flux. The first positive results are reported on a loop from high- $T_c$  film, which consists of a series connection of 214 grain-boundary junctions and in zero external field displays a Gaussian distribution of trapped flux with a stan-

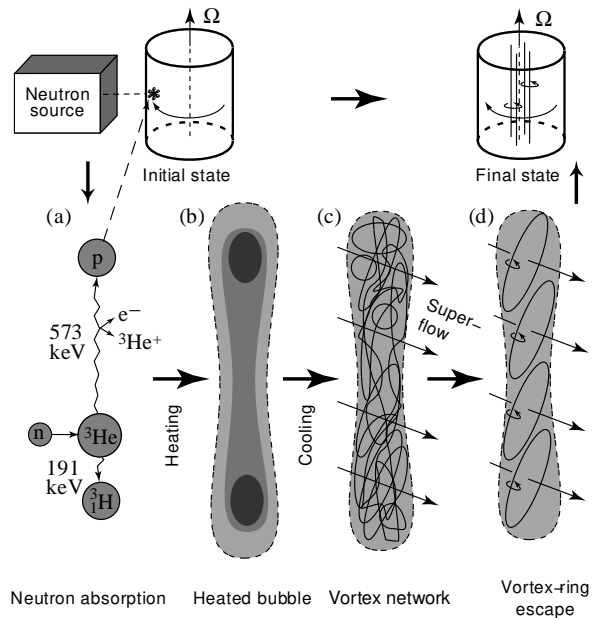


FIG. 2. Principle of the quench-cooled rotating experiment in superfluid  $^3\text{He-B}$ : (Top) A cylindrical sample container with superfluid  $^3\text{He-B}$  is rotated at constant angular velocity  $\Omega$  and temperature  $T$ , while the NMR absorption is monitored continuously. When the sample is irradiated with neutrons, vortex lines are observed to form. (Bottom) Interpretation of the processes following a neutron absorption event in bulk superflow; see the text for details. (From Ruutu et al. 1996a).

dard deviation of 7 quanta (Carmi et al. 2000).

A quantitative comparison of measurement to the KZ mechanism has been achieved with superfluid  $^3\text{He}$  (Ruutu et al. 1996a,b, 1998a; Bäuerle et al. 1996, 1998a). A happy coincidence of many valuable features has made this possible: A reduced likelihood of defect formation from extrinsic sources and the virtual absence of remanent vorticity, the possibility to perform thermal quenches in microseconds, the presence of a pure second order phase transition, and the availability of measuring methods to detect different types of defects, often with a resolution of one single defect.

## 2.5. Principle of superfluid $^3\text{He}$ experiments

To study reliably defect formation in a quench-cooled transition, two basic requirements are the following: First, the transition can be repeated reproducibly, and second, a measurement is required to detect the defects after their formation, either before they annihilate or by stabilizing their presence with a bias field. Both of these requirements can be satisfied in  $^3\text{He}$  experiments.

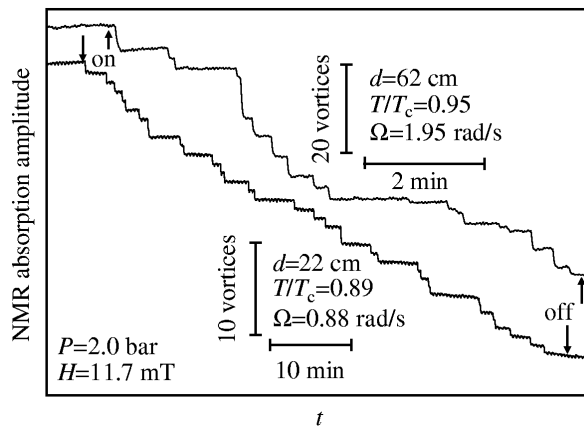


FIG. 3. Peak height of the counterflow absorption maximum in the NMR absorption spectrum of  $^3\text{He-B}$ , shown as a function of time  $t$  during neutron irradiation. The *lower trace* is for a low and the *upper trace* for a high value of rotation velocity  $\Omega$ . The initial state in both cases is metastable vortex-free counterflow. The vertical arrows indicate when the neutron source was turned on/off. Each step corresponds to one neutron absorption event and its height, when compared to the adjacent vertical calibration bar, gives the number of vortex lines formed per event. The distance of the neutron source from the sample is denoted with  $d$ . (From Ruutu et al. 1996b).

### 2.5.1. Outline of experimental method

A schematic illustration of one set of experiments (Ruutu et al. 1996a) is depicted in Fig. 2. The top part displays the events which are controlled by the observer in the laboratory. A cylindrical container filled with superfluid  $^3\text{He-B}$  is rotated at constant velocity  $\Omega$ . The velocity of rotation is maintained below the critical value at which quantized vortex lines are spontaneously formed. In other words, the initial state is one of metastable vortex-free counterflow under constant conditions.

Next a weak source of slow thermal neutrons is placed in the vicinity of the  $^3\text{He}$  sample. If the rotation velocity is sufficiently high, then vortices start to appear at a rate which is proportional to the neutron flux. The neutron source is positioned at a convenient distance  $d$  from the cryostat so that vortex lines are observed to form in well-resolved individual events. The experimental signal for the appearance of a new vortex line is an abrupt jump in NMR absorption. An example, measured at low rotation, is shown by the lower recorder trace in Fig. 3.

The lower part of Fig. 2 shows in more detail what is thought to happen within the superfluid. Liquid  $^3\text{He}$  can be locally heated by the absorption reaction of a thermal neutron:  $n + ^3_2\text{He} \rightarrow p + ^3_1\text{H} + E_0$ , where  $E_0 = 764$  keV. The reaction products, a proton and a triton, are stopped by the liquid and produce two collinear ionization tracks (Meyer and Sloan 1997). The ionized particles, electrons and  $^3\text{He}$  ions, diffuse in the liquid to recom-

bine such that 80 % or more of  $E_0$  is spent to heat a small volume with a radius  $R_b \sim 50 \mu\text{m}$  from the superfluid into the normal phase. The rest of the reaction energy escapes in the form of ultraviolet emission (Stockton et al. 1971; Adams et al. 1995) and, possibly, in the form of long-living molecular  $^3\text{He}_2^*$  excitations (Keto et al. 1974; Eltsov et al. 1998), which partially relax at the walls of the container.

For measurements in rotating  $^3\text{He}$ , neutron absorption is an ideal heating process: The large absorption cross section for slow neutrons ( $5500 \text{ barn} = 5.5 \cdot 10^{-21} \text{ cm}^2$ ) corresponds to a mean free path of about  $100 \mu\text{m}$  and thus most neutrons are absorbed within a close distance from the wall. This means that the reactions occur within bulk liquid, but close to the cylindrical wall, such that the velocity of the applied counterflow is accurately specified. In other parts of the refrigerator neutron absorption is negligible and thus the temperature of the  $^3\text{He}$  sample can be maintained stable during the irradiation. Subsequently, the heated volume of normal liquid cools back through  $T_c$  in microseconds.

The measurements demonstrate (Fig. 3) that vortex lines are indeed created in a neutron absorption event. Vortex loops, which form within a cooling neutron bubble in the bulk superfluid, would normally contract and disappear in the absence of rotation. This decay is brought about by the intervortex interactions between the vortex filaments in the presence of dissipation from the mutual friction between the normal and superfluid components. In rotation the externally applied counterflow provides a bias which causes sufficiently large loops to expand to rectilinear vortex lines and thus maintains them for later detection. In the rotating experiments in Helsinki these rectilinear vortex lines are counted with NMR methods (Ruutu et al. 1996a).

In a second series of  $^3\text{He}$  experiments, performed in Grenoble (Bäuerle et al. 1996, 1998a) and Lancaster (Bradley et al. 1998), the vortices formed in a neutron absorption event are detected calorimetrically with very-low-temperature techniques. In the zero temperature limit mutual friction becomes vanishingly small and the life time of the vorticity very long. In this situation its existence can be resolved as a deficit in the energy balance of the neutron absorption reaction.

### 2.5.2. Interpretation of $^3\text{He}$ experiments

Several alternative suggestions can be offered on how to explain these observations. The KZ model is one of them. However, whatever the mechanism, the superfluid transition in a localized bubble represents an entirely new process for creating vortex rings. This phenomenon is associated with what appears to be the fastest 2nd order phase transition, which has been probed to date, and is

not restricted to the immediate vicinity of a solid wall, where most other vortex formation processes take place in the presence of applied counterflow.

The KZ interpretation of the later stages of the experiment is contained in the two illustrations marked as (c) and (d) in Fig. 2. It is based on studies of the number of vortex lines, which are formed per neutron absorption event, as a function of the various external variables and, foremost, as a function of the velocity of the applied counterflow. First a random vortex network (c) is created while cooling through  $T_c$ . Next the network starts to evolve under the influence of intervortex interactions and the applied counterflow. The evolution is dissipative due to the mutual friction force which connects the superfluid and normal fractions of the liquid and acts on a moving vortex. The average intervortex distance increases, small loops are smoothed out, and the network becomes rarefied or “coarse grained”. Also reconnections, which take place when two lines cross each other, contribute to the rarefaction. The applied counterflow favors the growth of loops with the right winding direction and orientation. It causes sufficiently large loops to expand, while others contract and disappear. A somewhat similar situation has been studied in the stationary state turbulent flow of superfluid  $^4\text{He}$  through a pipe (Schwarz 1978, 1985, 1988; Donnelly 1991). The final outcome is that correctly oriented loops (d), which exceed a critical threshold size, will start expanding spontaneously as vortex rings, until they meet the chamber walls. There the superfluid sections of the ring will annihilate and only a rectilinear vortex line will finally be left over. It is pulled to the center of the container, where it remains in stationary state parallel to the rotation axis, stretched between the top and bottom surfaces.

Very different time scales are at work in this process of vortex formation. Except for the retarded molecular excitations, the majority of the heating from the initial ionization and subsequent recombination takes place much faster than the thermal recovery. The initial vortex network forms during cooling through  $T_c$ , for which the relevant time scale is microseconds. The later evolution of the network and the loop escape happen again on a much slower time scale, which is governed by the mutual-friction-dependent superfluid hydrodynamics, with processes which take from milliseconds up to seconds to complete.

## 2.6. Measurement of vortex lines in $^3\text{He-B}$

There are two major phases of superfluid  $^3\text{He}$ , the A and B phases (Fig. 13). The neutron measurements have been performed in the quasi-isotropic  $^3\text{He-B}$ . In the present context we may think of vortices in  $^3\text{He-B}$  as being similar to those in superfluid  $^4\text{He-II}$ , where only

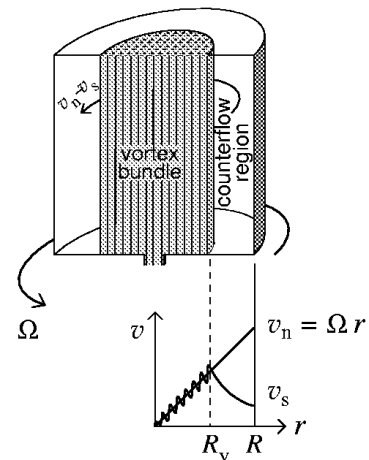


FIG. 4. (Top) Metastable state with a central vortex cluster in the rotating cylinder. This axially symmetric arrangement consists of rectilinear vortex lines surrounded by vortex-free counterflow. (Bottom) Radial distribution of the velocities of the superfluid component,  $v_s$ , and the normal component,  $v_n$ . Because of its large viscosity, the normal fraction corotates with the container. (From Krusius et al. 1994).

the U(1) symmetry is broken and the order parameter is of the general form  $\Psi = |\Psi(T)| e^{i\Phi(r)}$ : The vortices are topologically stable, have a singular core, inside of which  $|\Psi|$  deviates from its bulk value, while outside the phase  $\Phi$  changes by  $2\pi\nu$  on a closed path which encircles the core. A persistent superfluid current is trapped as a single-quantum circulation ( $\nu = 1$ ) around the core, with the circulation quantum  $\kappa = h/(2m_3) \simeq 0.0661 \text{ mm}^2/\text{s}$  and a superflow velocity  $\mathbf{v}_{s,\text{vortex}} = \kappa/(2\pi) \nabla\Phi = \kappa/(2\pi r) \hat{\phi}$ .

### 2.6.1. Critical velocity for vortex formation

The energy of one rectilinear vortex line, which is aligned along the symmetry axis of a rotating cylindrical container of radius  $R$  and height  $Z$ , consists primarily of the hydrodynamic kinetic energy stored in the superfluid circulation trapped around the core,

$$E_v = \frac{1}{2} \int \rho_s v_{s,\text{vortex}}^2 dV = \frac{\rho_s \kappa^2 Z}{4\pi} \ln \frac{R}{\xi} . \quad (5)$$

Here the logarithmic ultraviolet divergence has been cut off with the core radius, which has been approximated with the coherence length  $\xi$ . If the container rotates at an angular velocity  $\Omega$ , the state with the first vortex line becomes energetically preferred when the free energy  $E_v - \Omega L_z$  becomes negative. The hydrodynamic angular momentum from the superflow circulating around the vortex core is given by

$$L_z = \int \rho_s r v_{s,\text{vortex}} dV = \rho_s \kappa R^2 Z . \quad (6)$$

One finds that  $E_v - \Omega L_z < 0$ , when the velocity  $\Omega R$  of the cylinder wall exceeds the Feynman critical velocity,  $v_{c1} = \kappa/(2\pi R) \ln(R/\xi)$ . With a container radius  $R$  of a few mm, the Feynman velocity is only  $\sim 10^{-2}$  mm/s. However, if we can exclude remanent vorticity and other extrinsic mechanisms of vortex formation, which is generally the case in  $^3\text{He-B}$  (but not in  $^4\text{He-II}$ ), then vortex-free superflow will persist as a metastable state to much higher velocities because of the existence of a finite nucleation energy barrier.

The height of the nucleation barrier decreases with increasing velocity. In  $^4\text{He-II}$  intrinsic vortex formation is observed in superflow through submicron-size orifices. Here the barrier is ultimately at sufficiently high velocities overcome by thermal activation or at low temperatures by quantum tunnelling (Packard 1998; Varoquaux et al. 1998). In  $^3\text{He-B}$  the barrier is unpenetrably high in practically any situation and the flow velocity has to be increased to the point where the barrier approaches zero. Vortex formation then becomes possible in the form of an instability which takes place locally at some sharp asperity on the cylindrical wall where superflow first becomes unstable (Parts et al. 1995; Ruutu et al. 1997a). The average velocity, at which the instability occurs, we shall here call the container specific spontaneous critical velocity  $v_c(T, P)$  (Fig. 12). The actual local velocity at the asperity, the intrinsic container independent instability velocity  $v_{cb}(T, P)$ , can be considerably higher.

When the flow reaches the instability value  $v_{cb}$  at the asperity, a segment of a vortex ring is formed. The energy of the smallest possible vortex ring, which has a radius comparable to the coherence length, is of order  $E_v \sim \rho_s \kappa^2 \xi$ . This energy constitutes the nucleation barrier. On dimensional grounds we may estimate that  $E_v/(k_B T) \sim (\xi/a)(T_F/T)$ , where  $T_F = \hbar^2/(2m_3 a^2) \sim 1\text{K}$  is the degeneracy temperature of the quantum fluid and  $a$  the interatomic spacing. In  $^4\text{He-II}$  the coherence length is of order  $\xi \sim a$  and the temperature  $T \sim T_F$ , which means that  $E_v/(k_B T) \sim 1$  and thermally activated nucleation becomes possible. In contrast in  $^3\text{He-B}$  the coherence length is in any case more than 10 nm and we find  $E_v/(k_B T) \sim 10^5$  at temperatures of a few mK or less. The consequence from such an enormous barrier is that both thermal activation and quantum tunnelling are out of question as nucleation mechanisms. The only remaining intrinsic mechanism is a hydrodynamic instability, which develops at rather high velocity. This fact has made possible the measurement of neutron-induced vortex formation as a function of the applied flow velocity.

### 2.6.2. Rotating states of the superfluid

When a container with superfluid is set into rotation and the formation of vortex lines is inhibited by a high

energy barrier, then the superfluid component remains at rest in the laboratory frame and its velocity is zero in the whole container:  $v_s = 0$ . The normal excitations, in contrast, corotate with the container and  $v_n = \Omega r$ . This state of vortex-free counterflow is called the Landau state. It corresponds to the Meissner state in superconductors, with complete flux expulsion.

In  $^4\text{He-II}$  vortex-free flow is of little practical meaning in most situations, because even at very low velocities remanent vorticity leads to efficient vortex formation. In  $^3\text{He-B}$  the superfluid coherence length is several orders of magnitude larger and remanent vorticity can be avoided if the container walls are sufficiently smooth. Coupled with a high nucleation barrier, metastable rotating states then become possible. These can include an arbitrary number  $N$  of rectilinear vortex lines, where  $N \leq N_{\text{max}}$ . In most experimental situations the maximum possible vortex number,  $N_{\text{max}}$ , equals that in the equilibrium vortex state,  $N_{\text{eq}} \approx 2\pi\Omega R^2/\kappa$ . The equilibrium vortex state is obtained by cooling the container slowly at constant  $\Omega$  through  $T_c$ .

If the number of lines is smaller than that in the equilibrium state, then the existing vortex lines are confined within a central vortex cluster, as shown in Fig. 4. The confinement comes about through the Magnus force from the superfluid vortex-free counterflow,  $v = v_n - v_s$ , which circulates around the central cluster. Within the cluster mutual repulsion keeps the lines apart such that they form a triangular array at the equilibrium density,  $n_v = 2\Omega/\kappa$ , which is constant over the transverse cross section of the cluster. At this line density the cluster corotates with the container at constant  $\Omega$ , like a solid body. The total number of lines is given by  $N = \pi n_v R_v^2$ , where  $R_v$  is the radius of the cluster.

With  $N$  vortex lines in the cluster, the superflow velocity outside has the value  $v_s = \kappa N/(2\pi r)$ , which is equivalent to that around a giant vortex with  $N$  circulation quanta  $\kappa$  (Fig. 4). The counterflow velocity  $v$  vanishes inside the cluster (measured on length scales which exceed the inter-vortex distance), while outside it increases from zero at  $r = R_v$  to its maximum value at the cylinder wall,  $r = R$ :

$$v(R) = \Omega R - \frac{\kappa N}{2\pi R}. \quad (7)$$

In the absence of the neutron source, new vortex lines are only formed if  $v(R)$  is increased to its container-dependent critical value  $v_c(T, P)$  (Parts et al. 1995; Ruutu et al. 1997a). For a quartz glass cylinder  $v_c$  is a factor of three or more larger than the lowest velocity  $v_{cn}(T, P)$  at which vortices start to appear in neutron irradiation (Fig. 12).

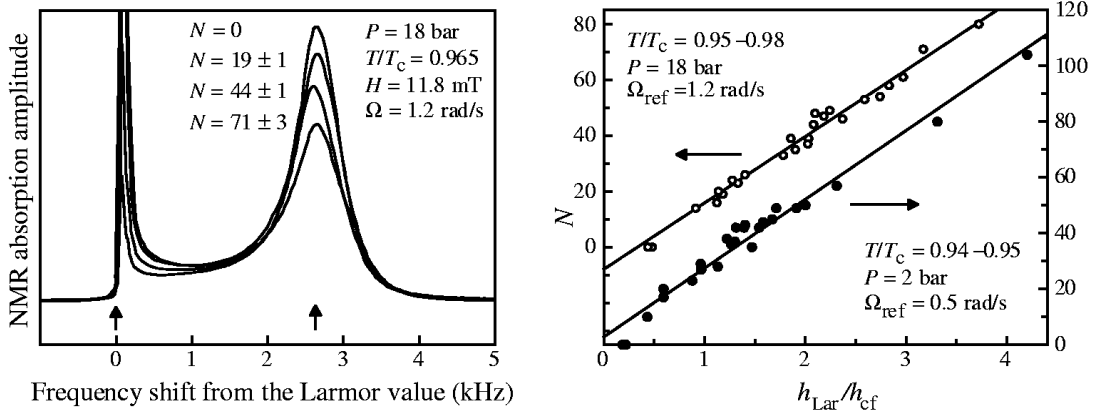


FIG. 5. NMR measurement of vortex lines in superfluid  $^3\text{He-B}$ , when rotated in a long cylinder with the magnetic field oriented axially: (Left) NMR spectra recorded at a reference velocity  $\Omega_{\text{ref}} = 1.2$  rad/s with different number of vortex lines  $N$ . The Larmor frequency is at the left and the counterflow peak at the right vertical arrow. (Right) Two calibration measurements of the number of vortex lines  $N$  as a function of the ratio of the Larmor and counterflow peak heights,  $h_{\text{Lar}}/h_{\text{cf}}$ , measured at two different rotation velocities  $\Omega_{\text{ref}}$ . (From Xu et al. 1996).

### 2.6.3. NMR measurement

Pairing in states with spin  $S = 1$  and orbital momentum  $L = 1$  leads to the unusual NMR properties of the  $^3\text{He}$  superfluids. The NMR absorption spectrum, recorded at low rf excitation in a traditional transverse cw measurement, is related to the spatial distribution of the order parameter in the rotating cylinder. Here spin-orbit coupling, although weak, is responsible for the large frequency shifts which give rise to absorption peaks shifted from the Larmor frequency (Vollhardt and Wölfle 1990). The height of the so-called counterflow peak in  $^3\text{He-B}$ , which depends on the counterflow velocity around the vortex cluster, can be used to determine the number of rectilinear vortex lines in the cluster.

In the left panel of Fig. 5 cw NMR absorption spectra are shown for  $^3\text{He-B}$ , measured at the same  $\Omega$ , but with a different number  $N$  of vortex lines in the container. The asymmetric peak on the left close to the Larmor frequency originates primarily from the center of the container where the average counterflow velocity is close to zero. This region shrinks rapidly with increasing  $\Omega$  in the vortex-free state. If vortex lines are added, the region expands with the size of the cluster. Outside the cluster the macroscopic normal-superfluid counterflow shifts the NMR absorption to higher frequencies into the counterflow peak, which is shown on the right. Its frequency shift increases monotonically with decreasing temperature and is used as a measure of the temperature. When the number of vortex lines in the container changes, the relative amount of absorption in the Larmor and counterflow peaks changes. This is because the total integrated absorption in the NMR spectrum is proportional to the B phase susceptibility  $\chi_B(T, P)$ , which is constant if only  $N$  undergoes a change. Thus by monitoring the peak height

of either of these absorption maxima, one can detect a change in  $N$ , as was shown in Fig. 3.

In the right panel of Fig. 5 the ratio of the two peak heights has been calibrated to give the vortex number at two different angular velocities  $\Omega_{\text{ref}}$ . In both cases only a relatively small number of vortex lines is present ( $N \ll N_{\text{max}}$  and the counterflow peak is large (Xu et al. 1996). This calibration plot was measured by starting with an initially vortex-free sample rotating at  $\Omega_{\text{ref}}$ , into which a given number of vortex lines  $N$  were introduced with neutron absorption reactions, as in Fig. 3. After that the whole NMR spectrum was recorded (by sweeping the magnetic polarization field  $H$ ). By measuring the ratio of the heights of the two absorption peaks from the spectrum and by plotting it versus  $N$ , the linear relationships in Fig. 5 were obtained.

The reduction in the height of the counterflow peak from the addition of one single vortex line can be discerned with good resolution in favorable conditions (Fig. 3). The optimization of this measurement has recently been analyzed by Kopu et al. (2000). With a small-size superconducting magnet and its modest field homogeneity ( $\Delta H/H \sim 10^{-4}$ ), the best conditions are usually achieved at low magnetic field ( $H \sim 10 - 20$  mT) close to  $T_c$  ( $T \geq 0.8 T_c$ ) and at relatively high counterflow velocity ( $\Omega > 0.6$  rad/s), where the counterflow peak is well developed (Korhonen et al. 1990). The single-vortex signal, i.e. the change in peak height per vortex line, decreases with increasing rotation and height of the counterflow peak, as shown in Fig. 6. In neutron irradiation measurements, the rate of vortex line creation  $\dot{N}$  is determined directly from records like the two traces in Fig. 3. The plot in Fig. 6 provides a yard stick for the single-vortex signal, to estimate the number of new lines when multiple lines are created in one neutron absorption

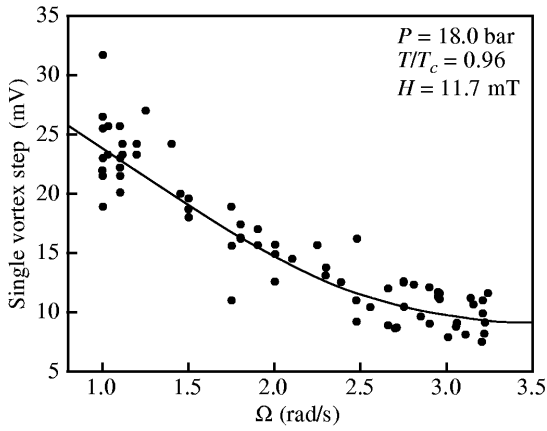


FIG. 6. Absolute magnitude of the single-vortex signal (as in Fig. 3), measured in the vortex-free counterflow state at different  $\Omega$ . The reduction in the height of the counterflow peak is given here in millivolts at the output of the cooled preamplifier which has a gain of  $\approx 10$  and is located inside the vacuum jacket of the cryostat. The scatter in the data arises from residual differences in the measuring temperature, perhaps from small differences in the order-parameter texture from one cool down to the next, and from an electronic interference signal which is generated by the rotation of the cryostat. More details on the NMR spectrometer are given by Parts et al. (1995) and Ruutu et al. (1997a).

event.

### 2.7. Vortex formation in neutron irradiation

A measurement of vortex-line formation in neutron irradiated normal-superfluid counterflow is performed at constant ambient conditions. The externally controlled variables include the rotation velocity  $\Omega$ , temperature  $T$ , pressure  $P$ , magnetic field  $H$ , and neutron flux  $\phi_n$ . The initial state is one of vortex-free counterflow:  $N = 0$ . When stable conditions have been reached, a weak neutron source is placed at a distance  $d$  from the  $^3\text{He-B}$  sample and the output from the NMR spectrometer is monitored as shown in Fig. 3. From this NMR absorption record as a function of time, the vortex lines can be counted which are formed during a given irradiation period.

The process evidently exhibits statistical behaviour. To measure the vortex-formation rate  $dN/dt = \dot{N}$ , records with a sufficiently large number of detected neutron absorption events are analyzed to obtain a representative result. After that one of the experimental parameters is changed and a new run is performed. In this way the dependence of the vortex formation process on the external variables can be studied. It was found that  $\dot{N}$  varies as a function of all the external parameters, i.e. neutron flux, rotation velocity, temperature, pres-

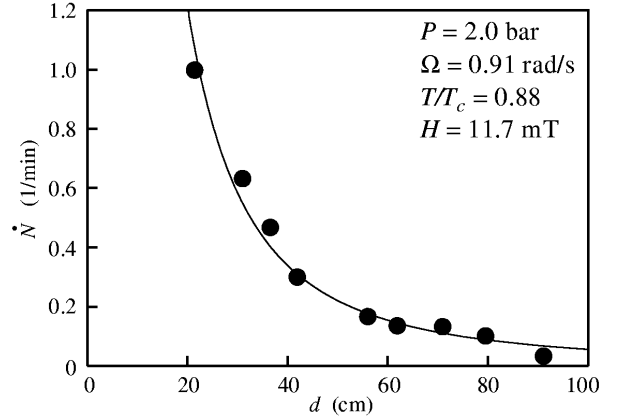


FIG. 7. Rate of vortex-line formation in neutron irradiated counterflow,  $\dot{N}$ , as a function of the distance  $d$  between neutron source and  $^3\text{He-B}$  sample. The initial state for all data points is vortex-free counterflow at a rotation velocity of 0.91 rad/s. The neutron irradiation time is 30 min. The fitted curve is of the form  $\ln[1 + (R_s/d)^2]$ , where  $R_s$  is the radius of the circular front surface of the paraffin moderator box (perpendicular to  $d$ ), in which the Am-Be source is embedded.

sure and magnetic field. In the following we shall first describe these empirically established dependences.

The rate of vortex-line formation is proportional to the neutron flux. The latter is varied by changing the distance of the source from the cryostat. In this way individual absorption events can be studied, which are well separated in time. A calibration plot of the measured rate  $\dot{N}$ , as a function of the distance between sample and source, is shown in Fig. 7. By means of this plot the results can be scaled to correspond to the same incident neutron flux, for example with the source at the minimum distance  $d = 22$  cm, which is given by the outer radius of the liquid He dewar.

A most informative feature is the dependence of  $\dot{N}$  on rotation (Ruutu et al. 1996a,b, 1998a). Rotation produces the applied counterflow velocity at the neutron absorption site. Since the absorption happens close to the wall of the container, the velocity of this bias flow is approximately equal to  $v(R)$  (Eq. (7)), the counterflow velocity at the cylinder wall. We shall denote this velocity simply by  $v$ . It depends both on the angular velocity  $\Omega$  and the number of vortex lines  $N(t)$  which are already present in the container. The counterflow provides the force which allows vortex rings to escape from the heated neutron bubble and to expand to rectilinear vortex lines, which are then preserved in the central vortex cluster. However, the first question is whether it is the velocity  $v$  of the counterflow or, for instance, that of the normal component,  $v_n(R) = \Omega R$ , which is the important variable controlling the rate  $\dot{N}(\Omega)$  in Fig. 3.

This question is answered in Fig. 8 where the number

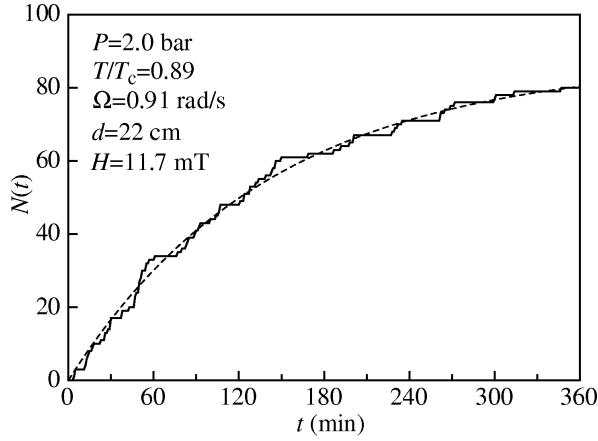


FIG. 8. Cumulative number of vortex lines  $N(t)$  as a function of time  $t$ , after turning on the neutron irradiation at constant flux on an initially vortex-free  $^3\text{He-B}$  sample rotating at constant  $\Omega$ . The dashed curve represents a fit to Eq. (10) with  $\alpha = 1.1 \text{ min}^{-1}$  and  $v_{\text{cn}} = 1.9 \text{ mm/s}$ . The result demonstrates that the rate of vortex-line formation is controlled by the counterflow velocity  $v$  and not by that of the normal component  $v_n(R) = \Omega R$ , which is constant during this entire measurement. (From Ruutu et al. 1996b).

of vortex lines  $N(t)$  is shown during neutron irradiation at constant external conditions over a time span of six hours. The irradiation is started from the vortex-free state:  $N(t=0) = 0$ . The rate  $\dot{N}(t)$ , at which vortex lines accumulate in the centre of the container, is not constant: Initially both the counterflow velocity and the rate of vortex formation are the highest. When more vortex lines collect in the central cluster, both the velocity  $v$  and the rate  $\dot{N}$  fall off. Finally the vortex number  $N$  approaches a saturation value, beyond which no more lines are formed. This means that there exists a lower limit, a threshold value for the counterflow velocity  $v$ , below which the neutron absorption events produce no vortex lines at all.

In principle the dependence of  $\dot{N}$  on the counterflow velocity  $v$  can be extracted from experiments like that in Fig. 8. However, more efficient is a measurement of only the initial linear part of the  $\dot{N}(t)$  record. Typically 15–30 min accumulation periods are used. Only a small number of vortices form during such a run compared to the number of vortices in the equilibrium state. Thus the decrease in the counterflow velocity as a function of time is minor and can be accounted for by assigning the average of the velocities before and after irradiation as the appropriate value of the applied counterflow velocity. An example of unprocessed data is shown in Fig. 9.

These measurements reveal a vortex-formation rate  $\dot{N}$  as a function of  $v$  which has an onset at a threshold velocity  $v_{\text{cn}}$ , followed by a rapid non-linear increase. As shown in Fig. 3, close above the threshold a successful

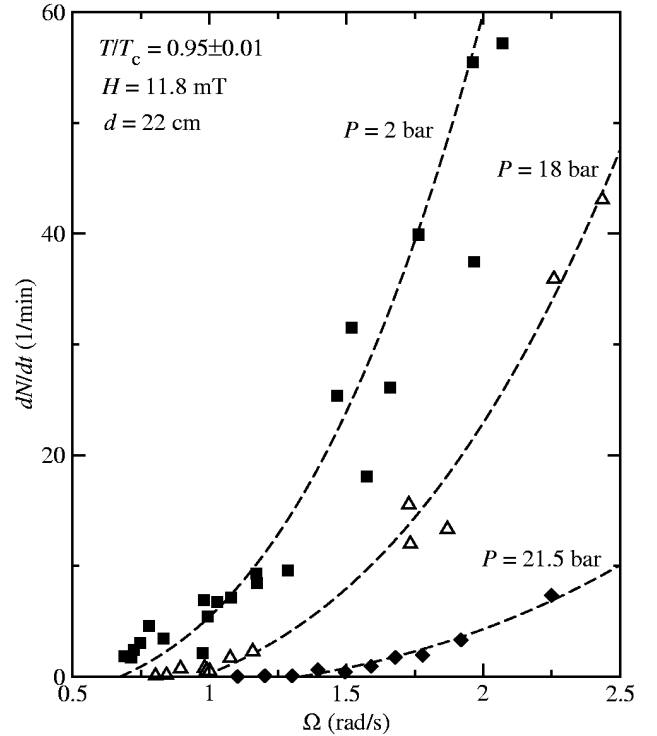


FIG. 9. Initial rate  $\dot{N}$  of vortex line formation at different rotation velocities  $\Omega$ .  $\dot{N}$  has been measured as the average of all vortex lines formed during an accumulation period of 15–30 min. The fitted curves are of the form  $\text{const} \cdot ((\Omega/\Omega_{\text{cn}})^3 - 1)$ . Their low velocity end points determine the threshold velocity  $v_{\text{cn}} = \Omega_{\text{cn}} R$ .

neutron absorption event produces one vortex line, but at high flow rates many lines may result. Therefore the nonlinear dependence  $\dot{N}(\Omega)$  arises in the following manner: Initially the fraction of successful absorption events increases, i.e. of those which produce one new vortex line. Eventually this effect is limited by the neutron flux, when essentially all absorbed neutrons produce at least one new vortex. The second part of the increase is brought about by the fact that more and more lines are produced, on an average, in each absorption event.

In Fig. 10 the rate  $\dot{N}$  is shown as a function of the counterflow velocity  $v$ . The dependence is approximated by the empirical expression

$$\dot{N}(v) = \alpha \left[ \left( \frac{v}{v_{\text{cn}}} \right)^3 - 1 \right]. \quad (8)$$

This equation also describes the results in Fig. 8: If initially  $v$  in the vortex-free state is only slightly larger than the critical velocity  $v_{\text{cn}}$ , then Eq. (8) can be linearized to  $\dot{N} \simeq 3\alpha(v/v_{\text{cn}} - 1)$ . Thus  $N(t)$  is given by

$$\dot{N}(t) = 3\alpha \left( \frac{v(0) - \kappa N(t)/(2\pi R)}{v_{\text{cn}}} - 1 \right) \quad (9)$$

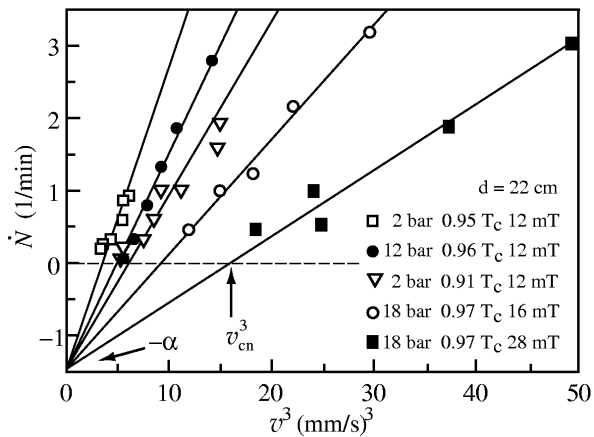


FIG. 10. Vortex-formation rate  $\dot{N}$  plotted versus the cube of the applied counterflow velocity  $v$ . This plot is used to determine the threshold velocity  $v_{cn}$ . A line has been fit to each set of data, measured under different external conditions, to identify the horizontal intercept  $v_{cn}^3$  and the common vertical intercept  $-\alpha = -1.4 \text{ min}^{-1}$ . (From Ruutu et al. 1996a).

with the solution

$$N(t) = \frac{2\pi R}{\kappa} [v(0) - v_{cn}] \left[ 1 - \exp\left(-\frac{3\alpha\kappa t}{2\pi R v_{cn}}\right) \right]. \quad (10)$$

This equation has been fit to the measurements to give the two parameters  $\alpha$  and  $v_{cn}$  in Fig. 8. The resulting values agree with those of the horizontal and vertical zero intercepts in Fig. 10.

At high rotation velocities a large number of vortex lines is produced in each neutron absorption event. The accumulation record for one neutron irradiation session (similar to the upper trace in Fig. 3) then consists of many large steps where, in the worst case, two absorption events might even be overlapping. Nevertheless, the final total number of lines, which have been collected into the central cluster, can be determined in a few different ways and these give consistent answers. These tests have been described in Fig. 11. One of them includes the use of the rate equation (8) where the multiplier  $\alpha$  has the value from Fig. 10.

In fact, it can be guessed from Fig. 10 that Eq. (8) has wider applicability than is apparent from the present examples: The same equation holds universally under different externally applied conditions with all dependence on external variables contained in  $v_{cn}(T, P, H)$ , while  $\alpha$  is proportional to the neutron flux but does not depend on temperature, pressure or magnetic field. Hence  $\dot{N}(v/v_{cn})$  appears to be a universal function for all measurements which have been performed (restricted so far to the temperature regime  $T > 0.8 T_c$ ).

To summarize, the experimental result displays two distinguishing properties: 1) the cubic dependence on the bias  $v$  and 2) the universality feature that all dependence

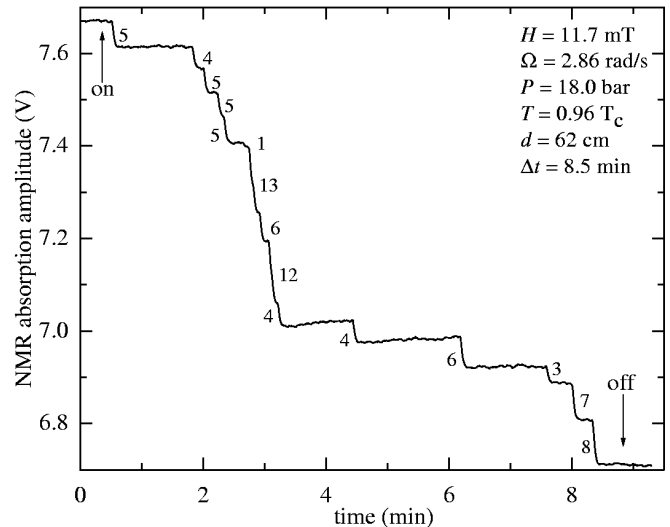


FIG. 11. Neutron irradiation and measurement of vortex-line yield at high rotation velocity. The total number of lines, which are created in one irradiation session, can be determined in several ways: 1) In this example the direct count of the steps in signal amplitude yields 88 lines (cf. Fig. 3). The number next to each step denotes its equivalent in number of extracted vortex lines. 2) From Fig. 6 one finds that the drop in signal amplitude per vortex line is 11 mV in the present measuring conditions. The total amplitude drop of 960 mV corresponds thus to 87 vortex lines. 3) A measurement of the annihilation threshold, by successive deceleration to lower and lower  $\Omega$  (Ruutu et al. 1997a), gives the total number of lines in the vortex cluster. Here this measurement yields  $\Omega_v = 0.245 \text{ rad/s}$ . The annihilation threshold, which at  $\Omega_v \gtrsim 0.2 \text{ rad/s}$  coincides with the equilibrium vortex state, corresponds to  $N = \pi R^2 2\Omega_v \kappa^{-1} (1 - 0.18\sqrt{1 \text{ rad s}^{-1}/\Omega_v})$ , as measured by Ruutu et al. (1998b). With  $R = 2.45 \text{ mm}$ , this gives 88 vortex lines. 4) The rate equation (8) with the measured value of  $\alpha$  in Fig. 10 gives 88 lines for an irradiation time of 8.5 min with the measured threshold value  $\Omega_{cn} = 0.75 \text{ rad/s}$ . Thus all of the reduction in the height of the counterflow absorption peak (cf. Fig. 5) can be reliably accounted for in four different ways.

of the vortex formation properties on the experimental variables  $T$ ,  $P$ , and  $H$  is contained in the threshold velocity  $v_{cn}$ .

## 2.8. Threshold velocity for vortex loop escape

The dependence on the counterflow bias  $v$  can be studied from the threshold  $v_{cn}$  up to the critical limit  $v_c$  at which a vortex is spontaneously nucleated at the cylindrical wall in the absence of the neutron flux (Parts et al. 1995; Ruutu et al. 1997a). The threshold velocity  $v_{cn}(T, P, H)$  is one of the features of the experiment which can be analyzed to learn more about the mechanism of vortex formation. Measurements of both critical

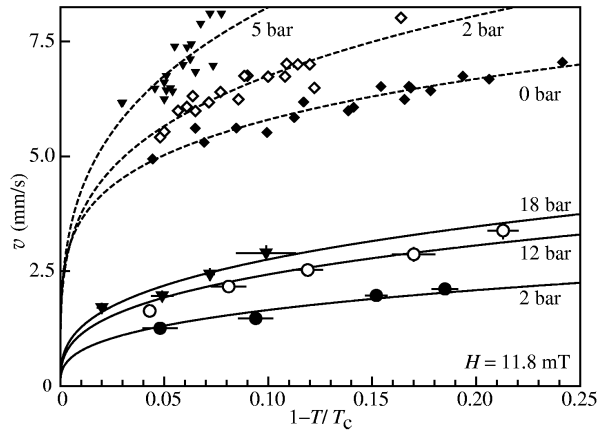


FIG. 12. Critical values of the applied counterflow velocity  $v$  vs. the normalized bulk liquid temperature at different pressures: (Solid lines) Threshold velocity  $v_{\text{cn}} \propto (1 - T/T_c)^{1/3}$ , where vortex formation starts in the presence of the neutron source (Ruutu et al. 1996a). (Dashed lines) Critical velocity  $v_c \propto (1 - T/T_c)^{1/4}$ , where a vortex is spontaneously nucleated in the same quartz glass container in the absence of the neutron source. (From Parts et al. 1995; Ruutu et al. 1997a).

velocities  $v_{\text{cn}}$  and  $v_c$  are shown in Fig. 12 as a function of temperature.

### 2.8.1. Properties of threshold velocity

By definition the threshold  $v_{\text{cn}}$  represents the smallest velocity at which a vortex ring can escape from the neutron bubble after the absorption event. It can be connected with the bubble size in the following manner. A vortex ring of radius  $r_o$  is in equilibrium in the applied counterflow at  $v$  if it satisfies the equation

$$r_o(v) = \frac{\kappa}{4\pi v} \ln \left( \frac{r_o}{\xi(T, P)} \right). \quad (11)$$

This follows from the balance between self-induced contraction and expansion by the Magnus force, as explained in more detail in Sec. 2.11.2. A ring with a radius larger than  $r_o$  will expand in the flow while a smaller one will contract. Thus the threshold or minimum velocity at which a vortex ring can start to expand towards a rectilinear vortex line corresponds to the maximum possible vortex-ring size. This must be of a size comparable to the diameter of the heated bubble. For a simple estimate we set the vortex ring radius equal to that of a spherical neutron bubble:  $r_o(v_{\text{cn}}) \sim R_b$ . (In fact, the numerical simulations to be described in Sec. 2.13.3 suggest that  $r_o(v_{\text{cn}}) \approx 2R_b$  because of the complex convoluted shape of the largest rings in the random vortex network.)

A simple thermal diffusion model can now be used to yield an order of magnitude estimate for the radius  $R_b$  of the bubble which originally was heated above  $T_c$ . In the

temperature range close to  $T_c$  the cooling occurs via diffusion of quasiparticle excitations out into the surrounding superfluid with a diffusion constant  $D \approx v_F l$ , where  $v_F$  is their Fermi velocity and  $l$  their mean free path. The difference from the surrounding bulk temperature  $T_0$  as a function of the radial distance  $r$  from the centre of the bubble can be calculated from the diffusion equation

$$\frac{\partial T(r, t)}{\partial t} = D \frac{\partial^2 T}{\partial r^2} + \frac{2}{r} \frac{\partial T}{\partial r}. \quad (12)$$

With the assumption that at  $t = 0$  the reaction energy  $E_0$  is deposited at  $r = 0$ , the solution is given by

$$T(r, t) - T_0 \approx \frac{E_0}{C_v} \frac{1}{(4\pi Dt)^{3/2}} \exp\left(\frac{-r^2}{4Dt}\right), \quad (13)$$

where  $C_v$  is the specific heat. For now, we may assume that all the energy of the neutron absorption reaction is deposited as heat. The bubble of normal fluid,  $T(r) > T_c$ , first expands and reaches a maximum radius

$$R_b = \sqrt{\frac{3}{2\pi e}} \left( \frac{E_0}{C_v T_c} \right)^{1/3} (1 - T_0/T_c)^{-1/3}. \quad (14)$$

It then starts cooling and rapidly shrinks with the characteristic time  $\tau_Q \sim R_b^2/D \sim 1\mu\text{s}$ . Since  $v_{\text{cn}}$  is inversely proportional to  $r_o \sim R_b$ , it has the temperature dependence  $v_{\text{cn}} \propto (1 - T_0/T_c)^{1/3}$ . This is in agreement with the solid curves in Fig. 12 which have been fitted to measurements on  $v_{\text{cn}}$ . The prefactor of these curves is in agreement with that from Eqs. (14) and (11) within a factor of  $\sim 2$ , and its increase with increasing pressure is well described by the decrease in bubble size according to Eq. (14), where  $C_v$  and  $T_c$  increase with pressure (Greywall 1986).

### 2.8.2. Superflow instability vs KZ mechanism

Above we have assumed that the largest radius of vortex loops, which manage to escape into the bulk at the threshold velocity  $v_{\text{cn}}$ , is approximately  $R_b$ , the radius of the heated bubble. This analysis is consistent with the KZ mechanism, but by no means proof of it: Other processes of hydrodynamic origin can be suggested with a similar interpretation for the threshold velocity. The neutron-induced experiment in  $^3\text{He-B}$  is not an exact replica of the ideal KZ model — namely that of a second order transition in an infinite homogeneous system. Inside the heated bubble there is a strong thermal gradient and a strict boundary condition applies at its exterior, imposed by the bulk superfluid state outside. Moreover, the cool down occurs so fast that any extrapolation from the equilibrium state theories is uncertain, whether it concerns the hydrodynamics or even the superfluid state

itself. The applicability of the KZ mechanism to inhomogeneous transitions is considered in more detail in Sec. 2.14.

In addition to the KZ mechanism, one can suggest other alternative sources of vortex formation. One of the most evident is the superflow instability in the outer peripheral regions of the neutron bubble where the fluid remains in the B phase but is heated above the surrounding bulk temperature  $T_0$ . In the Ginzburg-Landau temperature regime the container-dependent spontaneous critical velocity  $v_c(T, P)$  decreases with increasing temperature (dashed curves in Fig. 12). It is related to the intrinsic instability velocity  $v_{cb}(T, P)$  of the bulk superfluid (Parts et al. 1995; Ruutu et al. 1997a), which has qualitatively a similar temperature and pressure dependence, but is larger in magnitude. Consequently, if no other process intervenes, the superflow instability has to occur within a peripheral shell surrounding the neutron bubble: Within this layer the local temperature corresponds to that at which the applied counterflow velocity  $v$  equals the critical value  $v_{cb}(T, P)$  for bulk superflow.

One or several vortex rings are then formed, which encircle the bubble. Their number depends on the shape and size of the bubble and on the counterflow velocity. In this process it does not matter what the state of the liquid is in the interior of the bubble: The rings are formed within an external cooler layer, which remains throughout the process in the B phase. After their formation the rings will start to expand and will eventually be pulled away by the Magnus force. Thus these might be the vortex rings which give rise to the vortex lines observed in the NMR measurements. As long as the external vortex rings are still in the vicinity of the bubble they shield its central volume from the applied superflow and any vorticity within the bubble will start to collapse in the presence of dissipation. In this scenario it is thus the superfluid boundary condition which by necessity enforces the formation of vortex rings, if no vortices have been formed at an earlier stage in the interior of the bubble.

Recently numerical simulation work has been carried out on the rapid cooling of a model system with a scalar order parameter, using the thermal diffusion equation to account for the cooling and the time-dependent Ginzburg-Landau equation for the order-parameter relaxation (Aranson et al. 1999). In the presence of the applied superflow the instability at the moving normal-superfluid boundary was indeed found to compete with the KZ mechanism – both processes produced vorticity. According to this simulation the vortex rings, which eventually managed to escape into the bulk superfluid, originated mainly from the bubble boundary while the random vortex network in the interior of the bubble decayed away. Thus the experimentalist now faces the question whether any experimental arguments can be found to discern between the superfluid boundary condition or

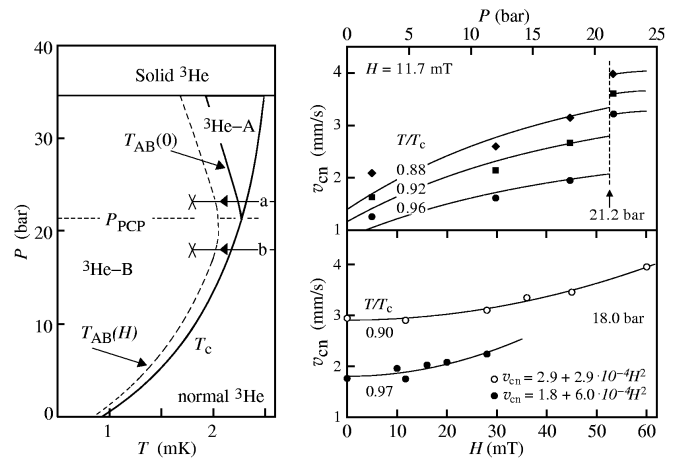


FIG. 13. Threshold velocity  $v_{cn}$  for the onset of vortex formation during neutron irradiation: (Left) Phase diagram of  $^3\text{He}$  superfluids in the pressure vs. temperature plane, with the A $\rightarrow$ B transition at  $T_{AB}(0)$  in zero field (solid line) and at  $T_{AB}(H)$  in nonzero field (dashed line). Two quench trajectories, distinguishing different types of measurements on the right, are marked with (a) and (b). (Right top) The pressure dependence of  $v_{cn}$  displays a steep change at the pressure  $P_{PCP}$  of the polycritical point. (Right bottom) The magnetic field dependence of  $v_{cn}$  is parabolic, similar to that of the equilibrium state A $\rightarrow$ B transition  $T_{AB}(H)$ . (From Ruutu et al. 1998a).

the KZ mechanism as the source for the observed vortex lines.

### 2.8.3. Influence of $^3\text{He-A}$ on threshold velocity

The measurements on the threshold velocity  $v_{cn}$  offer an interesting possibility to check whether the interior of the heated bubble participates in the vortex formation or not. In the left panel of Fig. 13 the phase diagram of  $^3\text{He}$  is shown at temperatures below 2.5 mK. In the measurements which we discussed so far, the liquid pressure has been below 21.2 bar, so that the heated bubble cools from the normal phase along a trajectory marked with (b) directly into the B phase. On the top right in Fig. 13 the measured  $v_{cn}$  is plotted as a function of pressure  $P$  at constant reduced temperature  $T/T_c$ . Here the pressure dependence displays an abrupt increase at about 21.2 bar, the pressure  $P_{PCP}$  of the polycritical point: It thus makes a quantitative difference whether the quench trajectory follows a path denoted with (a) or with (b)! The two cooling trajectories differ in that above  $P_{PCP}$  a new phase,  $^3\text{He-A}$ , is a stable intermediate phase between the normal and B phases. Consequently, although the bulk liquid is well in the B phase in all of the measurements of Fig. 13, vortex formation is reduced when the quench trajectory crosses the stable A-phase regime.

The pressure dependence of  $v_{\text{cn}}$  at  $P_{\text{PCP}}$  differs from the typical behavior of the bulk B-phase properties, which are changing smoothly with pressure. For instance, the superflow instability at the warm boundary of the heated bubble, where the liquid is all the time in the B phase, occurs close to the  $^3\text{He}$ -B pair-breaking velocity, at  $v_{\text{cb}}(T, P) \approx v_{\text{c0}}(P) (1 - T/T_c)^{1/2}$ , where  $v_{\text{c0}}(P) = 1.61 (1 + F_1^s/3) k_B T_c / p_F$  (Parts et al. 1995; Ruutu et al. 1997a). This instability velocity is a smooth function of pressure and does not reproduce the measured dependence in Fig. 13.

The fitted curves in Fig. 13, which represent  $v_{\text{cn}}(P)$  at pressures below  $P_{\text{PCP}}$ , correspond to  $v_{\text{cn}} = (\varepsilon \kappa / 4\pi R_b) \ln(R_b/\xi)$ , where  $R_b = (3/2e\pi)^{1/2} (E_0/C_v T_c)^{1/3} (1 - T/T_c)^{-1/3}$ . If we assume that all of the reaction energy is transformed to heat ( $E_0 = 764$  keV), then the common scaling factor  $\varepsilon$  for all three curves, which is the only fitting parameter here, comes out as  $\varepsilon = 2.1$ . The same fit is also displayed as the solid curves in Fig. 12, which represent  $v_{\text{cn}}$  as a function of temperature. The good agreement suggests that the spherical thermal diffusion model is not too far off. The largest increase in  $v_{\text{cn}}$  at  $P_{\text{PCP}}$  is observed at the highest temperature, which in Fig. 13 is  $0.96 T_c$ . This property correlates with the notion that vortex formation is reduced and  $v_{\text{cn}}$  is increased when the relative range of A-phase stability increases during the quench.

In the lower right panel of Fig. 13 the dependence of  $v_{\text{cn}}$  on the applied magnetic field  $H$  is shown. Below  $P_{\text{PCP}}$  the magnetic field acts to stabilize  $^3\text{He}$ -A in a narrow interval from  $T_c$  down to the first order A $\rightarrow$ B transition at  $T_{\text{AB}}(P, H)$ . Thus the stability of the A phase can be boosted by either increasing the pressure above  $P_{\text{PCP}}$  or increasing the magnetic field. In both cases the A-phase energy minimum is reduced relative to that of the B phase and both operations result in a reduced yield of vortex lines at any given value of the bias  $v$ . The parabolic magnetic field dependence of  $v_{\text{cn}}(H)$  is reminiscent of that of the equilibrium  $T_{\text{AB}}(H)$  transition temperature.<sup>2</sup> It should be noted that the measurements in the upper right panel of Fig. 13 have not been carried out in zero magnetic field but in 11.7 mT. However, as shown in the lower panel, the field dependence in the range 0–12 mT is not visible within the experimental precision.

From the measurements in Fig. 13 it is to be concluded that the pressure and magnetic field dependences of  $v_{\text{cn}}$  do not support the superflow instability at the heated bubble boundary as the source for the neutron-induced vortex formation: This process is not affected by the de-

tails of the cooling process within the hot bubble. In all of the measurements of Fig. 13 the hot neutron bubble is surrounded by  $^3\text{He}$ -B where the instability velocity  $v_{\text{cb}}$  does not display the measured pressure and field dependences.

On the other hand, it is important to note that the qualitative features of the vortex formation process are not altered when the sequence of phases traversed within the cooling bubble are changed from (normal phase $\rightarrow$  $^3\text{He}$ -B) to (normal phase $\rightarrow$  $^3\text{He}$ -A $\rightarrow$  $^3\text{He}$ -B). As shown in Figs. 9 and 10, except for the increased magnitude of  $v_{\text{cn}}$ , the qualitative features of vortex formation and in particular the form of the rate equation (8) remain unchanged below and above  $P_{\text{PCP}}$ .

## 2.9. Other defect structures formed in neutron irradiation

### 2.9.1. Radiation-induced supercooled A $\rightarrow$ B transition

Another piece of experimental evidence, which suggests that the boundary of the neutron bubble is not the only controlling factor, comes from measurements of the radiation induced increase in the transition rate of supercooled  $^3\text{He}$ -A to  $^3\text{He}$ -B. These measurements address the old problem about the mechanism which starts the first order A $\rightarrow$ B transition from supercooled  $^3\text{He}$ -A. All usual arguments show that this transition should be forbidden because of an exceedingly high nucleation barrier (Leggett 1992; Schiffer et al. 1995). Nevertheless, it has been shown by Osheroff and his coworkers (Schiffer et al. 1992; Schiffer and Osheroff 1995) that a dramatic increase in the transition probability can be catalyzed by the localized heat input from radiation absorption.

Suppose we supercool  $^3\text{He}$ -A to relatively low temperatures below the thermodynamic A $\leftrightarrow$ B transition. In the absence of the neutron source the sample stays in the A phase for very long times, perhaps indefinitely, but when the neutron flux is turned on the transition probability increases sharply. The deeper the supercooling, the faster the transition into the B phase follows. In this experiment the initial state is supercooled  $^3\text{He}$ -A and the same state is also enforced by the boundary condition. Thus this explanation is not useful here while the KZ mechanism is one of the possible solutions (Volovik 1996; Bunkov and Timofeevskaya 1998a,b).

### 2.9.2. A $\rightarrow$ B transition via KZ mechanism

Nucleation of competing phases, with different symmetries and local minima of the energy functional, has also been discussed in the cosmological context (Linde 1990). It is believed that the  $SU(3) \times SU(2) \times U(1)$  symmetries

<sup>2</sup>According to Tang et al. (1991), below  $P_{\text{PCP}}$  the equilibrium A $\leftrightarrow$ B transition temperature is in first order of the form  $T_{\text{AB}}(P, H) = T_c(P) (1 - \alpha H^2)$ , where  $\alpha(P) \sim (0.5 - 10) \cdot 10^{-6} (\text{mT})^{-2}$ .

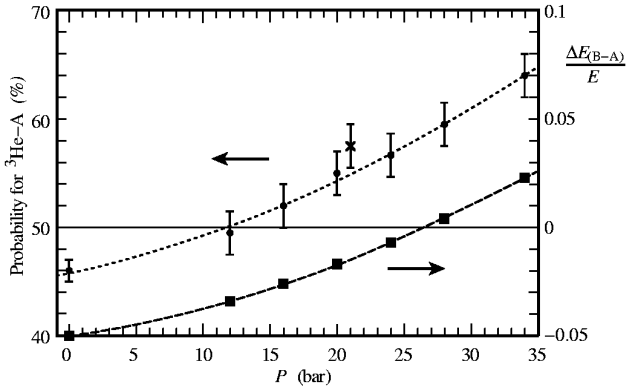


FIG. 14. Normalized energy difference,  $\Delta E/E(P)$ , between A and B phases (*right vertical axis*) and probability of A phase formation in a rapid cool-down (*left vertical axis*), plotted as a function of pressure at temperatures close to  $T_c$  in the Ginzburg-Landau regime. The results have been calculated with the weak coupling  $\beta$  parameters ( $\beta_i = -1, 2, 2, 2, -2$ ), except for the data point marked with a cross ( $\times$ ) on the upper curve, for which strong-coupling parameter values have been used according to the spin fluctuation model. (From Bunkov and Timofeevskaya 1998a,b).

of the strong, weak, and electromagnetic interactions (respectively) were united at high energies (or at high temperatures). The underlying Grand Unification (GUT) symmetry ( $SU(5)$ ,  $SO(10)$ , or a larger group) was broken at an early stage during the cooling of the Universe. Even the simplest GUT symmetry  $SU(5)$  can be broken in different ways: into the phase  $SU(3) \times SU(2) \times U(1)$ , which is our world, and into  $SU(4) \times U(1)$ , which apparently corresponds to a higher energy state. However, in supersymmetric models both phases represent local minima of almost equal depth, but are separated from each other by a high energy barrier.

In the cosmological scenario, after the symmetry break of the  $SU(5)$  GUT state, both new phases are created simultaneously with domain walls between them. The calculated probability for the creation of our world — the  $SU(3) \times SU(2) \times U(1)$  state — appears to be smaller than that of the false vacuum state of  $SU(4) \times U(1)$  symmetry at higher energy. Thus initially the state corresponding to our world appears to have occupied only a fraction of the total volume. Later bubbles of this energetically preferred state grew at the expense of the false vacuum state and finally completely expelled it. However, before that interfaces between the two states were created in those places where blobs of the two phases met. Such an interface is an additional topologically stable defect, which is formed in the transition process.

This situation resembles that of superfluid  $^3\text{He}$ , where the “GUT symmetry”  $SO(3) \times SO(3) \times U(1)$  can be broken to the  $U(1) \times U(1)$  symmetry of the A phase or to

the  $SO(3)$  symmetry of the B-phase, with a small energy difference between these two states, but separated by an extremely high energy barrier ( $\sim 10^6 k_B T$ ) from each other. For the  $A \rightarrow B$  transition in  $^3\text{He}$  the KZ mechanism was first discussed by Volovik (1996). This suggestion was put on quantitative ground by Bunkov and Timofeevskaya (1998a,b).

According to the KZ model in different parts of the cooling bubble the order parameter may fall initially either in the A or B phase energy minima. Thus a domain structure of size  $\xi_v$  (Eq. 3) is laid down, where A and B-phase blobs form a patch work. When these blobs later grow together, then AB interfaces start forming. The lower the temperature, the lower is the B-phase energy minimum relative to that of the A phase, the larger is the proportion of B-phase blobs in the patch work, and the more likely it is that many of them manage to merge together to form one large bubble, where the AB interface exceeds the critical diameter of about  $1 \mu\text{m}$ , needed for a spontaneous expansion of the bubble to start. This one seed then suffices to initiate the  $A \rightarrow B$  transition in the container.

The time dependent Ginzburg-Landau calculations of Bunkov and Timofeevskaya (1998a,b) are consistent with this model. The energy difference between the A and B phases is small and during rapid cool down through  $T_c$  the order parameter may settle into either of these two energy minima with a pressure-dependent probability shown in Fig. 14. The relative number of the A and B-phase blobs of size  $\xi_v$  is not only determined by the difference in the A and B-phase energies: It also depends on the trajectory from the normal phase to the new energy minimum in the phase space spanned by the order parameter components. The latter aspect gives more preference to the higher energy A state. In the calculations of Fig. 14 there is no spatial dependence, an initial fluctuation is imposed at  $T_c$  into a random direction of the phase space, and the evolution towards the final state is followed. The result shows that although the A-phase is energetically not favorable in a wide pressure range, the probability of its formation has a value close to 50 % even at low pressures.

The later evolution is similar to that in the cosmological scenario. In ambient conditions, where only B phase is stable, the A-phase blobs ultimately shrink away and only B phase remains. Before that, however, a network of AB interfaces is created which may interact with the formation of other topological defects. In any case, in supercooled  $^3\text{He-A}$  the KZ mechanism can lead with finite probability to the  $A \rightarrow B$  transition, independently of the boundary condition, which dictates  $^3\text{He-A}$ .

### 2.9.3. Threshold velocity, AB interfaces, and the KZ mechanism

At a pressure around  $P_{PCP}$  of the polycritical point, the KZ model predicts that in different parts of the cooling neutron bubble the order parameter may fall initially either in the A or B phase energy minima, and a patch work of AB interfaces is laid down. These interfaces are expected to interfere with the simultaneous formation of the random vortex networks within a bubble of each phase. It is known from experiments on a moving AB interface that the penetration of vortex lines through the AB phase boundary is suppressed (Krusius et al. 1994). We would expect that A-phase blobs reduce the combined B-phase volume inside the bubble. Consequently, when B-phase blobs have merged to larger units, the overall volume, into which the B-phase vortex network is confined, is smaller, and B-phase vortex formation becomes impeded. This process increases the value of  $v_{cn}$  and would be consistent with the measured pressure and magnetic field dependences in Fig. 13.

Thus we conclude that the KZ mechanism provides a unified explanation for the results in Fig. 13, which suggest that the interior of the heated bubble influences the value of  $v_{cn}$ , as well as for the radiation-induced A→B transition in supercooled  $^3\text{He-A}$ . In both cases the AB interfaces appear as a new type of defect when the neutron bubble cools through  $T_c$ . This interpretation suggests that the KZ mechanism is the fastest process by which defects are created, before other effects manage to switch on. Normally the creation of a sizeable bubble of B phase inside bulk A liquid requires that an AB interface of large size is formed. This is a slow and energy consuming process. In a rapid quench through  $T_c$  the AB interface appears only later as a metastable defect after the freeze-out of disconnected A and B-phase blobs, which are separated by normal liquid.

### 2.9.4. Spin-mass vortex

Unlike vortex lines, which are produced in neutron irradiation and partly are stabilized in the applied counterflow, no bias is usually provided for maintaining the AB interfaces. Thus in rotating experiments, the evidence for AB interfaces remains indirect. However, there is one more topologically stable defect, which can be directly observed after a neutron absorption event and which is maintained by the counterflow in the rotating container. This is a combined object called the spin-mass vortex (Kondo et al. 1992; Korhonen et al. 1993).

The signature from the spin-mass vortex is explained in Fig. 15, where the counterflow peak height is plotted as a function of time during neutron irradiation (as in Figs. 3 and 11). This accumulation record shows one oversized step in the absorption amplitude, which coincides with a

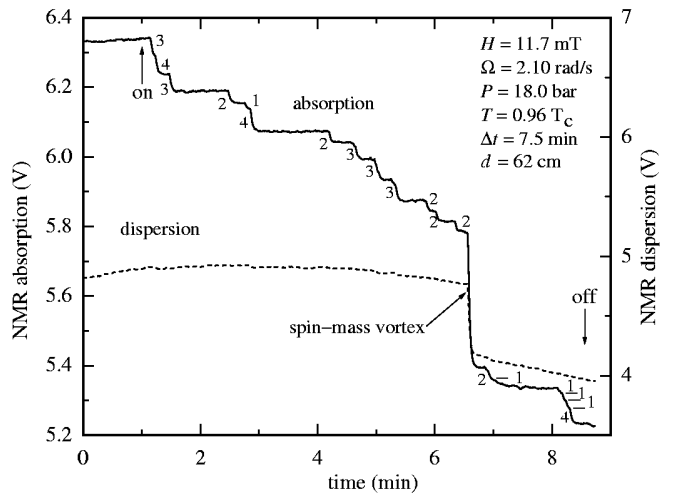


FIG. 15. Signal from spin-mass vortex in neutron irradiation. This irradiation session includes one large jump in the signal amplitude. As in Fig. 11, the various methods for extracting the total number of lines give: 1) A direct count of the steps in signal amplitude yields 45 lines plus the large jump. The combined amplitude drop for these 45 lines amounts to 716 mV which translates to 16 mV/vortex, in agreement with Fig. 6. With this step size the large jump of 390 mV would correspond to 25 additional lines. 2) A measurement of the annihilation threshold gives  $\Omega_v = 0.155$  rad/s, which corresponds to 48 lines. 3) The rate equation (8) gives  $\dot{N} = 6.2$  lines/min or a total of 48 lines for an irradiation of 7.5 min duration with the measured threshold value of  $\Omega_{cn} = 0.75$  rad/s. For these three estimates to be consistent, the large jump cannot be 25 lines. Instead it is interpreted to represent one spin-mass vortex line. In this case the size of the jump is not related to the number of lines, but to the counterflow velocity  $v(R)$  (Eq. (7)). It controls the length  $v(R)/2\Omega$  of the soliton sheet (Fig. 17). The dispersion signal also displays a simultaneous large jump, while it behaves smoothly when usual mass-current vortex lines are formed. Outside the discontinuity the dispersion signal is slowly drifting due to residual temperature creep.

similar discontinuous jump in the out-of-phase dispersion signal. As explained in the context of Fig. 11, the total number of vortex lines extracted from an irradiation session can be determined in several different ways. In the case of Fig. 15 a comparison of the different line counts shows that, within the uncertainty limits, the large jump cannot represent more than a few vortex lines. As will be seen below, this is the signature from a spin-mass vortex, which in Fig. 15 should be counted as one line.

The identification of the spin-mass vortex is based on its peculiar NMR spectrum (Fig. 16). In an axially oriented magnetic field the NMR spectrum has a textural cut off frequency, beyond which no absorption is allowed (excepting line broadening effects). The distinguishing feature of the spin-mass vortex is the absorption which has been pushed to the maximum possible frequency

shift, beyond that of the counterflow peak (which corresponds to 80% of the maximum value).

The appearance of the new maximum in the NMR spectrum close to, but not exactly at the monitored frequency explains why both the absorption and dispersion signals are discontinuous, when the spin-mass vortex is created (compare the two spectra in Fig. 16). Since both signals are continuously monitored at the lock-in-amplifier output, the jump in the dispersion signal provides the immediate alert for the spin-mass vortex. In contrast, no discontinuity in the dispersion signal is observed in first order when a small number of vortex lines is added to the cluster at high counterflow velocity. In this case some absorption intensity is shifted towards the Larmor edge to small frequency shifts, and the change in the dispersion signal at the site of the counterflow maximum is negligible.

The large-scale configuration, in which the spin-mass vortex appears, is shown in the top part of Fig. 17. It consists of a linear object and a planar domain-wall-like soliton sheet. The line defect provides one termination for the sheet while its second end is anchored on the cylindrical wall of the container. The line defect consists of a singular core, which supports a circulating superfluid mass current, but has additionally trapped a disclination line in spin-orbit coupling. The latter feature can also be described in terms of a spin vortex which supports a persistent spin current. Thus the composite object, the spin-mass vortex, has the combined properties of a usual mass-current vortex and a spin-current vortex. A gain in the core energy of the combined structure provides the energy barrier against their dissociation. The soliton sheet is the continuation from the breaking of the spin-orbit coupling into the bulk superfluid: It separates two degenerate domains with anti-parallel orientations of the B-phase anisotropy axis  $\hat{n}$  (lower part of Fig. 17). The spin-mass vortex feels the Magnus force from the counterflow, but this is partly compensated by the surface tension of the soliton sheet. The equilibrium position of the spin-mass vortex is therefore at the edge of the vortex cluster (top part of Fig. 17) from where it can be selectively removed by annihilation, as was done in the experiment of Fig. 16.

The origin of the two defects in the spin-mass vortex can be seen from the form which the B-phase order parameter has (Vollhardt and Wölfle 1990):

$$A_{\alpha j} = \Delta_B(T; P) e^{i\phi} R_{\alpha j}(\hat{n}, \theta). \quad (15)$$

It includes the isotropic energy gap  $\Delta_B(T, P)$ , the phase factor  $e^{i\phi}$ , and the rotation matrix  $R_{\alpha j}(\hat{n}, \theta)$ . The latter defines the rotation by which the  $SO(3)_L$  orbital and  $SO(3)_S$  spin spaces are rotated with respect to each other around the axis  $\hat{n}$  by the angle  $\theta$ . The mass-current vortex is associated with a  $2\pi$  circulation in the phase factor while the spin current results from the disclina-

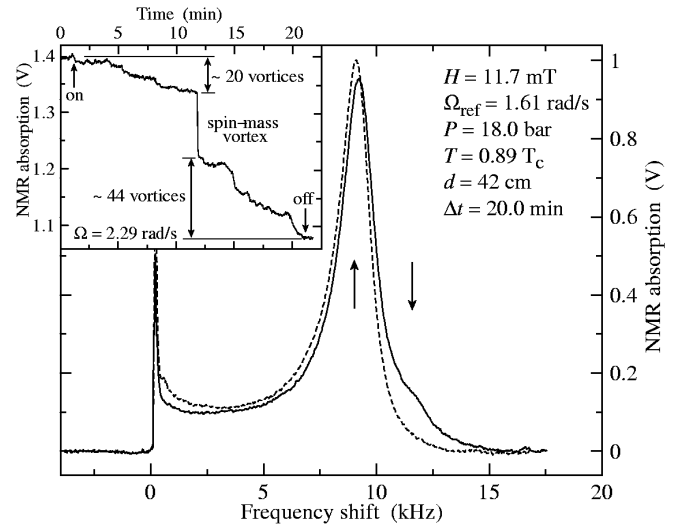


FIG. 16. NMR signal characteristics of the spin-mass vortex. (*Insert*) This 20 min irradiation session includes one large jump, in addition to vortex-line formation. The latter amounts to 64 lines, as determined from the measured annihilation threshold  $\Omega_v = 0.19$  rad/s. The rate equation (8) gives  $\dot{N} = 3.35$  lines/min or a total of 67 lines (with the measured  $\Omega_{cn} = 1.10$  rad/s). The combined drop in signal amplitude from these lines is 206 mV, which corresponds to 3.2 mV/line. Here at a lower temperature the step size per vortex is much reduced from that in Fig. 10. The large jump would correspond to 36 additional lines but to be consistent with other measurements it is interpreted to represent a spin-mass vortex, similar to Fig. 15. (*Main panel*) NMR spectra of the vortex cluster, recorded at a lower reference velocity  $\Omega_{ref}$ : The lower peak was traced first after the irradiation and deceleration from 2.29 to 1.61 rad/s. The higher peak was traced later after cycling  $\Omega$  from 1.61 to 0.20 rad/s and back, i.e. after decelerating to close above the annihilation threshold. In the former spectrum (solid line) the soliton sheet shifts a sizeable fraction of the absorption to the maximum possible frequency shift. This frequency shift is denoted with the right vertical arrow. After cycling  $\Omega$  the soliton and the spin-mass vortex have been removed, and the height of the counterflow peak increases back to where it would have been without the soliton (dashed line). Its frequency shift is denoted with the left vertical arrow. Since the cluster was not decelerated below the annihilation threshold of 0.19 rad/s, no usual vortex lines were yet removed from the second spectrum.

tion in  $R_{\alpha j}(\hat{n}, \theta)$  field (lower part of Fig. 17). The minimum of the weak spin-orbit interaction is reached when  $\theta = \arccos(-\frac{1}{4}) \approx 104^\circ$  homogeneously everywhere within the bulk superfluid. Therefore the volume where  $\theta$  traverses through  $\pi$  and the spin-orbit coupling is not minimized becomes confined within the soliton sheet.

In  $^3\text{He-B}$  weak anisotropy energies arise in an external magnetic field. They produce an extended orientational distribution, or texture, of the anisotropy axis  $\hat{n}$ . The characteristic length scale of this texture in

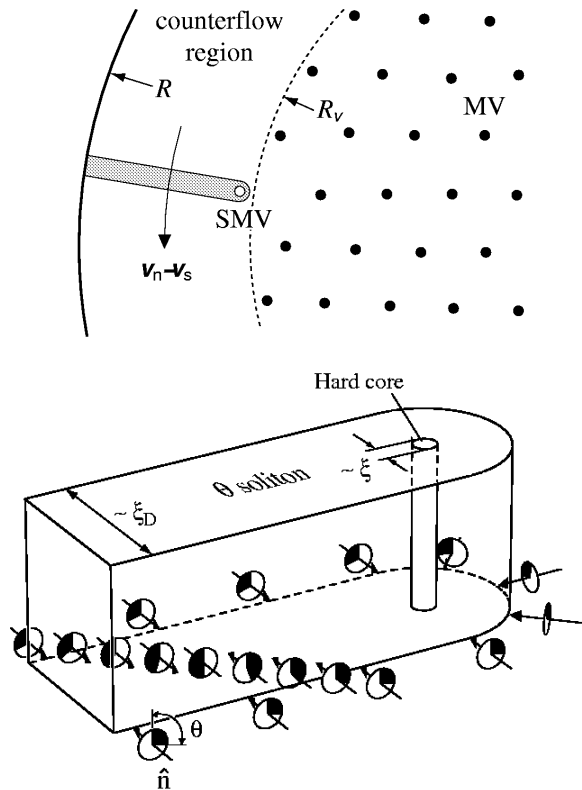


FIG. 17. (Top) The spin-mass vortex (SMV) is a composite object, which carries a trapped spin current as well as a mass current. In the rotating container it is confined by the Magnus force to the edge of the vortex cluster, which also includes other usual mass-current vortex lines (MV). The extension of the spin vortex into the bulk liquid is a soliton tail (grey strip). The spin-mass vortex itself provides one termination line of the soliton while its second end is anchored on the container wall. (Bottom) Inside the soliton the angle  $\theta$  changes through  $\pi$  while outside it is homogeneously at  $104^\circ$ . At the soliton surface the rotation axis  $\hat{n}$  is oriented perpendicular to the surface while further away it goes smoothly over into the flare-out texture of an ideal cylinder in an axially oriented magnetic field. The distortion of the  $\hat{n}$  texture from the flare-out configuration in the region around the soliton gives rise to the NMR signature of the spin-mass vortex in Fig. 16.

the conditions of the rotating NMR measurements is  $\xi_H \propto 1/H \sim 1$  mm. The NMR spectrum is an image of the  $\hat{n}$  texture in the cylindrical container. In an axially oriented magnetic field and an infinitely long cylinder, the texture is known to be of the “flare-out” form (Vollhardt and Wölfle 1990). In this texture there are no regions where  $\hat{n}$  would lie in the transverse plane perpendicular to the field  $\mathbf{H}$ . In contrast, at the soliton sheet  $\hat{n}$  is oriented strictly perpendicular to the sheet and thus to  $\mathbf{H}$ . This part of the texture is responsible for shifting NMR absorption into the region of maximum possible frequency shift and becomes thus the signature of the spin-mass vortex in the NMR spectrum (Fig. 16).

Fig. 16 illustrate the easy identification of the spin-

mass vortex. Here two NMR spectra are shown. The spectrum with the smaller counterflow peak was recorded first after the neutron irradiation and reveals the absorption at high frequency shifts, the characteristic signature from the soliton sheet. The second signal, obtained after decelerating just above the annihilation threshold, has no soliton signal and a counterflow peak which represents the cluster without the spin-mass vortex. Such a recovery back to the usual counterflow spectrum of an isolated vortex cluster provides simple proof for the spin-mass vortex.

The presence of the soliton sheet has thus many important experimental implications: It determines the location of the spin-mass vortex at the edge of the cluster and it leaves a clear signature in the NMR spectrum at high counterflow velocities when the sheet becomes stretched. It also affects the threshold velocity at which a spin-mass vortex might be expected to escape from the neutron bubble. This was only observed to happen well above  $v_{cn}$ , the threshold velocity for usual mass-vortex rings (Fig. 12). It is explained by the fact that for spontaneous expansion a spin-mass vortex loop has to exceed, in addition to the usual barrier formed by the line tension of the small loop, also the surface tension from the soliton sheet.

The spin-mass vortex was originally discovered as a defect which is formed when an A  $\rightarrow$  B transition front moves slowly close to adiabatic conditions through a rotating container (Kondo et al. 1992; Korhonen et al. 1993). In this experiment the initial A-phase state is one with the equilibrium number of doubly quantized singularity-free vortex lines while the final state is found to contain less than the equilibrium number of singly quantized B-phase vortex lines plus some number of spin-mass vortices. This means that A-phase vortex lines interact with the moving AB interface, they are not easily converted to B-phase vorticity, a critical value of counterflow velocity has to be exceeded before conversion becomes possible, and even then some fraction of the conversion leads to vorticity with the additional defect in  $R_{\alpha j}(\hat{n}, \theta)$  (Parts et al. 1993; Krusius et al. 1994). In the neutron measurements the spin-mass vortex was not observed at 2.0 bar, but at 18.0 bar. In the KZ scenario this is the pressure regime where the probability for the formation of A phase blobs in the neutron bubble increases (Fig. 14). Interestingly one might therefore surmise that even in the neutron bubble the spin-mass vortex could result from vorticity which originally was contained within the A-phase blobs and which is partly transferred to the B phase when the A phase blobs shrink away.

Although the spin-mass vortex is a rare event, compared to the yield of vortex lines in neutron irradiation, its various prominent features allow its unambiguous identification. Its presence demonstrates that in addition to usual mass-current vortices also other order-

parameter defects can be created in a neutron absorption event. It lends further support to the discussion in Sec. 2.8.3 that also the AB interface is among such defects. The presence of the spin-mass vortex among the products from the neutron absorption event limits the possible mechanisms of defect formation. An explanation in terms of the superflow instability, which takes place within a warm shell around the hot neutron bubble, is not a probable alternative: The spin-mass vortex is not normally created at the spontaneous critical velocity limit.

## 2.10. Vortex formation in gamma radiation

To study the dependence of the vortex formation rate  $\dot{N}$  on the dimensions of the heated neutron bubble in the  $^3\text{He-B}$  bath, it would be useful to investigate alternative heating methods. In addition to thermal neutrons, beta and gamma radiation have frequently been used as a source of heat. In the rotating experiments a  $^{60}\text{Co}$  gamma source was experimented with, which emits  $\gamma$  rays at 1.17 and 1.33 MeV energy.

A gamma ray, which scatters in the container wall or in the liquid  $^3\text{He}$  bath, knocks off a secondary electron which gives rise to the heat release in the liquid  $^3\text{He}$  bath. The interaction probability is roughly proportional to the density of the material and thus a large fraction of the secondary electrons originate from the quartz glass wall. Although the initial energies of the secondary electrons cover a broad spectrum, the variation in the effective heat release is narrower. Energetic electrons knock off additional electrons which produce their own ionization tracks. However, once the energy has dropped in the regime of several keV, the remaining ionization track is short: roughly the rate of energy loss per unit distance traveled increases inversely proportional to the electrons decreasing energy. Therefore the heating becomes concentrated within a distance  $\lesssim 10 \mu\text{m}$  of its final stopping point.

As a source for localized heating in liquid  $^3\text{He}$  experiments, gamma rays suffer from several shortcomings, compared to thermal neutrons: 1) It is not possible to concentrate on single heat-release events, since many secondary electrons can be produced by a single  $\gamma$  ray. Thus there is more variation in these events. For instance, the endpoints of different ionization tracks may fall close to each other and may merge to produce a large hot bubble of variable size. 2) The events are not localized in a well-determined location within the container. 3) It is not only the liquid  $^3\text{He}$  bath which preferentially absorbs the heat, but even more so the structural materials of the refrigerator. This interferes with the temperature control of the measurements, the heating produced by the  $\gamma$  radiation in the metal parts of the cryogenic equipment

may rise to excessive levels, and radiation shielding and collimation need to be built into the experiment.

It was found that qualitatively vortex formation in gamma and neutron radiation are similar. But the measurements also showed that the quantitative differences are large: the threshold velocity  $v_{\text{cn}}$  is substantially increased and thus the yield  $\dot{N}(\Omega)$  at a given rotation velocity  $\Omega$  in the vortex-free state is smaller. So far no careful quantitative measurements have been carried out with  $\gamma$  radiation.

## 2.11. Bias dependence of loop extraction

The dependence of the vortex formation rate  $\dot{N}$  on the externally applied bias  $v$  is the most tangible quantitative result from the rotating measurements. It will be described and analyzed below (Ruutu et al. 1998a). The empirical rate equation (8) is shown to be consistent with the KZ model, including the measured value of the prefactor  $\alpha$ .

### 2.11.1. Experimental velocity dependence

The frequency and number of vortex lines can be counted from the accumulation record (Figs. 3, 11) where the NMR absorption is monitored as a function of time during neutron irradiation. Fig. 18 shows the vortex formation rate  $\dot{N}$  (*top*), the number of those neutron absorption events  $\dot{N}_e$  which produce at least one line and thus become observable (*middle*), and the number of lines extracted from each absorption event (*bottom*). All three rates are determined independently and directly from the absorption records. In Fig. 18 the results are plotted as a function of the normalized bias  $v/v_{\text{cn}}$ . To construct the plot, the horizontal axis was divided into equal bins from which all individual measurements were averaged to yield the evenly distributed data points displayed in the graphs.

The rates in Fig. 18 are proportional to the intensity of the neutron flux, which is contained in the prefactors of the expressions given in the different panels of the figure. For counting the rates from the NMR absorption records it is vital that absorption events do not start to overlap, when the applied counterflow velocity is increased. Therefore three different source positions were used which were scaled to the same distance using the measured graph in Fig. 7.

The rates in Fig. 18 increase rapidly with the applied counterflow velocity  $v$ : At  $v/v_{\text{cn}} \approx 4.5$ , close to the maximum velocity limit imposed by the spontaneous instability limit (Fig. 12), there are almost no unsuccessful (or unobserved) absorption events left:  $\dot{N}_e(\infty) - \dot{N}_e(4.5v_{\text{cn}}) \approx 0$ . Also we note that in agreement with the scaling properties expressed by the rate equation (8),

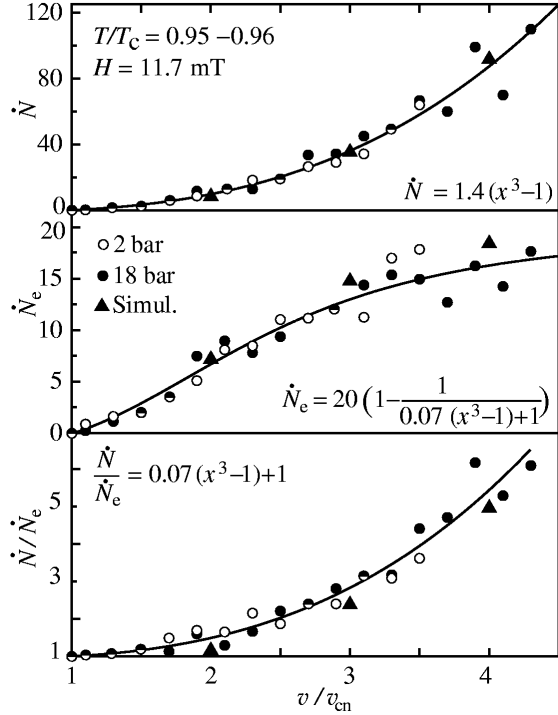


FIG. 18. Rates of vortex line formation plotted *vs* normalized counterflow velocity  $x = v/v_{cn}$ : (*Top*) the total number of lines  $\dot{N}$  formed per minute, (*middle*) the number of observed neutron absorption events  $\dot{N}_e$  per minute, and (*bottom*) the number of lines per event ( $\approx \dot{N}/\dot{N}_e$ ). All three rates have been determined *independently* from discontinuities in the NMR absorption as shown in Fig. 3. The solid curves are fits to the data, given by the expressions in each panel. Triangles are result of numerical simulations described in Sec. 2.13. (From Ruutu et al. 1998a).

measurements at the two pressures of 2 and 18 bar fall on the same universal curves.

The most detailed information from the rate measurements is the dispersion into events in which a given number of lines is formed. Fig. 19 displays the rates  $\dot{N}_i$  of events which produce  $i = 1-5$  lines. This data exhibits larger scatter, owing to its statistical variation, but again after averaging one gets for each value of  $i$  a curve, which peaks at a maximum, and then trails off. With increasing value of  $i$  the curves shift to successively higher velocities. The starting points of each curve, the threshold velocity  $v_{cni}$ , are plotted in the inset. Their values increase monotonically with each consecutive value of  $i$ . This means that at and immediately above the first threshold,  $v_{cn} = v_{cn1}$ , only single-vortex events occur.

A surprising finding from the measurements was the total absence of a background contribution to the measured rates. A number of tests were performed to look for spontaneous events in the absence of the neutron source, to check whether a contribution from the background radiation level should be subtracted from the measured rates.

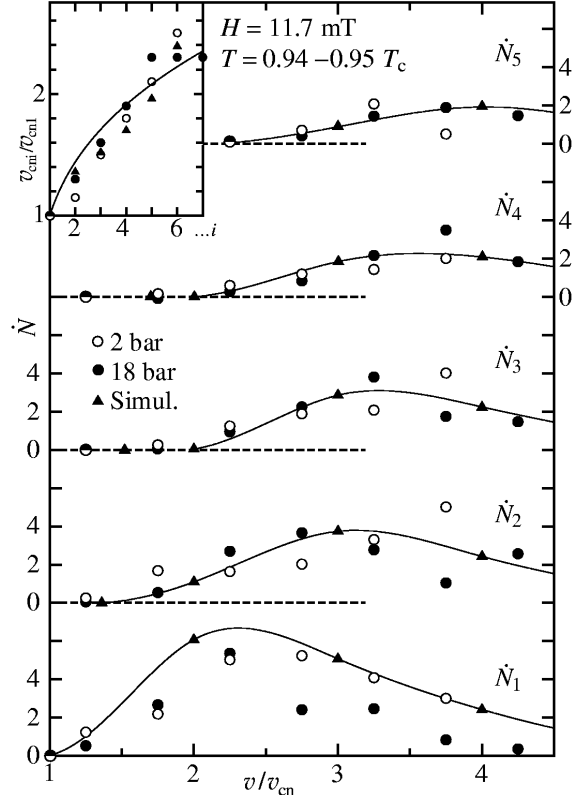


FIG. 19. Rates  $\dot{N}_i$  of vortex line formation, grouped according to the number of lines  $i$  formed per absorption event per minute, plotted *vs*  $v/v_{cn}$ . Triangles are result of numerical simulations described in Sec. 2.13. The solid curves are spline fits to simulation data. (*Inset*) Threshold velocity  $v_{cni}/v_{cn1}$  for the onset of an event with  $i$  lines, plotted *vs* the number of lines  $i$ . The solid curve represents the fit  $v_{cni}/v_{cn1} = [2.0(i - 1) + 1]^{1/3}$ . (From Ruutu et al. 1998a).

For instance, a vortex-free sample was rotated for 90 min at different velocities (0.9, 1.3, and 2.1 rad/s at 2.0 bar and 0.94  $T_c$ ), but not a single event was noted.

### 2.11.2. Analytic model of vortex loop escape

An analytic calculation can be constructed for independent vortex loops in the applied flow, which explains the cubic velocity dependence of the escape rate in Fig. 18. Vortex rings, which are part of the random vortex network after the quench, each have a critical diameter (Eq. (11)) below which they contract and above which they expand spontaneously in homogeneous superflow. By comparing this diameter to the typical loop sizes in the random network, we arrive at the desired result (Ruutu et al. 1996a).

During the quench through the superfluid transition a random vortex network is formed with a characteristic length scale of the order of  $\xi_v$ . The later evolution of the

network leads to a gradual increase in this length. The average intervortex distance or, equivalently, the typical diameter of curvature of the loops increases with time. We shall call this length  $\tilde{\xi}(t)$ . This ‘‘coarse-graining’’ process preserves the random character of the network, in other words the network remains self similar or scale invariant. Only later a change occurs in this respect, when the loops become sufficiently large to interact with the externally applied counterflow field: This causes large loops to expand, if they are oriented transverse to the flow with the correct winding direction, while in the opposite case with the wrong sign of circulation the flow causes the loops to contract. The time scale of all these processes is determined by the magnitude of mutual friction between the normal and superfluid components. At very low temperatures  $T \ll T_c$  the evolution can be slow, but in the temperature range of the rotating experiments the scale is milliseconds.

In superfluid  $^3\text{He}$  the large viscosity of the normal component clamps it to corotation with the container. In the rotating frame of reference we may write  $v_n = 0$  and  $v_s = v$ . The energy of a vortex loop, which is stationary with respect to the walls, is given by (Donnelly 1991)

$$\mathcal{E} = E_{\text{kin}} + \mathbf{p}\mathbf{v}, \quad (16)$$

where  $\mathbf{v}$  is the velocity of the applied superflow. In simple configurations, the hydrodynamic kinetic energy or self-energy of the loop arises from the trapped superfluid circulation with the velocity  $v_{s,\text{vort}}$ ,

$$E_{\text{kin}} = \frac{1}{2} \int \rho_s v_{s,\text{vort}}^2 dV = \varepsilon L, \quad (17)$$

and is proportional to the length  $L$  of the loop and its line tension,

$$\varepsilon = \frac{\rho_s \kappa^2}{4\pi} \ln \frac{\tilde{\xi}(t)}{\xi}. \quad (18)$$

Here we neglect the small contribution from the core energy, use  $\tilde{\xi}(t)$  for the diameter of the loop, and the superfluid coherence length  $\xi(T, P)$  for the diameter of the core. This equation is valid in the logarithmic approximation, when  $\tilde{\xi}(t) \gg \xi(T, P)$ . While the first term in Eq. (16) is proportional to the length  $L$  of the loop, the second term involves its linear momentum,

$$\mathbf{p} = \int \rho_s \mathbf{v}_{s,\text{vort}} dV = \frac{1}{2\pi} \rho_s \kappa \int \nabla \Phi dV = \rho_s \kappa \mathbf{S}, \quad (19)$$

where  $S$  is the area of the loop in the direction of the normal  $\mathbf{S}/S$  to the plane of the loop.

Thus we write for the energy of a loop

$$\mathcal{E}(L, S, t) = \rho_s \kappa \left[ L \frac{\kappa}{4\pi} \ln \frac{\tilde{\xi}(t)}{\xi} - vS \right], \quad (20)$$

where  $S$  is the algebraic area, perpendicular to the flow and of proper winding direction. This equation expresses the balance between a contracting loop due to its own line tension, which dominates at small applied velocities, and expansion by the Magnus force from the external superflow, which dominates at high applied velocities. The divide is the equilibrium condition, which was expressed by Eq. (11) and corresponds to the situation when the height of the energy barrier, which resists loop expansion, vanishes. In this extremal configuration  $\mathbf{p}$  is antiparallel to  $\mathbf{v}$ , the loop moves with the velocity  $-\mathbf{v}$  in a frame of the superfluid component, but is stationary in the rotating frame. In a more general sense, if we consider loops in the random network which still deviate from circular shape, the extremal case degenerates to a saddle point. This is because the extremum requires also minimization with respect to deviations from circular shape, ie. the total energy is invariant under small variations of the radius of the ring, or  $\delta\mathcal{E} = \delta E_{\text{kin}} + \mathbf{v} \cdot \delta\mathbf{p} = 0$ .

The expansion of the vortex loop should be calculated by including the mutual friction forces. In our analytic description of vortex loop escape we shall neglect such complexity. Instead we shall make use of three scaling relations which apply to Brownian networks and are described in more detail in Sec. 2.13. These expressions relate the mean values in the statistical distributions of the loop diameter  $\mathcal{D}$ , area  $S$ , and density  $n$  to the length  $L$  of the loop:

$$\mathcal{D} = AL^\delta \tilde{\xi}^{1-\delta}, \quad (A \approx 0.93, \delta \approx 0.47), \quad (21)$$

$$|S| = BD^{2-\zeta} \tilde{\xi}^\zeta, \quad (B \approx 0.14, \zeta \approx 0), \quad (22)$$

$$n = CL^{-\beta} \tilde{\xi}^{\beta-3}, \quad (C \approx 0.29, \beta \approx 2.3). \quad (23)$$

For a Brownian random walk in infinite space the values of  $\delta$ ,  $\beta$  and  $\zeta$  are 1/2, 5/2 and 0.

The important assumption is that these relations are valid during the entire evolution of the network, until sufficiently large rings are extracted by the counterflow into the bulk. Using Eqs. (21) and (22), we may write Eq. (20) for the energy of a loop in the form

$$\mathcal{E}(\mathcal{D}, t) = \rho_s \kappa \mathcal{D}^2 \left[ \frac{\kappa}{4\pi \tilde{\xi}(t) A^2} \ln \frac{\tilde{\xi}(t)}{\xi} - vB \right]. \quad (24)$$

When the mean diameter  $\tilde{\xi}(t)$  exceeds a critical size  $\tilde{\xi}_c(v)$ , which depends on the particular value of the applied superflow velocity  $v$ ,

$$\tilde{\xi}_c(v) = \frac{1}{A^2 B} \frac{\kappa}{4\pi v} \ln \frac{\tilde{\xi}_c}{\xi}, \quad (25)$$

the energy in Eq. (24) becomes negative and the loop starts expanding spontaneously. This is the smallest loop

which will be able to expand at a given value  $v$  of the applied superflow. The upper cutoff for the loop size distribution is provided by the diameter of the entire network, or that of the heated bubble,  $2R_b$ , such that  $\tilde{\xi}_c(v_{cn}) = 2R_b$ . The total number of loops  $N_b$ , which will be extracted from one neutron bubble, can then be obtained from

$$N_b = V_b \int_{\tilde{\xi}_c}^{2R_b} d\mathcal{D} n(\mathcal{D}) . \quad (26)$$

Here the density distribution  $n(L) = C \tilde{\xi}^{-3/2} L^{-5/2}$ , combined with that for the average diameter  $\mathcal{D}(L) = A (L \tilde{\xi})^{1/2}$ , gives  $n(\mathcal{D}) d\mathcal{D} = 2A^3 C \mathcal{D}^{-4} d\mathcal{D}$ . On inserting this into the integral (26) we obtain

$$N_b = \frac{1}{9} \pi A^3 C \left[ \left( \frac{2R_b}{\tilde{\xi}_c} \right)^3 - 1 \right] . \quad (27)$$

From this equation we see that the requirement  $N_b(v_{cn}) = 0$  returns us the definition of the threshold velocity  $v_{cn}$ :  $\tilde{\xi}_c(v = v_{cn}) = 2R_b$ . This in turn gives us from Eq. (25) for the radius of the heated bubble

$$R_b = \frac{1}{A^2 B} \frac{\kappa}{8\pi v_{cn}} \ln \frac{2R_b}{\xi(T, P)} , \quad (28)$$

which we used in Sec. 2.8.1 to derive the temperature dependence of the threshold velocity:  $v_{cn} \propto (1 - T/T_c)^{1/3}$ .

Eqs. (25) and (28) thus show that  $\xi_c \propto 1/v$  and  $R_b \propto 1/v_{cn}$ , so that we may write for the vortex-formation rate  $\dot{N} = \phi_n N_b$  from Eq. (27)

$$\dot{N} = \frac{1}{9} \pi A^3 C \phi_n \left[ \left( \frac{v}{v_{cn}} \right)^3 - 1 \right] , \quad (29)$$

where  $\phi_n$  is the neutron flux. This is the form of the measured cubic velocity dependence in the empiric Eq. (8). By inserting  $A \approx 0.93$ ,  $C \approx 0.29$  from Eqs. (21) and (23) respectively and  $\phi_n \approx 20$  neutrons/min, as determined from the saturation of the event rate  $\dot{N}_e$  in the center panel of Fig. 18, we obtain for the prefactor in Eq. (29)  $\alpha \approx 1.6 \text{ min}^{-1}$ , which agrees with the experimental value in Figs. 10 and 18. We note that the cubic dependence on the applied counterflow in Eq. (29) comes only from the assumption that the whole volume of the heated bubble contributes equally to the outcome of vortices. On the other hand, the values of the prefactor and of the constant term in Eq. (29) depend on the particular scaling relations (21–23).

The definition of the threshold velocity  $v_{cni}$ , which applies for an event in which  $i$  rings are formed simultaneously, is roughly consistent with the requirement  $N_b(v = v_{cni}) \approx i$ . This gives  $v_{cni}/v_{cn} \sim i^{1/3}$ , which agrees with the measured result in Fig. 19.

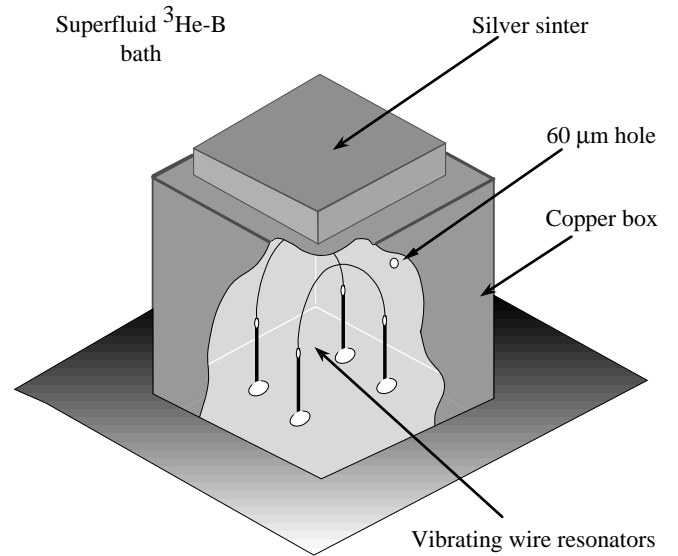


FIG. 20. Bolometer box, which is used in the  $^3\text{He-B}$  bath in the very low temperature regime of ballistic quasiparticle motion. Two vibrating superconducting wire loops are included, one for measuring the temperature of the liquid within the box and the other as a heater to calibrate a calorimetric measurement. (From Bäuerle et al. 1998b).

In summary, one finds that the KZ model, combined with the simplest possible interpretation for the loop escape from a random vortex network, reproduces both the measured cubic dependence on the normalized velocity,  $(v/v_{cn})^3$ , and the magnitude of the extraction rate.

## 2.12. Calorimetry of vortex network

The calorimetric measurements of Bäuerle et al. (1996, 1998a) calibrate the amount of heat which is dumped into the liquid  $^3\text{He-B}$  bath in each individual neutron absorption event. They allow another quantitative comparison to the KZ model. These measurements are performed in the very low temperature limit of ballistic quasiparticle motion.

The measuring probe is a superconducting wire loop. It is oscillated in the liquid with a frequency of a few hundreds Hz and a high Q value, by driving the loop at resonance with an ac current in a dc magnetic field oriented perpendicular to the wire. The damping of the wire oscillations measures the density of quasiparticle excitations in the liquid and can be calibrated to give the temperature. For this a second vibrating wire loop is used as a heater (Fig. 20). The latter is excited with a known current pulse to heat up the liquid, by driving the wire at supercritical velocities where the break-down of Cooper pairs gives rise to a shower of quasiparticles. To contain the ballistically moving quasiparticles, both wire loops are placed inside a box from which the par-

	$P$ (bar)			Source
	0	6	19.4	
$\Delta E$ exper. (keV)	85	95	150	Bäuerle et al. (1996, 1998a)
$T_c$ (mK)	0.93	1.56	2.22	Greywall (1986)
$v_F$ ( $10^3$ cm/s)	5.95	5.04	3.94	Greywall (1986)
$C_v$ [ $10^3$ erg/( $\text{cm}^3$ K)]	5.83	12.8	25.4	Greywall (1986)
$\xi_0$ (nm)	65	33	18	$\xi_0 = \sqrt{7\zeta(3)/(48\pi^2)} \hbar v_F / (k_B T_c)$
$\tau_0$ (ns)	1.1	0.65	0.46	$\tau_0 = \xi_0 / v_F$
$R_b$ ( $\mu\text{m}$ )	27	17	12	$R_b = \sqrt{\frac{3}{2\pi e}} \left( \frac{E_0}{C_v(T_c - T_0)} \right)^{1/3}$
$\tau_T$ ( $\mu\text{s}$ )	0.59	0.17	0.12	Wheatley (1975)
$D$ ( $\text{cm}^2/\text{s}$ )	21	4.3	0.94	$D = v_F^2 \tau_T$
$\tau_Q$ ( $\mu\text{s}$ )	0.16	0.31	0.69	$\tau_Q = (e/6) R_b^2 / D$
$\xi_v$ ( $\mu\text{m}$ )	0.23	0.15	0.11	$\xi_v = \xi_0 (\tau_Q / \tau_0)^{1/4}$
$\tilde{D}_b$	210	200	190	$\tilde{D}_b = \left( \frac{4}{3} \pi R_b^3 / \xi_v^3 \right)^{1/3}$
$L_v$ (cm)	79	43	28	$L_v = (4\pi/3a_l) R_b^3 / \xi_v^2$
$\rho_s$ ( $\text{g}/\text{cm}^3$ )	0.081	0.094	0.108	$\rho_s \approx \rho$ , Greywall (1986)
$\Delta E$ theor. (keV)	170	140	120	$\Delta E = (\rho_s \kappa^2 / 4\pi) L_v \ln(\xi_v / \xi_0)$

TABLE I. Comparison of measured and estimated total vortex line energies at different pressures in a random vortex network, as expected after a neutron absorption event according to the KZ model. The ambient temperature of the  $^3\text{He}$ -B bath is taken to be  $T_0 = 0.16$  mK. For the value of  $\tau_Q$  we use the time it takes for the normal phase bubble to disappear. The coefficient  $a_l = 2.1$ , for estimating the total vortex-line length  $L_v$ , is taken from the simulation results in Sec. 2.13.1, when the value of the dimensionless bubble diameter is  $\tilde{D}_b = 200$ .

ticles leak out through a pin hole at a well-known rate (Bäuerle et al. 1998b).

The thermal connection between the liquid in the calorimeter box and that in the surrounding  $^3\text{He}$ -B bath is only via the small pin hole. A neutron absorption event inside the box heats up the liquid and a thermal pulse is recorded with the wire resonator. The rise time is determined by the resonator properties, while the trailing edge (with a time constant of about 1 min) monitors the much slower leakage of the quasiparticle excitations from the box through the orifice. Thus if energy is released into the box at a still longer time constant it is not recorded in the form of pulses.

It is found that neutron absorption events amount to roughly 100 keV smaller thermal pulses than the 764 keV, which a slow neutron is expected to yield for the absorption reaction with a  $^3\text{He}$  nucleus. Since the various recombination channels of the ionized charge and the subsequent thermalization processes in liquid  $^3\text{He}$  are poorly known, it is not quite clear how large an energy deficit one should expect. Obvious losses include the ultraviolet radiation absorbed in the walls of the bolometer box and the retarded relaxation of excited electronic states of helium atoms and molecular complexes. However, Bäuerle

et al. (1996, 1998a) expect that this contribution is not strongly pressure dependent and on the order of 3 % of the reaction energy. They then ascribe the remaining energy deficit to the random vortex network which is created in the neutron bubble and which in the very low temperature limit has a long life time when mutual friction approaches zero.

In Table I the measured missing energy at three different liquid pressures has been compared to that estimated from the KZ model. The measured result  $\Delta E_{\text{exp}}$  is recorded on the top most line while the calculated comparison proceeds stepwise from one line to the next in the downward direction of the table. The final result  $\Delta E_{\text{theor}}$  can thus be found on the lower most line. The thermal diffusion constant  $D = 3k_T/C_v = v_F^2 \tau_T$  is derived from the conductivity  $k_T$ , which has been tabulated by Wheatley (1975) while all other basic liquid  $^3\text{He}$  values are taken from Greywall (1986). The agreement between the top and bottom lines, which is within a factor of 2, can be regarded as surprising, if we remember the uncertainties which are built into this comparison.

Table I has been included in this context to illustrate the magnitudes of the different quantities. However, it is again indicative of the fact that rough agreement be-

tween experiment and the KZ model can be claimed on the quantitative level. Nevertheless, a number of other alternative interpretations can also be offered. In the next sections we shall analyze some further aspects of loop formation and escape which we now have omitted.

### 2.13. Simulation of loop extraction

In spite of the good agreement of the measured neutron-induced vortex formation rate with the KZ model, a deeper understanding of the processes involved would be important. Owing to its phenomenological content, the KZ model is based on general concepts and contains only few media parameters (such as the superfluid coherence length  $\xi$  or the order-parameter relaxation time  $\tau$ ). These are known in the case of superfluid  $^3\text{He}$ , hence the predictions of the model for the initial state of the vortex network can be calculated. In the rotating experiments the initial state is connected with observable quantities only through the complex evolution of the network, governed by superfluid hydrodynamics. This means that a more rigorous comparison requires numerical simulation.

A number of numerical simulations exist today on the evolution of a network of linear defects. These apply to cosmic strings, liquid crystals, and vortices in superfluid  $^4\text{He}$ . However, such results cannot be directly transferred to neutron-induced vortex formation in  $^3\text{He-B}$ . The differences with the cosmic string and liquid crystal calculations arise from the different boundary conditions and the equations which govern the evolution of the network in the applied external bias fields. In the case of superfluid  $^4\text{He}$ , studies of random vortex networks often concentrate on vortex flow driven by thermal normal-superfluid counterflow in a stationary situation (Tough 1982). In contrast, the vortex network, which is produced in  $^3\text{He-B}$  in a neutron absorption event, is in a state of rapid non-stationary evolution. However, in the course of the  $^4\text{He}$  studies the techniques have been developed (Schwarz 1978, 1985, 1988) for solving also the transient problem in  $^3\text{He-B}$ . Here we describe preliminary calculations which address the dependence of the vortex-formation rate on the normalized counterflow velocity  $x = v/v_{\text{cn}}$  (Ruutu et al. 1998a).

#### 2.13.1. Initial loop distribution

Vachaspati and Vilenkin (1984) developed an approach for the simulation of the initial network of linear defects after a rapid phase transition, adapted for the case of cosmic strings. This technique has been used in most studies since then (see e.g. the reviews by Hindmarsh and Kibble 1995a and Bray 1994).

We approximate the neutron bubble with a cubic volume which is subdivided into smaller cubes, such that the size of these volume elements equals the length scale of the initial inhomogeneity in the order-parameter distribution at the moment of defect formation. This length is on the order of the coherence length and in the simulation it plays the role of a “unit” length: It is a parameter of the model, which has to be derived by other means. In the case of the superfluid transition this length is given by Eq. (3).

An arbitrary phase is assigned to each vertex of the grid, to model the initial random inhomogeneity of the order parameter. It is usually assumed that the distribution of the phase in each segment of the grid between two vertices corresponds to the shortest path in the phase circle. Thus it is possible to determine whether a line defect pierces a given face. Then the centers of the corresponding faces are connected to form closed or open (depending upon specific boundary conditions) linear defects, strings in the cosmological case and vortices in the superfluid.

Vachaspati and Vilenkin assigned to each vertex a value of the phase from the following set:  $\{0, 2\pi/3, 4\pi/3\}$  and then studied the statistical properties of the resulting network of strings. They found that most (70%) of the strings were in the form of open segments, which extended from one boundary of the system to another. For closed loops they found two scaling relations to hold:

$$n = CL^{-\beta}, \quad (30)$$

and

$$\mathcal{D} = AL^\delta, \quad (31)$$

where  $\beta \approx \frac{5}{2}$ ,  $\delta \approx \frac{1}{2}$ ,  $n$  is the density of loops with a given length  $L$ , and  $\mathcal{D}$  is the average spatial size of a loop. It is usually defined as an average of straight-line dimensions in  $x$ ,  $y$  and  $z$  directions. In this model both the characteristic inter-vortex distance and the radius of curvature are on the order of the length scale of the spatial inhomogeneity (i.e. the size of the small cubes, which here has been set equal to unity). Later, other variations of this model have been studied, including other types of grids and other sets of allowed phases. However, it has been found that the scaling relations (30) and (31) hold universally in each case.

The direct applicability of these results to the case of vortex formation in  $^3\text{He-B}$  is not evident. In cosmology the open lines are the most significant ones: only these strings may survive during the later evolution if no bias field exists to prevent closed loops from contracting and annihilating. In the case of a normal-liquid bubble within the bulk superfluid there exists an obvious boundary condition: the phase is fixed at the boundary and there are no open lines at all. Thus it is of interest to find out the influence of the boundary conditions on the scaling relations (30) and (31).

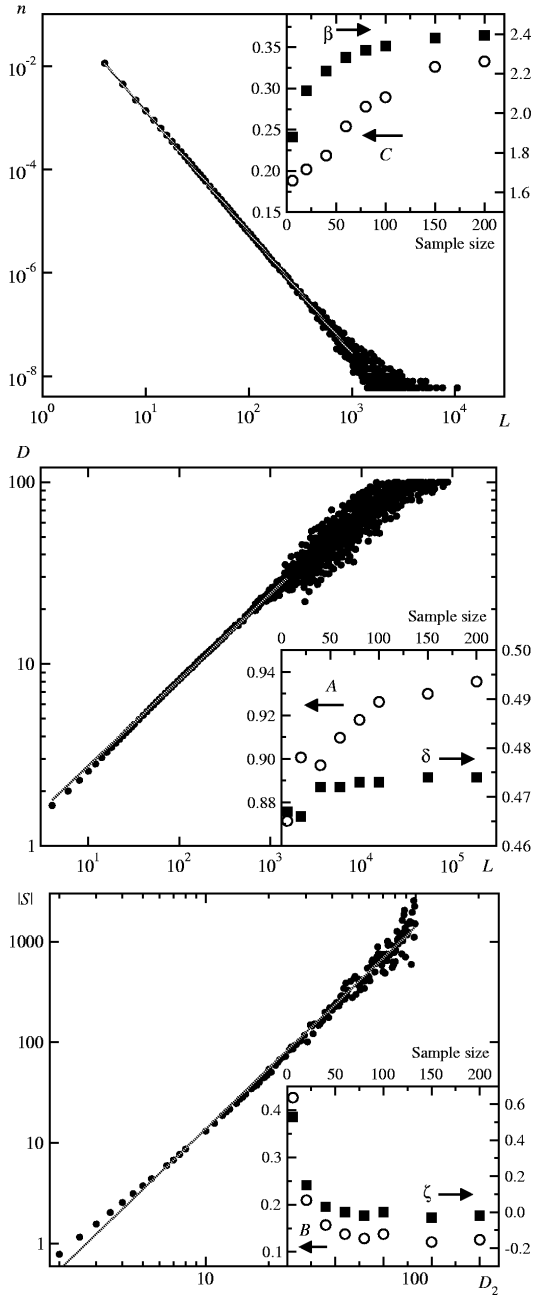


FIG. 21. Scaling properties of vortex loops in the initial network: density  $n$  (*top*) and average spatial size  $D$  (*middle*), plotted as a function of the length  $L$  of the loops. Below their algebraic area  $|S|$  is shown (*bottom*), as a function of the 2-dimensional spatial size  $D_2$  of the loop. The calculations are performed on a lattice of  $100 \times 100 \times 100$  cells. The solid lines are fits to scaling laws obeying equations of the form of (30), (31), and (32), respectively. The inset in each plot shows the dependence of the scaling parameters on the size of the cubic neutron “bubble”.

Another question, which arises in the case of superfluid vortices, concerns the interaction of the loops with the external bias field due to the normal-superfluid counterflow.

The energy of a tangled vortex loop in the counterflow is proportional to its algebraic area  $S = \oint y dz$  in the direction  $x$  of the counterflow velocity, Eq. (20). Thus the dependence of  $S$  on the length of the loop is of interest as well.

The simulation is performed in a cubic lattice with a fixed (zero) phase at the outer boundary. The set of allowed phases is not limited. It is known that such limitations affect the number of open lines in cosmic-string simulations, but this should be irrelevant for the network in the neutron bubble. Several vortices may pass through one cell in the grid. In this case the corresponding faces of the cell are connected at random. For calculating the length of a loop, it is assumed that both straight and curved segments of the loop inside one cell have unit length. The size of a loop in the direction of a specific coordinate axis is measured as the number of cells in the projection of the loop along this axis.

The size of the volume, which undergoes the superfluid transition in the neutron absorption event, is about  $50 \mu\text{m}$ , while the characteristic inter-vortex distance in the initial network is of the order of  $1 \mu\text{m}$ . Calculations have been performed for several “bubble” volumes: starting from  $6 \times 6 \times 6$  up to  $200 \times 200 \times 200$ . For each bubble size the loop distributions obtained from a large number of (up to 1000) initial distributions of random phases are averaged. The resulting distributions of  $n$ ,  $D$ , and  $S$  are shown in Fig. 21. One can see that despite differences in the boundary conditions the Vachaspati-Vilenkin relations (30) and (31) hold in the case of vortices in superfluid helium, but the exponents and prefactors are slightly different and depend on the size of the bubble.

For the algebraic area  $S$  of a loop as a function of the corresponding 2-dimensional diameter  $D_2$  the additional scaling law is

$$|S| = B D_2^{2-\zeta}, \quad (32)$$

where  $\zeta \approx 0$ . Here  $D_2$  is the average of the straight-line dimensions of a loop in  $y$  and  $z$ -directions. Thus the oriented area of a tangled loop is proportional to the area of a circle of the same straight-line size. The scaling relation (32), as well as (30) and (31), are of the form expected for a Brownian particle, for which the square of the average displacement on the  $i$ -th step is proportional to  $i$  and therefore the mean value of the square of the oriented area is given by

$$\begin{aligned} \langle S^2 \rangle &= \left\langle \left( \sum_{1 \leq i \leq L} y_i \Delta z_i \right)^2 \right\rangle = \sum_{1 \leq i, j \leq L} \langle y_i \Delta z_i y_j \Delta z_j \rangle = \\ &= \sum_{i, j} \langle y_i y_j \rangle \langle \Delta z_i \Delta z_j \rangle = \sum_i \langle y_i^2 \rangle \langle \Delta z_i^2 \rangle \propto \sum_i i \propto L^2 \quad . \end{aligned}$$

These scaling relations were already used in the analytic description of vortex-loop extraction [ie. Eqs. (21) – (23)].

### 2.13.2. Network evolution under scaling assumptions

After its formation, the vortex network evolves under the influence of the inter-vortex interactions and the normal-superfluid counterflow  $v$ . Its characteristic length scale  $\tilde{\xi}(t)$  increases with time. Vortices start to escape from the bubble when the energy gain due to the external counterflow becomes larger than the energy of the superflow associated with the vortex itself. This corresponds to the critical value of  $\tilde{\xi}$ , expressed by Eqs. (11) or (25).

Tangled vortex flow in superfluid  $^4\text{He}$  has been studied numerically by Schwarz (1978, 1985, 1988), Samuels (1992), Aarts and de Waele (1994), Nemirovskii and Fiszdon (1994), Barenghi et al. (1997), Tsubota and Yoneda (1995), and others. A large number of calculations has been devoted to the evolution of the initial network of cosmic strings (see reviews by Hindmarsh and Kibble (1995a), Bray (1994)) and also of linear defects in liquid crystals (Toyoki 1994; Zapotocky et al. 1995). In all three cases the initial state is quite similar, but the equations controlling the evolution are different. The common feature is that the interaction between the loops leads to reconnections when the loops cross each other. It has been shown by Kagan and Svistunov (1994) that the scaling relations remain valid in a random network if the vortices are allowed to reconnect when they cross each other, but all other interactions are neglected for simplicity. In most simulation work, both in the case of cosmic strings and liquid crystals, it has been found that the scaling relations are preserved during the evolution even when the inter-vortex interactions are included.

To calculate the escape rate from the network, two crude assumptions are made, which are essentially the same as in the analytic treatment in Sec. 2.11.2: 1) We assume that the scaling laws remain valid until  $\tilde{\xi}$  grows comparable in size to the critical value in Eq. (25). 2) At this point the influence of the external counterflow becomes suddenly so significant that all sufficiently large loops immediately escape by expanding to a rectilinear vortex line. In the numerical simulations the state before escape is modelled by the same method as was used to construct the initial state. It is assumed that not only the scaling relations but also the statistical properties of the vortex tangle remain the same during the evolution as in the “initial” state with the characteristic length  $\tilde{\xi}$ .

At the moment of escape,  $\tilde{\xi} \sim r_o \propto v_{\text{cn}}/v = 1/x$ , and  $\tilde{\xi}$  is used as the size of a cell in the Vachaspati-Vilenkin method. For integer values of  $x$  the bubble is represented by a grid with  $x \times x \times x$  vertices and a random phase is assigned to each vertex. To satisfy the boundary condition, this grid is surrounded by a shell of vertices with fixed zero phase, representing the uniform bulk superfluid outside the heated bubble. Thus the whole grid contains  $(x+1) \times (x+1) \times (x+1)$  cells. Such a correspondence

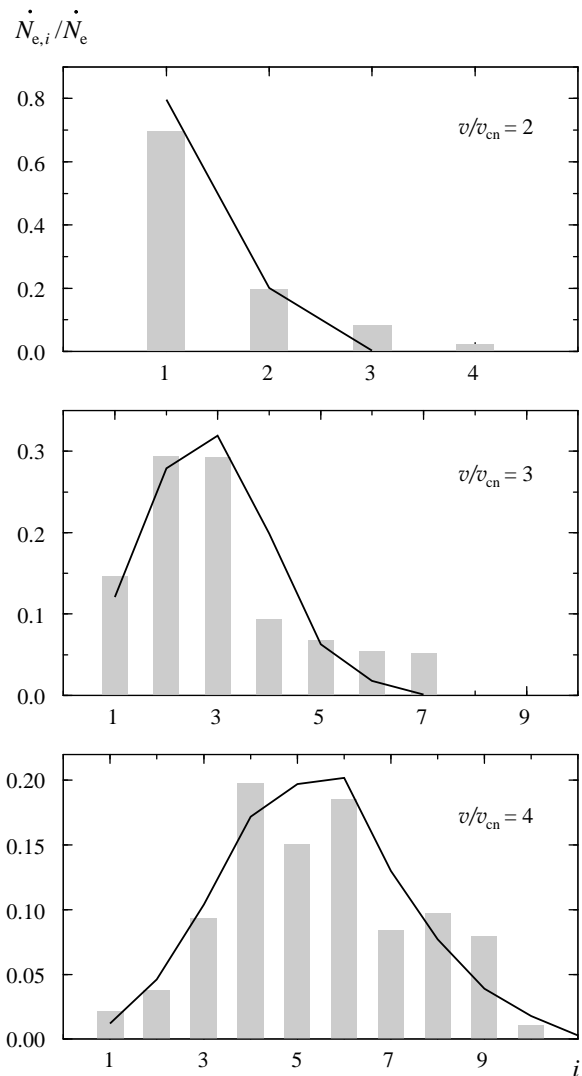


FIG. 22. Distribution of the number of loops escaping per absorption event, normalized to the total number of absorption events and given at three different values of the external bias field,  $v/v_{\text{cn}}$ . The solid lines represent the simulations while the bars denote the experiment.

between the size of the grid and the velocity is not too artificial even at small values of  $x$ : for example, at the critical velocity  $v = v_{\text{cn}}$  one gets a grid with  $(x+1)^3 = 8$  cells and  $3 \times 3 \times 3$  vertices, but the phase can be non-zero only at one vertex in the middle of the grid. In this case no vortices can appear in agreement with the definition of  $v_{\text{cn}}$ .

By counting the vortex lines produced from a number of random-phase distributions it is possible to calculate the probability distribution for the number of loops escaping per absorption event. For these calculations it is assumed that each loop, which survives until the moment when  $\tilde{\xi} \sim r_o$ , will form an observable vortex line: In the case of a tangled loop the probability is high that

at least one arc is oriented favorably with respect to the counterflow and will be extracted.

In Fig. 22 the calculated probability distribution is plotted for observed neutron absorption events at different values of  $x$  ( $x = 2, 3$ , and  $4$ ) expressed as the fraction of those neutron absorption events which produce a given number of vortices, normalized by the number of all events which give rise to at least one vortex. These results are in remarkably good agreement with the experimental data (without any fitting parameters). However, the agreement with the fraction of “zero” events, i.e. absorption events which produce no vortices at all, is poorer, underestimating their number, especially at  $x = 2$ . Experimentally the “zero” events can be extracted from the measured data by comparing the event rate at a given rotation velocity with the saturated event rate at the highest velocity.

One reason for this discrepancy is that at low  $R_b/r_o$  ratio (ie. at low velocities) loops with a radius of curvature  $\sim r_o$ , which are capable of escape into the bulk superfluid, have a rather large probability to be oriented in such a way that they do not have sufficiently large segments oriented favorably with respect to the counterflow, owing to space constraints. Hence they contract and do not give a contribution to the observed signal. Taking this into account one could develop more elaborate techniques for counting vortices than the simple “count all” method described above. In this case better agreement with all experimental data could be achieved. Particularly, if only vortices with positive algebraic area with respect to the counterflow ( $S = \oint y dz$ ) are counted, then good agreement with the number of “zero” events would be obtained. However, such refinements do not change the results essentially, compared to uncertainties of the model.

### 2.13.3. Direct simulation of network evolution

There is no direct evidence for the validity of the assumptions, which were made in the previous section about the evolution of the network, ie. whether the network remains self-similar (or scale invariant) and the scaling laws Eqs. (30) – (32) can be applied during its later evolution. Preliminary calculations have been carried out using the techniques developed by Schwarz for the simulation of superfluid turbulence in  $^4\text{He}$ . These methods give good numerical agreement with experimental data in  $^4\text{He}$  (Schwarz 1978, 1985, 1988) and have been used extensively by Schwarz and many others (Aarts and de Waele 1994; Nemirovskii and Fiszdon 1994; Samuels 1992; Barenghi et al. 1997; Tsubota and Yoneda 1995).

In such calculations vortices are generally considered to be 1-dimensional objects without internal structure. In  $^4\text{He}$  the diameter of the core is much smaller than other

characteristic lengths, foremost the average radius of curvature for the loops or the inter-vortex distance, and even  $\ln(\tilde{\xi}/\xi)$  can be treated as a large parameter. This is not the case in  $^3\text{He-B}$  due to the large coherence length, especially in the early stages of the evolution when the vortex density is largest. However, as mentioned in Sec. 2.3, the characteristic inter-vortex distance and the radius of curvature may still be several times larger than the coherence length and the diameter of the vortex core. For now, we shall continue considering the vortices as linear objects.

There are several forces acting on a vortex line in a superfluid (Donnelly 1991). The Magnus force appears in the presence of superflow,

$$\mathbf{f}_M = \rho_s \kappa \nu \mathbf{s}' \times (\mathbf{v}_L - \mathbf{v}_{sl}), \quad (33)$$

where  $\mathbf{s}$  is the radius vector of a point on the vortex line and the prime denotes the derivative with respect to the length of the line (ie.  $\mathbf{s}'$  is a unit vector tangent to the vortex line at  $\mathbf{s}$ ),  $\mathbf{v}_L = \dot{\mathbf{s}}$  is the local velocity of the vortex line, and  $\mathbf{v}_{sl}$  is the local superfluid velocity at this point. For singular vortices in  $^3\text{He-B}$  the number of circulation quanta is  $\nu = 1$ . The local superfluid velocity  $\mathbf{v}_{sl}$  is a sum of the superfluid velocity  $\mathbf{v}_s$  far from the network and the velocity induced by all the vortices in the tangle:

$$\mathbf{v}_{sl}(\mathbf{r}) = \mathbf{v}_s + \frac{\kappa}{4\pi} \int_{\text{loops}}^{\text{all}} \frac{(\mathbf{s} - \mathbf{r}) \times d\mathbf{s}}{|\mathbf{s} - \mathbf{r}|^3}. \quad (34)$$

The Iordanskii force arises from the Aharonov-Bohm scattering of quasiparticles from the velocity field of the vortex,

$$\mathbf{f}_{\text{Iordanskii}} = \rho_n \kappa \nu \mathbf{s}' \times (\mathbf{v}_L - \mathbf{v}_n), \quad (35)$$

where  $\mathbf{v}_n$  is the velocity of the normal component (ie. the heat bath of the fermionic quasiparticles). The Kopnin or spectral flow force has the same form, but originates from the spectral flow of the quasiparticle levels in the vortex core:

$$\mathbf{f}_{\text{sf}} = m_3 \mathcal{C}(T) \kappa \nu \mathbf{s}' \times (\mathbf{v}_L - \mathbf{v}_n), \quad (36)$$

where the temperature dependent parameter  $\mathcal{C}(T)$  determines the spectral flow in the core. All these three forces are of topological origin: they act in the transverse direction and are thus nondissipative. They are discussed in more details in Sec. 3.

In contrast, the nontopological friction force  $\mathbf{f}_{\text{fr}}$  acts in the longitudinal direction,

$$\mathbf{f}_{\text{fr}} = -d_{\parallel} \rho_s \kappa \nu \mathbf{s}' \times [\mathbf{s}' \times (\mathbf{v}_n - \mathbf{v}_L)]. \quad (37)$$

Here the factor  $\rho_s \kappa \nu$  is the same as in the Magnus force.

Neglecting the vortex mass, we may write the force balance equation for the vortex element:

$$\mathbf{f}_M + \mathbf{f}_{\text{Iordanskii}} + \mathbf{f}_{\text{sf}} + \mathbf{f}_{\text{fr}} = 0. \quad (38)$$

It is convenient to rewrite the balance of forces in the following form:

$$\mathbf{s}' \times [(\mathbf{v}_L - \mathbf{v}_{sl}) - \alpha'(\mathbf{v}_n - \mathbf{v}_{sl})] = \alpha \mathbf{s}' \times [\mathbf{s}' \times (\mathbf{v}_n - \mathbf{v}_{sl})], \quad (39)$$

where  $\alpha$  and  $\alpha'$  are the dimensionless mutual friction coefficients. The  $\alpha$  parameters are actually the experimentally determined mutual friction quantities (see eg. Bevan et al. 1997a). The inverse coefficients are the  $d$  parameters:

$$\alpha + i(1 - \alpha') = \frac{1}{d_{\parallel} - i(1 - d_{\perp})}, \quad (40)$$

where  $i = \sqrt{-1}$ . The transverse mutual friction parameter  $d_{\perp}$  is expressed in terms of three temperature dependent functions which determine the Magnus, Iordanskii and spectral-flow forces:

$$d_{\perp}(T) = (m_3 \mathcal{C}(T) - \rho_n(T)) / \rho_s(T). \quad (41)$$

Eq. (39) is complicated because of the term (34) which contains the integral over the vortex network. To solve Eq. (39), one may follow Schwarz and neglect the influence of all other vortex segments on  $\mathbf{v}_{sl}$  except the one containing the point of interest (the so called local self-induced approximation). In this case

$$\mathbf{v}_{sl} \approx \mathbf{v}_s + \beta \mathbf{s}' \times \mathbf{s}'', \quad \text{where } \beta = \frac{\kappa}{4\pi} \ln \frac{\xi}{\tilde{\xi}}. \quad (42)$$

The leading correction to this simplification comes from the nearest neglected vortex segments and can be estimated to be of order  $\tilde{\xi}/[b \ln(\tilde{\xi}/\xi)]$ , where  $b$  is the average inter-vortex distance. For a network in  $^3\text{He-B}$ ,  $\tilde{\xi} \sim b$  and  $\ln(\tilde{\xi}/\xi) \sim 1$  in the early stages of the evolution and thus at this point the approximation is rather crude. However, the main effect in the initial stages arises from the reconnection of vortex lines which happen to cross each other and this effect is taken into account below.

A second simplification close to  $T_c$  comes from  $\alpha' \ll \alpha$ . We may rewrite the equation of vortex motion in the form:

$$\mathbf{v}_L = \mathbf{v}_s + \beta \mathbf{s}' \times \mathbf{s}'' + \alpha \mathbf{s}' \times [(\mathbf{v}_n - \mathbf{v}_s) - \beta \mathbf{s}' \times \mathbf{s}'']. \quad (43)$$

In the rotating reference frame the normal component is at rest,  $\mathbf{v}_n = 0$ , and one has  $\mathbf{v}_s = -\mathbf{v}$ , where  $\mathbf{v} = \mathbf{v}_n - \mathbf{v}_s$  is the counterflow velocity. We shall be comparing to experimental results measured at  $T = 0.96 T_c$  and  $P = 18$  bar, where the most detailed data were collected. In these conditions  $\alpha \approx 10$  (Bevan et al. 1995) and in the rotating frame Eq. (43) can be simplified further to the form

$$\dot{\mathbf{s}} = \alpha \beta \mathbf{s}'' + \alpha \mathbf{s}' \times \mathbf{v}, \quad (44)$$

The first term on the right hand side of Eq. (44) causes a loop to shrink while the second represents growth or shrinking, depending upon the orientation of the loop with respect to the counterflow.

In the numerical calculation vortices are considered as lines in the same 3-dimensional lattice as before. The temporal and spatial coordinates are discrete and therefore the network evolves in discrete steps: During each step in time a vertex of a loop can jump to one of the adjacent vertices of the lattice. The probability of a jump in any direction is proportional to the component of  $\dot{\mathbf{s}}$  in Eq. (44) in this direction, so that the average velocity equals  $\dot{\mathbf{s}}$ . Other more elaborate representations of vortex loops, based on splines for instance, have been used to model the dynamics of smooth vortex lines in the continuous space. However, for the preliminary study of the network evolution the simplest lattice representation was used. The simple case of one circular loop in the counterflow, where the result is known analytically, can be checked separately and it is found to give correct results.

It is well known that the interactions between neighboring vortex segments in the tangle play an important role in the evolution of a dense network. These interactions lead to the reconnection of loops which cross each other. The reconnections are the main source for the rarefaction of the network at the initial stages of evolution, which process through formation and decay of small loops. The reconnection process has been studied numerically (Schwarz 1985; Koplik and Levine 1993) and was found to occur with a probability close to unity for vortex lines approaching each other. In the simulations the vertices are connected in such a way that closed loops are obtained after each time step during the evolution. If a cell is pierced by two vortices, the two segments coming in and the two segments going out are connected randomly. This corresponds to a reconnection probability of 0.5. It is reasonable to suppose that this convention leads to a slowing down in the evolution, in particular in the initial phase, but does not produce gross qualitative changes.

The vortex tangle is initially produced by the procedure described in Sec. 2.13.2, in a lattice  $40 \times 40 \times 40$ , and its evolution is followed until all vortices have disappeared or loops have expanded and formed circular planar rings far from their location of origin. These large rings are counted, since it is fair to assume that each one of them will produce a detectable rectilinear vortex line in the rotating container. The calculation is repeated for a large number of random initial distributions of the phase at any given value of  $v$ . The results are averaged to obtain the average number of vortices  $N_b$ , which are produced from one simulated bubble as a function of  $v$ , and are compared to experimental data in Fig. 23. It is also possible to study the validity of the scaling law (30)

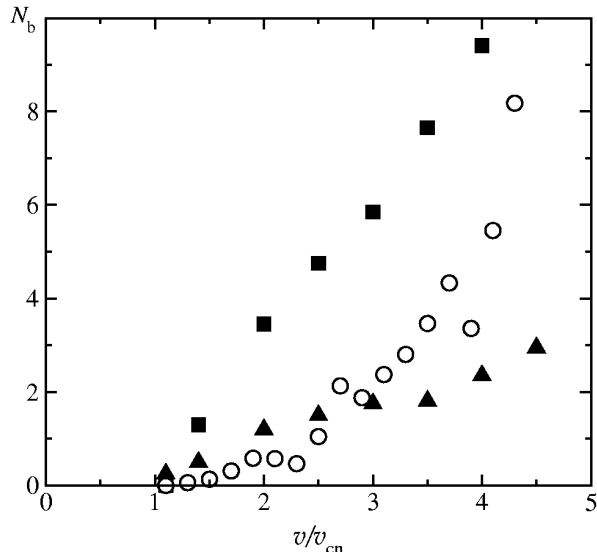


FIG. 23. The number of vortices  $N_b$  escaped from the bubble heated by one absorbed neutron as a function of  $v/v_{cn}$ : (■) simulation of the network evolution in the local self-induced approximation (Eq. (42)) and (▲) by including in addition approximately the polarization of the tangle by the superflow (Eq. (45)). Both calculations were performed on a  $40 \times 40 \times 40$  lattice, but the results remain unchanged if the lattice is reduced in size to  $20 \times 20 \times 20$ . The experimental data (○) represent measurements at  $P = 18$  bar and  $T = 0.96 T_c$  (Ruutu et al. 1996a).

at different stages of the evolution in the course of these simulations. In the absence of counterflow ( $v = 0$ ) it is found that the relation is valid for large loops,  $L > 4\tilde{\xi}$ , at least during much of the early evolution (in the late stages, when  $n$  approaches zero, the statistical noise exceeds  $n$ ).

Fig. 23 illustrates the simulation results. No vortices are obtained at low counterflow velocity  $v < v_{cn}$ , but when  $v > v_{cn}$ , their number  $N_b$  starts to increase rapidly with  $v$ . The value of the threshold velocity  $v_{cn}$  corresponds to the situation when the largest radius of curvature  $r_o(v_{cn})$  becomes equal to the diameter of the initial volume of the vortex network (ie. the diameter of the heated bubble). It then becomes possible for a loop to escape into the bulk superfluid if it consists of at least one arc with sufficiently large radius of curvature  $\geq r_o$ . The same calculations were also performed for a tangle with an initial volume of  $20 \times 20 \times 20$ , but no differences were found in the dependence  $N_b(v/v_{cn})$ . This is additional circumstantial evidence for the fact that the scaling relations approximately survive during the evolution of the network also in the counterflow until the moment of escape and that the network can be approximated as scale invariant.

The experimental data (denoted with (○) in Fig. 23) fit the universal dependence  $N_b(v/v_{cn}) = \tilde{\alpha}[(v/v_{cn})^3 - 1]$ , where  $\tilde{\alpha}$  equals  $\alpha$  in Eq. (8) divided by the neutron flux.

The numerical results (■) lie higher (note that no fitting parameters are involved) and do not display a cubic dependence in the experimental range  $1 < v/v_{cn} < 4$ . The differences could be explained by the approximations in the expression for  $\mathbf{v}_{sl}$ , which neglect significant contributions from the inter-vortex interactions. The polarization by the external counterflow causes the loops with unfavourable orientation to contract and loops with the proper winding direction and orientation to grow. However, as the polarization evolves, it also screens the vortex tangle from the external counterflow. To check whether the polarization has a significant effect on the results, the calculations were repeated by taking the screening approximately into account in the expression for  $\mathbf{v}_{sl}$ :

$$\mathbf{v}_{sl} = \mathbf{v}_s + \beta \mathbf{s}' \times \mathbf{s}'' + \frac{\kappa}{4\pi} \int_{\text{other loops}} \frac{1}{V} \int d\mathbf{r} \frac{(\mathbf{s} - \mathbf{r}) \times d\mathbf{s}}{|\mathbf{s} - \mathbf{r}|^3}. \quad (45)$$

Here the contribution from each loop to the superflow is averaged over the volume. The results (▲) show that this effect is significant and should be taken into account more accurately, to reproduce the network evolution correctly.

To summarize we note that the preliminary simulation work shows that it is possible to obtain numerical agreement between the KZ mechanism and the rotating experiments, if one assumes that the scaling relations of the initial vortex tangle are roughly obeyed also during its later evolution in the presence of the external superflow. This assumption should still be checked with sufficiently accurate simulation, with full account of the non-local inter-vortex interactions. Future simulation of transient networks should then answer the question how much information about the initial state of the vortex tangle can be retrieved from the rotating experiment, where only the final stationary state result is measured.

## 2.14. Superfluid transition as a moving phase front

In any real laboratory system a rapid phase transition becomes inhomogeneous: The transition will be driven by a strong gradient in one or several of the externally controlled variables. In the case of the superfluid transition in the aftermath of a neutron absorption event it is a steep and rapidly relaxing thermal gradient. In this situation even a second order transition becomes spatially inhomogeneous and is localized into a phase front. In the limit of very fast transitions the order-parameter relaxation slows down the propagation of the superfluid phase and the thermal front, where the temperature drops below  $T_c$ , may escape ahead. This means that the moving phase boundary breaks down into a leading thermal front and a trailing superfluid interface. The width of the region between these two zones is determined by

the relative velocities of thermal and superfluid relaxations. Thermal fluctuations in this region are amplified in the transition process and are carried over as order-parameter inhomogeneity into the new symmetry-broken phase. This is the central claim of the KZ model. Below we shall briefly discuss the influence of the thermal gradient on defect formation, as analyzed by Kibble and Volovik (1997) and Kopnin and Thuneberg (1999).

#### 2.14.1. Neutron absorption and heating

The decay products from the neutron absorption reaction generate ionization tracks which can be estimated from a standard calculation of stopping power (Meyer and Sloan 1997). This leads to a cigar-shaped volume of ionized particles, with the largest concentration at the end points of the two tracks. The probabilities and relaxation times of the different recombination channels for the ionized charge are not well known in liquid  $^3\text{He}$ . Also the thermalization of the reaction energy may not produce a heated region which preserves the shape of the original volume with the ionized charge.

Initially the recombination processes are expected to lead to particles with large kinetic energies in the eV range, which are well outside the thermal distribution and for which the recoil velocities become more and more randomly oriented. Energetic particles suffer collisions with their nearest neighbors and the mean free path increases only slowly for atoms participating in these collisions, until all particles are slowed down and become thermalized to the ambient conditions (Bunkov and Timofeevskaya 1998a,b). This means that the reaction energy remains initially localized. In the calorimetric experiments at the lowest temperatures (Bäuerle et al. 1996, 1998a) the thermal mean free path exceeds the container dimensions. Nevertheless, the energy is not immediately dispersed into the entire container volume, but remains centralized within a bubble of limited size during cooling through  $T_c$ , when the vortex network is formed. This is the conclusion to be drawn from the comparison between experiment and the KZ mechanism in Table I, where it is assumed that the thermal diffusion mean free path is the same as in the normal fluid at  $T_c$ .

In an inhomogeneous initial state with large thermal gradients the second order phase transition is turned into one where a normal-to-superfluid phase front with finite width sweeps through the heated bubble. If the velocity of the phase front,  $v_T \sim R_b/\tau_Q \sim 6$  m/s, is sufficiently high, comparable to a critical value  $v_{Tc} \sim v_F (\tau_0/\tau_Q)^{\frac{1}{4}}$ , then the KZ mechanism is again expected to dominate, similarly as in the homogeneous case (Kibble and Volovik 1997).

In contrast, if the majority of the kinetic energy is assumed to be thermalized by quasiparticles with en-

ergies comparable to the high-energy tail of the thermal Maxwellian velocity distribution, then the mean free paths are long, the volume heated above the ambient becomes large, and its temperature distribution may even become nonmonotonic like in a “Baked Alaska”, as has been described by Leggett (1992). The Baked Alaska scenario is also popular in high energy physics, where the formation of the false vacuum with a chiral condensate after a hadron-hadron collision is considered (Bjorken 1997; Amelino-Camelia et al. 1997). In both cases a rather thin shell of radiated high energy particles expands, with the speed of light in a relativistic system and with the Fermi velocity  $v_F$  in  $^3\text{He}$ , leaving behind a region at reduced temperature. Since this interior region is separated from the exterior vacuum by the hot shell, the cooldown into the broken symmetry state in the center is not biased by the external order parameter state. The Baked Alaska mechanism thus can solve the problem of the neutron-mediated formation of B phase from supercooled bulk A liquid (Leggett 1992), while in high energy physics it opens the possibility for the formation of a bubble of chiral condensate in a high energy collision (Bjorken 1997; Amelino-Camelia et al. 1997).

In such conditions, when the quasiparticle mean free path exceeds or is comparable to the dimensions of the heated bubble, temperature is not a useful quantity for the description of its cooling. Most of the analysis of the previous sections is applicable only if we assume that the reaction energy remains reasonably well localized while the hot bubble cools through  $T_c$ . In this case there is no Baked-Alaska effect: No hot shell will be formed which would separate the interior from the exterior region. In this situation the exterior region could be imagined to fix the phase in the cooling bubble, while the phase front is moving inward, suppressing the formation of new order-parameter states, which are different from that in the bulk superfluid outside, and in the same manner suppressing the formation of vortices. However, it appears that there also exists another alternative: The influence of the exterior region may not be decisive if the phase transition front moves sufficiently rapidly. Which of these mechanisms wins in a particular situation is still very much a subject of discussion.

For the interpretation of the measurements in neutron irradiation, a sophisticated understanding of the shape and size of the constant temperature contours within the heated bubble is not vitally necessary. In the final results the bubble size does not enter, since the data can be normalized in terms of the measured threshold velocity  $v_{cn}$ . Its measurement provides an estimate of the circumference of the bubble, since the largest possible vortex ring has to be comparable in size to the neutron bubble. The diameter of this ring is 1–2 orders of magnitude larger than the expected average inter-vortex distance  $\xi_v$  in the initial random network which is created by the KZ mech-

anism.

### 2.14.2. Thermal gradient and velocity of phase front

For a rough understanding of the superfluid transition in a temperature gradient let us consider the time dependent Ginzburg-Landau (TDGL) equation for a one-component order parameter  $\Psi = \Delta/\Delta_0$ :

$$\tau_0 \frac{\partial \Psi}{\partial t} = \left(1 - \frac{T(\mathbf{r}, t)}{T_c}\right) \Psi - \Psi |\Psi|^2 + \xi_0^2 \nabla^2 \Psi \quad , \quad (46)$$

where the notations for  $\tau_0 \propto 1/\Delta_0$  and  $\xi_0$  are the same as in Sec. 2.3. This equation is the so-called over-damped limit of the more general TDGL equation which has a time derivative of second order. The over-damped limit has been used in numerical simulations (Laguna and Zurek 1997; Antunes et al. 1999; Aranson et al. 1999) and analytical estimations (Dziarmaga 1998, 1999) of the density of topological defects in a homogeneous quench. An extension of the above equation to superconductivity was used by Ibaceta and Calzetta (1999) to study the formation of defects after a homogeneous quench in a 2-dimensional type II superconductor.

If the quench occurs homogeneously in the whole space  $\mathbf{r}$ , the temperature depends only on one parameter, the quench time  $\tau_Q$ :

$$T(t) = \left(1 - \frac{t}{\tau_Q}\right) T_c \quad . \quad (47)$$

In the presence of a temperature gradient, say, along  $x$ , a new parameter appears, which together with  $\tau_Q$  characterizes the evolution of the temperature:

$$T(x - v_T t) = \left(1 - \frac{t - x/v_T}{\tau_Q}\right) T_c \quad . \quad (48)$$

Here  $v_T$  is the velocity of the temperature front which is related to the temperature gradient (Kibble and Volovik 1997)

$$\nabla_x T = \frac{T_c}{v_T \tau_Q} \quad . \quad (49)$$

With this new parameter  $v_T$  we may classify transitions to belong to one of two limiting regimes: slow or fast propagation of the transition front. At slow velocities,  $v_T \rightarrow 0$ , the order parameter moves in step with the temperature front and

$$|\Psi(x, t)|^2 = \left(1 - \frac{T(x - v_T t)}{T_c}\right) \Theta(1 - T(x - v_T t)/T_c) \quad . \quad (50)$$

Here  $\Theta$  is the step function. In this case phase coherence is preserved behind the transition front and no defect formation is possible.

The opposite limit of large velocities,  $v_T \rightarrow \infty$ , is more interesting. Here the phase transition front lags behind the temperature front (Kopnin and Thuneberg 1999). In the space between these two boundaries the temperature is already below  $T_c$ , but the phase transition did not yet happen, and the order parameter has not yet formed,  $\Psi = 0$ . This situation is unstable towards the formation of blobs of the new phase with  $\Psi \neq 0$ . This occurs independently in different regions of space, leading to vortex formation via the KZ mechanism. At a given point  $\mathbf{r}$  the development of the instability can be found from the linearized TDGL equation, since during the initial growth of the order parameter  $\Psi$  from zero the cubic term can be neglected:

$$\tau_0 \frac{\partial \Psi}{\partial t} = \frac{t}{\tau_Q} \Psi \quad . \quad (51)$$

This gives an exponentially growing order parameter, which starts from some seed  $\Psi_{\text{fluc}}$ , caused by fluctuations:

$$\Psi(\mathbf{r}, t) = \Psi_{\text{fluc}}(\mathbf{r}) \exp \frac{t^2}{2\tau_Q \tau_0} \quad . \quad (52)$$

Because of exponential growth, even if the seed is small, the modulus of the order parameter reaches its equilibrium value  $|\Psi_{\text{eq}}| = \sqrt{1 - T/T_c}$  after the Zurek time  $t_{\text{Zurek}}$ :

$$t_{\text{Zurek}} = \sqrt{\tau_Q \tau_0} \quad . \quad (53)$$

This occurs independently in different regions of space and thus their order-parameter phases are not correlated. The spatial correlation is lost over distances exceeding  $\xi_v$  when the gradient term in Eq. (46) becomes comparable to the other terms at  $t = t_{\text{Zurek}}$ . Equating the gradient term  $\xi_0^2 \nabla^2 \Psi \sim (\xi_0^2/\xi_v^2) \Psi$  to, say, the term  $\tau_0 \partial \Psi / \partial t|_{t_{\text{Zurek}}} = \sqrt{\tau_0/\tau_Q} \Psi$ , one obtains the characteristic Zurek length which determines the initial length scale of defects,

$$\xi_v = \xi_0 (\tau_Q/\tau_0)^{1/4} \quad , \quad (54)$$

which is the same as in Eq. (3).

We can estimate the lower limit for the characteristic value of the fluctuations  $\Psi_{\text{fluc}} = \Delta_{\text{fluc}}/\Delta_0$ , which serve as a seed for vortex formation. If there are no other sources of fluctuations, caused by external noise for example, the initial seed is provided by thermal fluctuations of the order parameter in the volume  $\xi_v^3$ . The energy of such fluctuations is  $\xi_v^3 \Delta_{\text{fluc}}^2 N_F/E_F$ , where  $E_F \sim k_B T_F$  is the Fermi energy and  $N_F$  the fermionic density of states in normal Fermi liquid. Equating this energy to temperature  $T \approx T_c$  one obtains the magnitude of the thermal fluctuations

$$\frac{|\Psi_{\text{fluc}}|}{|\Psi_{\text{eq}}|} \sim \left(\frac{\tau_0}{\tau_Q}\right)^{1/8} \frac{T_c}{E_F} \quad . \quad (55)$$

The same small parameter  $k_B T_c / E_F \sim a / \xi_0 \sim 10^{-3} - 10^{-2}$  enters here, which is responsible for the extremely narrow temperature region of the critical fluctuations in  $^3\text{He}$  near  $T_c$ . But in our case it only slightly increases the Zurek time by the factor  $\sqrt{\ln[|\Psi_{\text{eq}}|/|\Psi_{\text{fluc}}|]}$  and thus does not influence vortex formation in a homogeneous quench or in an inhomogeneous quench at large velocities of the temperature front.

Clearly there must exist a characteristic velocity  $v_{T_c}$  of the propagating temperature front, which separates the fast and slow regimes, or correspondingly transitions with and without defect formation. The criterion for defect formation is that the Zurek time  $t_{\text{Zurek}} = \sqrt{\tau_Q \tau_0}$  should be shorter than the time  $t_{\text{sw}}$  in which the phase transition front sweeps through the space between the two boundaries. The latter time is  $t_{\text{sw}} = x_0 / v_T$ , where  $x_0$  is the lag – the distance between the temperature front  $T = T_c$  and the region where superfluid coherence starts (order parameter front). If  $t_{\text{Zurek}} < t_{\text{sw}}$ , instabilities have time to develop. If  $t_{\text{Zurek}} > t_{\text{sw}}$ , both fronts move coherently and the phase is continuous. Let us consider the latter case, with “laminar” motion, and find how the lag  $x_0$  depends on  $v_T$ . From the equation  $t_{\text{Zurek}} = x_0(v_{T_c})/v_{T_c}$  we find the criterion for the threshold where laminar motion becomes unstable and defect formation starts.

In steady laminar motion the order parameter depends on  $x - v_T t$ . Introducing a dimensionless variable  $z$  and a dimensionless parameter  $a$ ,

$$z = (x - v_T t)(v_T \tau_Q \xi_0^2)^{-1/3}, \quad a = \left(\frac{v_T \tau_0}{\xi_0}\right)^{4/3} \left(\frac{\tau_Q}{\tau_0}\right)^{1/3}, \quad (56)$$

the linearized TDGL equation becomes

$$\frac{d^2 \Psi}{dz^2} + a \frac{d\Psi}{dz} - z\Psi = 0, \quad (57)$$

or

$$\Psi(z) = \text{const} \cdot e^{-az/2} \chi(z), \quad \frac{d^2 \chi}{dz^2} - \left(z + \frac{a^2}{4}\right) \chi = 0. \quad (58)$$

This means that  $\Psi$  is an Airy function,  $\chi(z - z_0)$ , centered at  $z = z_0 = -a^2/4$  and attenuated by the exponential factor  $e^{-az/2}$ .

When  $a \gg 1$ , it follows from Eq. (58) that  $\Psi(z)$  quickly vanishes as  $z$  increases above  $-a^2/4$ . Thus there is a supercooled region  $-a^2/4 < z < 0$ , where  $T < T_c$ , but the order parameter is not yet formed: the solution is essentially  $\Psi = 0$ . The lag between the order parameter and temperature fronts is  $|z_0| = a^2/4$  or in conventional units

$$x_0 = \frac{1}{4} \frac{v_T^3 \tau_Q \tau_0^2}{\xi_0^2}. \quad (59)$$

Setting  $t_{\text{Zurek}} = x_0(v_{T_c})/v_{T_c}$  one can estimate the value for the velocity of the temperature front where laminar propagation becomes unstable:

$$v_{T_c} \sim \frac{\xi_0}{\tau_0} \left(\frac{\tau_0}{\tau_Q}\right)^{1/4}. \quad (60)$$

This result corresponds to  $a \sim 1$  and is in agreement with that obtained from scaling arguments by Kibble and Volovik (1997). Here an exact numerical value cannot be offered for the threshold where laminar motion ends, but this can in principle be done using the complete TDGL equation (Kopnin and Thuneberg 1999). For the neutron bubble we might take  $v_T \sim R_b/\tau_Q$ , which gives  $v_T \sim 10$  m/s. This value provides also an estimate for the limiting velocity  $v_{T_c}$ . These considerations suggest that the thermal gradient should be sufficiently steep in the neutron bubble such that defect formation is to be expected.

## 2.15. Quench of infinite vortex tangle

### 2.15.1. Vorticity on microscopic and macroscopic scales

Onsager (1949) was the first to interpret the  $\lambda$ -transition in liquid  $^4\text{He}$  from the superfluid to the normal state in terms of quantized vortices: When the concentration of the thermally activated quantized vortices reaches the point where they form a connected tangle throughout the liquid (and their line tension vanishes), the liquid goes normal (Fig. 24). This proliferation of vortices to an infinite network destroys superfluidity, since the phase slippage processes caused by the back reaction from the tangle to the superfluid current lead to the decay of this current.

In Ginzburg-Landau theory vortices are identified as lines of zeroes in the scalar complex order parameter  $\Psi = |\Psi|e^{i\Phi}$ , around which the phase winding number  $\nu$  is nonzero. Above the transition, in the symmetric phase, thermal fluctuations of the order parameter give rise to an infinite network of zeroes – to vortices which exist on the microscopic scale but are absent on the macroscopic scale (Kleinert 1989). This is another way of describing the fact that there is no long range order in the symmetric phase. The properties of such microscopic vortices – topologically nontrivial zeroes – have been followed across the thermodynamic phase transition in numerical investigations (Antunes and Bettencourt 1998; Antunes et al. 1998; Rajantie et al. 1998; Kajantie et al. 1998; Rajantie 1998). The renormalization group description of the phase transition, based on the Ginzburg-Landau free energy functional, also contains the microscopic quantized vortices, but in an implicit form of zeroes (see e.g. Guillou and Zinn-Justin 1980 and Albert 1982).

Some attempts have been made to reformulate the 3-dimensional phase transition in terms of this vortex picture in the renormalization group approach (Williams

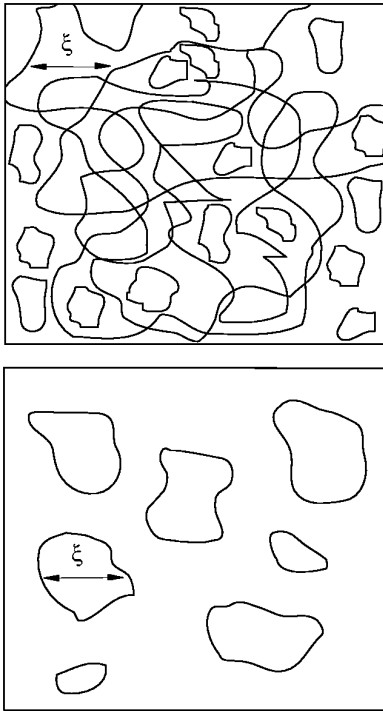


FIG. 24. Normal-to-superfluid transition, when described as a change-over from an infinite to a finite vortex network. (*Top*) The disordered phase ( $T > T_c$ ) is an infinite network of the defects in the ordered phase – the vacuum of tangled closed loops. The coherence length  $\xi$  is the mean distance between the elements in this network. (*Bottom*) In the ordered phase ( $T < T_c$ ) the defects also form closed loops, but the coherence length is now the upper limit in the distribution of loop sizes.

1993a,b, 1999; Chattopadhyay et al. 1993), in a manner similar to the 2-dimensional Berezinskii-Kosterlitz-Thouless transition (Nelson and Kosterlitz 1977), i.e. by avoiding consideration of the Ginzburg-Landau free energy functional altogether. It is possible, though it has not been proven, that the Ginzburg-Landau model and the vortex model belong to the same universality class and thus give the same critical exponents for the heat capacity and superfluid density. Both ground and space-based measurements of the critical exponents (Goldner and Ahlers 1992; Lipa et al. 1996) have generally been consistent with the renormalization-group estimations (Guillou and Zinn-Justin 1980; Albert 1982), although possibly disagreement between theory and recent zero-gravity experiments may have appeared (Lipa et al. 1998).

In an equilibrium phase transition the infinite network disappears below  $T_c$ , but in a non-equilibrium phase transition the tangle of microscopic vortices persists even into the ordered phase, due to critical slowing down. These vortices finally transform to conventional macroscopic vortices, when the latter become well defined. In

this language the Kibble-Zurek mechanism corresponds to a quench of the infinite vortex network across the non-equilibrium transition from the normal to the superfluid phase (Yates and Zurek 1998). What is important for us here, is the scaling law for the distribution of vortices. According to numerical simulations (Antunes and Bettencourt 1998; Antunes et al. 1998) and the phenomenological vortex model (Williams 1993a,b, 1999; Chattopadhyay et al. 1993) the scaling exponent  $\delta$ , which characterizes the distribution of vortex loops in Eq. 31), is close to the value  $\delta = 2/(d + 2) = 0.4$  obtained using the concept of Flory calculations for self-avoiding polymers. It is different from the value given by the Vachaspati-Vilenkin model for a Brownian-walk network. On the other hand, this model was applied to the Ginzburg region of critical fluctuations in  $^4\text{He}$ , which might not be valid for  $^3\text{He}$ .

### 2.15.2. Scaling in equilibrium phase transitions

Important differences exist between the phase transitions in the  $^4\text{He}$  and  $^3\text{He}$  liquids. These also are involved in a number of other phenomena. Let us therefore recall some of these differences. The temperature region of the critical fluctuations, where the simple Ginzburg-Landau theory does not work and one must introduce the thermal renormalization of the Ginzburg-Landau functional, can be derived from the following simplified considerations. Let us estimate the length  $L_T$  of the thermal vortex loop, i.e. a loop whose energy is comparable to temperature:

$$\rho_s(T) \frac{\kappa^2}{4\pi} L_T \ln \left( \frac{L_T}{\xi(T)} \right) = k_B T \approx k_B T_c. \quad (61)$$

In the broken symmetry phase far below  $T_c$ , this length is less than the coherence length  $\xi(T)$ , which means that there are no real vortices with the energy of order  $k_B T$ , and real vortices with higher energy are exponentially suppressed. When the temperature increases, one approaches the point at which the length  $L_T$  becomes comparable to the coherence length  $\xi$ . This is the Ginzburg temperature  $T_{Gi}$ , determined by the condition  $L_T(T = T_{Gi}) \sim \xi(T = T_{Gi})$ :

$$\rho_s(T_{Gi}) \xi(T_{Gi}) \sim \frac{k_B T_c}{\kappa^2}. \quad (62)$$

or

$$\left( 1 - \frac{T_{Gi}}{T_c} \right) \sim \left( \frac{k_B T_c}{\rho \xi_0 \kappa^2} \right)^2 \sim \left( \frac{T_c}{T_F} \right)^4. \quad (63)$$

Here as before  $T_F \sim \hbar^2/ma^2 \sim 1\text{K}$  is the degeneracy temperature of the quantum fluid, with  $a$  being the inter-atomic spacing. The region of critical fluctuations – the Ginzburg region  $T_{Gi} < T < T_c$  – is broad for

$^4\text{He}$ , where  $T_c \sim T_F$ , and extremely small for  $^3\text{He}$ , where  $T_c < 10^{-2} T_F$ .

In the region of Ginzburg fluctuations the scaling exponents for the thermodynamic quantities, such as  $\xi(T)$  and  $\rho_s(T)$ , are different from those in the Ginzburg-Landau region,  $T_c - T_{\text{Gi}} < T_c - T \ll T_c$ :

$$\frac{\xi(T)}{\xi_0} \sim \left(1 - \frac{T}{T_c}\right)^{-\frac{1}{2}}, \quad T_c - T_{\text{Gi}} < T_c - T \ll T_c, \quad (64)$$

$$\frac{\xi(T)}{\xi_0} \sim \left(1 - \frac{T_{\text{Gi}}}{T_c}\right)^{\nu - \frac{1}{2}} \left(1 - \frac{T}{T_c}\right)^{-\nu}, \quad T_{\text{Gi}} < T < T_c, \quad (65)$$

$$\frac{\rho_s(T)}{\rho} \sim \left(1 - \frac{T}{T_c}\right), \quad T_c - T_{\text{Gi}} < T_c - T \ll T_c, \quad (66)$$

$$\frac{\rho_s(T)}{\rho} \sim \left(1 - \frac{T_{\text{Gi}}}{T_c}\right)^{1-\zeta} \left(1 - \frac{T}{T_c}\right)^{\zeta}, \quad T_{\text{Gi}} < T < T_c. \quad (67)$$

There are two relations, the scaling hypotheses, which connect the critical exponents for  $\xi(T)$  and  $\rho_s(T)$  in the Ginzburg region, with the exponent of the heat capacity. In the Ginzburg region  $T_{\text{Gi}} < T < T_c$ , the coherence length is determined by thermal fluctuations, or which is the same thing, by thermal vortices. This gives for the relation between the coherence length  $\xi(T)$  and superfluid density  $\rho_s(T)$  in the Ginzburg region:

$$\rho_s(T)\xi(T) \sim \frac{k_B T_c}{\kappa^2} \sim \rho a \left(\frac{T_c}{T_F}\right), \quad T_{\text{Gi}} < T < T_c. \quad (68)$$

This equation gives the Josephson scaling hypothesis:  $\nu = \zeta$ .

Another relation between these exponents comes from a consideration of the free energy, which has the same scaling law as the kinetic energy of superflow:

$$F(T) \sim \left(1 - \frac{T}{T_c}\right)^{2-\alpha} \sim \rho_s v_s^2 \sim \frac{\rho_s(T)}{\xi^2(T)} \sim \frac{\rho}{\xi_0^2} \left(1 - \frac{T}{T_c}\right)^{\zeta+2\nu} \quad (69)$$

Here  $\alpha$  is the the critical exponent for the heat capacity in the critical region,  $C(T) = -T\partial_T^2 F \sim (1 - T/T_c)^{-\alpha}$ . Eqs. (68) and (69) give  $\nu = \zeta = (2 - \alpha)/3$ .

### 2.15.3. Non-equilibrium phase transitions

The formation of vortices during a rapid transition into the broken-symmetry phase is the subject of dynamic scaling and a poorly known area in the field of critical phenomena. Dynamic scaling is characterized by an additional set of critical exponents, which depend not only on the symmetry and topology of the order parameter, but also on the interaction of the order parameter with the different dynamic modes of the normal liquid. The

question first posed by Zurek was the following: What is the initial density  $\xi_v$  of macroscopic vortices at the moment when they become well defined? According to the general scaling hypothesis one has

$$\xi_v \sim \xi_0 (\omega \tau_0)^{-\lambda} \quad \text{and} \quad \omega = \frac{1}{\tau_Q}, \quad (70)$$

where  $\omega$  is the characteristic frequency of the dynamic process.

In the time-dependent Ginzburg-Landau model (Eq. (46)) and also in its extension based on the renormalization group approach, the exponent  $\lambda$  is determined by the static exponents and by the exponent for the relaxation time  $\tau = \tau_0(1 - T/T_c)^{-\mu}$ :

$$\lambda = \frac{\nu}{1 + \mu}. \quad (71)$$

This follows from the following consideration. When we approach the critical temperature from the normal phase, at some moment  $t_{\text{Zurek}}$  the relaxation time  $\tau(t)$  becomes comparable to the time  $t$  which is left until the transition takes place. At this moment

$$t_{\text{Zurek}} = \tau_0 \left(\frac{\tau_Q}{\tau_0}\right)^{\mu/(1+\mu)}, \quad (72)$$

the vortex network is frozen out. After the transition it becomes ‘‘unfrozen’’ when  $\tau(t)$  again becomes smaller than  $t$ , the time after passing the transition. The initial distance between the vortices is determined as the coherence length  $\xi = \xi_0(t/\tau_Q)^{-\nu}$  at  $t = t_{\text{Zurek}}$ , which gives Eq. (70) with  $\lambda$  as in Eq. (71). For the conventional time-dependent Ginzburg-Landau model in Eq. (46) one has  $\mu = 1$ ,  $\nu = 1/2$ , and thus  $\lambda = 1/4$ . In the Ginzburg regime, if one assumes that  $\mu$  remains the same, while  $\nu \approx 2/3$ , one obtains  $\lambda \approx 1/3$ .

In numerical simulation of a quench in the time-dependent Ginzburg-Landau model, the main problem becomes how to resolve between the microscopic vortices (ie. the zeroes in the order parameter) and real macroscopic vortices. This requires some coarse-graining procedure, which is not well established. Also speculations exist (Rivers 2000) that if the quench is limited to within the region of the Ginzburg fluctuations, then the network of microscopic vortices might effectively screen out the real macroscopic vortices, so that the density of the real vortices after the quench is essentially less than its Zurek estimate. This could explain the negative result of the recent pressure-quench experiments in liquid  $^4\text{He}$  (Dodd et al. 1998), where the final state after the decompression was well within the region of critical fluctuations.

### 2.16. Implications of the quench-cooled experiments

It is not entirely evident that a phenomenological model like the KZ mechanism, which is based on scal-

ing arguments, should work at all: It describes a time-dependent phase transition in terms of quantities characterizing the equilibrium properties of the system. Numerical calculations on simple quantum systems, where one studies the fluctuations in the amplitude of the system wave function while it is quench cooled below a second order phase transition, have provided much evidence for the KZ model and appear to agree with its qualitative features. Most experimental attempts of its verification suffer from serious deficiencies. Measurements on superfluid  $^3\text{He}$  are the first to test the KZ model more quantitatively. In this case the deviations from the ideal KZ setup include the presence of a strict boundary condition and a strong thermal gradient. At present time we can conclude that the experiments and the model are in reasonable harmony, assuming that open questions from Sec. 2.13 can be answered satisfactorily, as seems likely.

However, even good agreement leaves us with an interesting question: What is the microscopic basis for the applicability of the KZ mechanism to such experiments? A rapid quench through the superfluid transition is more amenable to microscopic analysis in the case of liquid  $^3\text{He}$  than in most other systems, since the freeze out of order-parameter domains can be demonstrated with physically acceptable calculations. The consequences from this are exciting and the prospects for a better understanding of non-equilibrium phase transitions look promising. Although detailed agreement has not yet been reached between experimental and theoretical work, nevertheless the effort by Aranson et al. (1999) illustrates that many aspects of the neutron absorption event in  $^3\text{He-B}$  can be treated in realistic ways.

Are there implications from such work to cosmological large-scale structure formation? The measurements described in this section illustrate that topological defects are expected to form in rapid second order phase transitions and support the suggestion that this could also be the case in the cosmological settings. It is still unclear what form these phase transitions take, what kind of defects can be formed, what traces such defects, which may have annihilated long ago, would leave behind, and whether defect formation alone or perhaps in the presence of other phenomena, like inflationary expansion, are needed to explain large-scale structure formation.

### 3. OTHER $^3\text{He}$ – QUANTUM FIELD THEORY ANALOGUES INVOLVING TOPOLOGICAL DEFECTS

At closer inspection, it has turned out that other connections can be worked out between the physics of the  $^3\text{He}$  superfluid phases and various ideas in relativistic quantum field theory. At best such analogue approaches have the benefit that the known and tested  $^3\text{He}$  features can perhaps open new ways of thought on how to solve

problems in quantum field theory, on which no direct experimental information yet exists. An example is the concept of the energetic physical vacuum in elementary particle physics – the modern ether. Bosonic and fermionic excitations in  $^3\text{He}$  are in many respects similar to the excitations of the physical vacuum. This similarity allows us to model, with concepts borrowed from  $^3\text{He}$  physics, the interactions of elementary particles with the evolving strings and domain walls, which are formed in a rapid phase transition. These processes become important after defect formation in the initial quench and give rise to the cosmological consequences which we are measuring today.

#### 3.1. Three topological forces acting on a vortex and their analogues

Here we consider several effects coming from these interactions, which result in the experimentally observed forces acting on the vortex moving in  $^3\text{He}$ . As we mentioned in Sec. 2.13.3, there are 3 different topological contributions to the force acting on the vortex. The more familiar Magnus force arises when the vortex moves with respect to the superfluid vacuum. For the relativistic cosmic string such force is absent since the corresponding superfluid density of the quantum physical vacuum is zero. However the analog of this force appears if the cosmic string moves in the uniform background charge density (Davis and Shellard 1989; Lee 1994). The other two forces of topological origin — the Iordanskii force and spectral flow force — also have analogues for the cosmic strings (Volovik and Vachaspati 1996; Volovik 1998; Sonin 1997; Wexler 1997; Shelankov 1998a,b), which we discuss here.

First we start with the Iordanskii force (Iordanskii 1964, 1965; Sonin 1975), which arises when the vortex moves with respect to the heat bath represented by the normal component of the liquid, which consists of the quasiparticle excitations. The latter corresponds to the matter in particle physics. The interaction of quasiparticles with the velocity field of the vortex resembles the interaction of the matter with the gravitational field induced by such cosmic string, which has an angular momentum, – the so-called spinning cosmic string (Mazur 1986). The spinning string induces the peculiar space-time metric, which leads to the difference of times needed for any particle to orbit around the string with the same speed, but in opposite directions (Harari and Polychronakos 1988). This gives rise to the quantum gravitational Aharonov-Bohm effect (Mazur 1986, 1987, 1996). In this section we discuss how the same effect leads to the asymmetry in the scattering of particles on the spinning string and finally to the Iordanskii lifting force acting on the spinning string or on the moving vortex in superfluid.

The other force, arising when the vortex moves with respect to the heat bath, is the direct consequence of the chiral anomaly effect, which violates the conservation of the fermionic charge. The anomalous generation by the moving vortex of such fermionic charge as momentum (called “momentogenesis”) leads to the net force acting on the vortex, which was experimentally confirmed in  $^3\text{He}$  (Bevan et al. 1997a). This phenomenon is based on the same physics as the anomalous generation of matter in particle physics and bears directly on the cosmological problem of the baryonic asymmetry of our present Universe: why the Universe contains much more matter than antimatter (“baryogenesis”).

The experimental observation of the opposite effect to momentogenesis has been reported by Krusius et al. (1998): the conversion of quasiparticle momentum into a non-trivial order parameter configuration or “texture”. The corresponding process in a cosmological setting would be the creation of a primordial magnetic field due to changes in the matter content. Processes in which magnetic fields are generated are very relevant to cosmology as magnetic fields are ubiquitous now in the Universe. The Milky Way, other galaxies, and clusters of galaxies are observed to have a magnetic field whose generation is still not understood. One possible mechanism is that a seed field was amplified by the complex motions associated with galaxies and clusters of galaxies. The seed field itself is usually assumed to be of cosmological origin.

It has been noted that the two genesis problems in cosmology – baryo- and magnetogenesis – may be related to each other (Roberge 1989; Vachaspati and Field 1994, 1995; Vachaspati 1994). More recently, a stronger possible connection has been detailed (Joyce and Shaposhnikov 1997; Giovannini and Shaposhnikov 1997). In the same way they are related in  $^3\text{He}$ , where the texture is the analog of magnetic field while the normal component of the liquid represents the matter: the moving vortex texture leads to the anomalous production of quasiparticles, while an excess of the quasiparticle momentum – the net quasiparticle current of the normal component – leads to the formation of textures. This mapping of cosmology to condensed matter is not simply a picture: the corresponding effects in the two systems are described by the same equations in the low-energy regime, by quantum field theory and the axial anomaly.

## 3.2. Iordanskii force

### 3.2.1. Superfluid vortex vs spinning cosmic string

To clarify the analogy between the Iordanskii force and Aharonov-Bohm effect, let us consider the simplest case of phonons propagating in the velocity field of the quantized vortex in the Bose superfluid  $^4\text{He}$ . According to

the Landau theory of superfluidity, the energy of quasiparticle moving in the superfluid velocity field  $\mathbf{v}_s(\mathbf{r})$  is Doppler shifted:  $E(\mathbf{p}) = \epsilon(\mathbf{p}) + \mathbf{p} \cdot \mathbf{v}_s(\mathbf{r})$ . In the case of the phonons with the spectrum  $\epsilon(\mathbf{p}) = cp$ , where  $c$  is the sound velocity, the energy-momentum relation is thus

$$(E - \mathbf{p} \cdot \mathbf{v}_s(\mathbf{r}))^2 = c^2 p^2. \quad (73)$$

The Eq. (73) can be written in the general Lorentzian form with  $p_\mu = (-E, \mathbf{p})$ :

$$g^{\mu\nu} p_\mu p_\nu = 0 \quad (74)$$

where the metric is

$$g^{00} = 1, \quad g^{0i} = -v_s^i, \quad g^{ik} = -c^2 \delta^{ik} + v_s^i v_s^k. \quad (75)$$

We use the convention to denote indices in the 0–3 range by Greek letters and indices in the 1–3 range by Latin letters. Thus the dynamics of phonons in the presence of the velocity field is the same as the dynamics of photons in the gravity field (Unruh 1976): both are described by the light-cone equation  $ds = 0$ . The interval  $ds$  for phonons is given by the inverse metric  $g_{\mu\nu}$  which determines the geometry of the effective space:

$$ds^2 = g_{\mu\nu} dx^\mu dx^\nu, \quad (76)$$

where  $x = (t, \mathbf{r})$  are physical (Galilean) coordinates in the laboratory frame.

The similar relativistic equation occurs for the fermionic quasiparticles in the superfluid  $^3\text{He-A}$  in the linear approximation close to the gap nodes (see Sec. 4.2.2). In general, i.e. far from the gap nodes, the spectrum of quasiparticle in  $^3\text{He-A}$  is not relativistic:

$$\epsilon^2(\mathbf{p}) = v_F^2 (p - p_F)^2 + \frac{\Delta_A^2}{p_F^2} (\hat{\mathbf{l}} \times \mathbf{p})^2. \quad (77)$$

Here  $v_F(p - p_F)$  is the quasiparticle energy in the normal Fermi liquid above transition, with  $p_F$  the Fermi momentum and  $v_F = p_F/m^*$ ;  $m^*$  is the effective mass, which is of order the mass  $m_3$  of the  $^3\text{He}$  atom;  $\Delta_A$  is the so-called gap amplitude and the unit vector  $\hat{\mathbf{l}}$  shows direction to the gap nodes.

The energy in Eq. (77) is zero at two points  $\mathbf{p} = e\mathbf{A}$  with  $\mathbf{A} = p_F \hat{\mathbf{l}}$  and  $e = \pm 1$ . Close to the two zeroes of the energy spectrum one can expand equation  $(E - \mathbf{p} \cdot \mathbf{v}_s(\mathbf{r}))^2 = \epsilon^2(\mathbf{p})$  in  $\mathbf{p} - e\mathbf{A}$  and bring it to the form similar to the propagation equation for a massless relativistic particle in a curved spacetime in the presence of an electromagnetic vector potential:

$$g^{\mu\nu} (p_\mu - eA_\mu)(p_\nu - eA_\nu) = 0. \quad (78)$$

Here  $A_0 = p_F(\hat{\mathbf{l}} \cdot \mathbf{v}_s)$  and the metric is anisotropic with the anisotropy axis along the  $\hat{\mathbf{l}}$ -vector:

$$\begin{aligned}
g^{00} &= 1, & g^{0i} &= -v_s^i, \\
g^{ik} &= -c_\perp^2 (\delta^{ik} - \hat{l}^i \hat{l}^k) - c_\parallel^2 \hat{l}^i \hat{l}^k + v_s^i v_s^k, \\
c_\parallel &= v_F, & c_\perp &= \Delta_A / v_F.
\end{aligned} \tag{79}$$

Here the quantities  $c_\parallel$  and  $c_\perp$  play the part of speeds of light propagating along  $\hat{\mathbf{l}}$  and in transverse directions correspondingly.

For simplicity, let us turn back to the case of phonons and vortices in  $^4\text{He}$  which is described by Eqs. (74), (75). If velocity field is induced by one vortex with  $\nu$  quanta of circulation,  $\mathbf{v}_s = \nu \kappa \hat{\phi} / 2\pi r$ , then the interval (76) in the effective space, where the phonon is propagating along geodesic curves, becomes:

$$\begin{aligned}
ds^2 &= \left(1 - \frac{v_s^2}{c^2}\right) \left(dt + \frac{\nu \kappa d\phi}{2\pi(c^2 - v_s^2)}\right)^2 \\
&\quad - \frac{dr^2}{c^2} - \frac{dz^2}{c^2} - \frac{r^2 d\phi^2}{c^2 - v_s^2}. \tag{80}
\end{aligned}$$

The origin of the Iordanskii force lies in the scattering of quasiparticles for small angles, so large distances from the vortex core are important. Far from the vortex  $v_s^2/c^2$  is small and can be neglected, and one has

$$ds^2 = \left(dt + \frac{d\phi}{\omega}\right)^2 - \frac{1}{c^2}(dz^2 + dr^2 + r^2 d\phi^2), \quad \omega = \frac{2\pi c^2}{\nu \kappa} \tag{81}$$

The connection between the time and the azimuthal angle  $\phi$  in the interval suggests that there is a characteristic angular velocity  $\omega$ . The similar metric with rotation was obtained for the so-called spinning cosmic string in 3 + 1 space-time, which has the rotational angular momentum  $J$  concentrated in the string core, and for the spinning particle in the 2+1 gravity (Mazur 1986, 1996; Staruszkiewicz 1963; Deser et al. 1984):

$$ds^2 = \left(dt + \frac{d\phi}{\omega}\right)^2 - \frac{1}{c^2}(dz^2 + dr^2 + r^2 d\phi^2), \quad \omega = \frac{1}{4JG} \tag{82}$$

where  $G$  is the gravitational constant. This gives the following correspondence between the circulation  $\nu \kappa$  around the vortex and the angular momentum  $J$  of the spinning string

$$\kappa \nu = 8\pi JG. \tag{83}$$

Though we consider the analogy between the spinning string and vortices in superfluid  $^4\text{He}$ , there is a general statement that vortices in any superfluids have the properties of the spinning cosmic strings (Davis and Shellard 1989). In particular, the spinning string generates the density of the angular momentum in the vacuum outside the string (Jensen and Kuvcera 1993). The density of

the angular momentum in the superfluid vacuum outside the vortex is also nonzero and equals at  $T = 0$

$$\mathbf{r} \times \rho \mathbf{v}_s = \hbar \nu n_B \hat{\mathbf{z}}, \tag{84}$$

where  $n_B$  is the density of elementary bosons in superfluid vacuum: the density  $\rho/m_A$  of  $^4\text{He}$  atoms in superfluid  $^4\text{He}$  or the density  $\rho/2m_3$  of Cooper pairs in superfluid  $^3\text{He}$ .

### 3.2.2. Gravitational Aharonov-Bohm effect

The effect peculiar for the spinning string, which can be modeled in condensed matter, is the gravitational Aharonov-Bohm topological effect (Mazur 1986). On the classical level the propagation of the particles is described by the relativistic equation  $ds^2 = 0$ . Outside the string the space metric, which enters the interval  $ds$ , is flat, Eq. (82). But there is the difference in the travel time for the particles propagating around the spinning string along the closed path in the opposite directions. As can be seen from (82) this time difference is (Harari and Polychronakos 1988)

$$2\tau = \frac{4\pi}{\omega}. \tag{85}$$

For the vortex at large distances from the core the same equation approximately valid due to equivalence of metrics Eqs. (81) and (82). This asymmetry between the particles orbiting in different directions around vortex implies that in addition to the symmetric part of the cross section:

$$\sigma_\parallel = \int_0^{2\pi} d\theta (1 - \cos \theta) |a(\theta)|^2, \tag{86}$$

where  $a(\theta)$  is a scattering amplitude, there should be an asymmetric part of the scattering cross section:

$$\sigma_\perp = \int_0^{2\pi} d\theta \sin \theta |a(\theta)|^2. \tag{87}$$

The latter is the origin of the Iordanskii force acting on the vortex in the presence of the net momentum of the quasiparticles. Another consequence of the Eqs. (81), (82) is displayed on the quantum level: the connection between the time variable  $t$  and the angle variable  $\phi$  in the Eqs. (81), (82) implies that the scattering cross sections of phonons (photons) on the vortex (string) should be the periodic functions of the energy with the period equal to  $\hbar\omega$ .

Calculations which allow to find both symmetric and asymmetric contributions to the scattering of the quasiparticles on the velocity field of the vortex have been done by Sonin (1997) for phonons and rotons in  $^4\text{He}$  and

by Cleary (1968) for the Bogoliubov-Nambu quasiparticles in conventional superconductors. In the case of phonons the propagation is described by the Lorentzian equation for the scalar field  $\Phi$ ,  $g^{\mu\nu}\partial_\mu\partial_\nu\Phi = 0$  with  $g^{\mu\nu}$  from Eq. (75). We are interested in large distances from the vortex core, so the quadratic terms  $\mathbf{v}_s^2/c^2$  can be neglected and this equation can be rewritten as (Sonin 1997)

$$E^2\Phi - c^2\left(-i\nabla + \frac{E}{c}\mathbf{v}_s(\mathbf{r})\right)^2\Phi = 0. \quad (88)$$

This equation maps the problem under discussion to the Aharonov-Bohm (AB) problem for the magnetic flux tube (Aharonov and Bohm 1959) with the effective vector potential  $\mathbf{A} = \mathbf{v}_s$ , where the electric charge  $e$  is substituted by the mass  $E/c^2$  of the particle (Mazur 1987; Jensen and Kuvcera 1993; Gal'tsov and Letelier 1993). Actually  $\mathbf{v}_s$  plays the part of the vector potential of the so called gravimagnetic field (see Sec. 4.2.7). Because of the mapping between the electric charge and the mass of the particle, one obtains the AB expression (Aharonov and Bohm 1959) for the symmetric differential cross section

$$\frac{d\sigma_{\parallel}}{d\theta} = \frac{\hbar c}{2\pi E \sin^2(\theta/2)} \sin^2 \frac{\pi E}{\hbar\omega}. \quad (89)$$

This expression was obtained for the scattering of particles with energy  $E$  in the background of spinning string with zero mass (Mazur 1987, 1996) and represented the gravitational Aharonov-Bohm effect. Note the singularity at  $\theta \rightarrow 0$ .

Returning back to vortices one finds that the analogue with the spinning string is not exact. In more accurate calculations one should take into account that as distinct from the charged particles in the AB effect, the current in the case of phonons is not gauge invariant. As a result the scattering of the phonon with momentum  $p$  and with the energy  $E$  by the vortex is somewhat different (Sonin 1997):

$$\frac{d\sigma_{\parallel}}{d\theta} = \frac{\hbar c}{2\pi E} \cot^2 \frac{\theta}{2} \sin^2 \frac{\pi E}{\hbar\omega}. \quad (90)$$

The algebraic difference between the AB result Eq. (89) and Eq. (90) is  $(\hbar c/2\pi E) \sin^2(\pi E/\omega)$ , which is independent of the scattering angle  $\theta$  and thus is not important for the singularity at small scattering angles, which is present in (90) as well. For small  $E$  the result in Eq. (90) was obtained by Fetter (1964). The generalization of the Fetter result for the quasiparticles with arbitrary spectrum  $\epsilon(\mathbf{p})$  (rotons in  $^4\text{He}$  and the Bogoliubov-Nambu fermions in superconductors) was recently suggested by Demircan et al. (1995): In our notations it is  $(\nu\kappa^2 p/8\pi v_G^2) \cot^2(\theta/2)$ , where  $v_G = d\epsilon/dp$  is the group velocity of quasiparticle.

### 3.2.3. Asymmetric cross section of scattering on a vortex

The Lorentz force, which acts on the flux tube in the presence of electric current, has its counterpart – the Iordanskii force, which acts on the vortex in the presence of the mass current carried by the normal component. The Lorentz-type Iordanskii force comes from the asymmetric contribution to the cross section (Sonin 1997; Shelankov 1998a,b), which has the same origin as singularity at the small angles in the symmetric cross section and leads to the non-zero transverse cross section.

For the phonons in the  $^4\text{He}$  with the spectrum  $E(\mathbf{p}) = cp$  the transverse cross section is (Sonin 1997)

$$\sigma_{\perp} = \frac{\hbar}{p} \sin \frac{2\pi E}{\hbar\omega} \quad (91)$$

At low  $E \ll \hbar\omega$  the result becomes classical:  $\sigma_{\perp} = 2\pi c/\omega$  does not contain the Planck constant  $\hbar$ . This means that in the low energy limit the asymmetric cross section can be obtained from the classical theory of scattering. In this case it can be generalized for arbitrary spectrum  $E(\mathbf{p})$  of scattering particles (Sonin 1997). Let us consider the particle with the spectrum  $E(\mathbf{p})$  moving in the background of the velocity field  $\mathbf{v}_s(\mathbf{r})$  around the vortex. The velocity field modifies the particle energy due to the Doppler shift,  $E(\mathbf{p}, \mathbf{r}) = E(\mathbf{p}) + \mathbf{p} \cdot \mathbf{v}_s(\mathbf{r})$ . Far from the vortex, where the circulating velocity is small, the trajectory of the quasiparticle is almost the straight line parallel, say, to the axis  $y$ , with the distance from the vortex line being the impact parameter  $x$ . It moves along this line with the almost constant momentum  $p_y \approx p$  and almost constant group velocity  $dy/dt = v_G = d\epsilon/dp$ . The change in the transverse momentum during this motion is determined by the Hamiltonian equation  $dp_x/dt = -\partial E/\partial x = -p_y \partial v_{sy}/\partial x$ , or  $dp_x/dy = -(p/v_G) \partial v_{sy}/\partial x$ . The transverse cross section is obtained by integration of  $\Delta p_x/p$  over the impact parameter  $x$ :

$$\sigma_{\perp} = \int_{-\infty}^{+\infty} \frac{dx}{v_G} \int_{-\infty}^{+\infty} dy \frac{\partial v_{sy}}{\partial x} = \frac{\nu\kappa}{v_G}. \quad (92)$$

This result is a pure classical: the Planck constant  $\hbar$  drops out (it enters only the circulating quantum which characterizes the vortex).

### 3.2.4. Iordanskii force: vortex and spinning string

The asymmetric part of scattering, which describes the momentum transfer in the transverse direction, after integration over the distribution of excitations gives rise to the transverse force acting on the vortex if the vortex moves with respect to the normal component. This is the Iordanskii force:

$$\begin{aligned} \mathbf{f}_{\text{Iordanskii}} &= \int \frac{d^3 p}{(2\pi)^3} \sigma_{\perp}(p) v_G n(\mathbf{p}) \mathbf{p} \times \hat{\mathbf{z}} = \\ &= -\nu \kappa \hat{\mathbf{z}} \times \int \frac{d^3 p}{(2\pi)^3} n(\mathbf{p}) \mathbf{p} = \nu \kappa \mathbf{P}_n \times \hat{\mathbf{z}} \end{aligned} \quad (93)$$

It is proportional to the density of mass current  $\mathbf{P}_n$  carried by excitations (matter). Of the vortex parameters it depends only on the circulation  $\nu \kappa$ . This confirms the topological origin of this force. In the case of the equilibrium distribution of quasiparticles one has  $\mathbf{P}_n = \rho_n \mathbf{v}_n$ , where  $\rho_n$  and  $\mathbf{v}_n$  are the density and velocity of the normal component of the liquid. So one obtains the Eq. (35). To avoid the conventional Magnus force in this derivation, we assumed that the asymptotic velocity of the superfluid component of the liquid is zero in the vortex frame.

The Eq. (93) was obtained using the asymptotic behavior of the flow field  $\mathbf{v}_s$ , which induces the same effective metric (81) as the metric around the spinning string (82). So one can apply this result directly to the spinning string. The asymmetric cross-section of the scattering of relativistic particles on the spinning string is given by Eq. (91). This means that in the presence of the momentum of matter the spinning cosmic string experiences the kind of the lifting force, which corresponds to the Iordanskii force in superfluids. This force can be obtained by relativistic generalization of the Eq. (93). The momentum density  $\mathbf{P}_n$  of quasiparticles should be substituted by the component  $T_0^i$  of the energy-momentum tensor. As a result, for 2+1 space-time and for small energy  $E$ , which corresponds to the low temperature  $T$  of the matter, the Iordanskii force on spinning string moving with respect to the matter is

$$f_{\text{Iordanskii}}^{\alpha} = 8\pi J G \varepsilon^{\alpha\beta\gamma} u_{\beta} u_{\mu} T_{\gamma}^{\mu}. \quad (94)$$

Here  $u_{\alpha}$  is the 3-velocity of the string and  $T_{\gamma}^{\mu}$  is the asymptotic value of the energy-momentum tensor of the matter at the spot of the string. Using the Einstein equations one can rewrite this as

$$f_{\text{Iordanskii}}^{\alpha} = J \varepsilon^{\alpha\beta\gamma} u_{\beta} u_{\mu} R_{\gamma}^{\mu}, \quad (95)$$

where  $R_{\gamma}^{\mu}$  is the Riemannian curvature at the position of the string. This corresponds to the force acting on particle with the spin  $J$  from the gravitational field due to interaction of the spin with the Riemann tensor (Thorne and Hartle 1985; Mino et al. 1997).

Note that previously we have shown how ideas first developed in cosmological context (such as nucleation of bubbles of different broken symmetry phases during rapid transition) could be applied to the superfluid helium. Here we have the opposite case: when the ideas originated from helium physics have application in the other systems described by the quantum field theory.

Iordanskii force has been experimentally identified in the rotating superfluid  $^3\text{He-B}$  (Bevan et al. 1997b). In

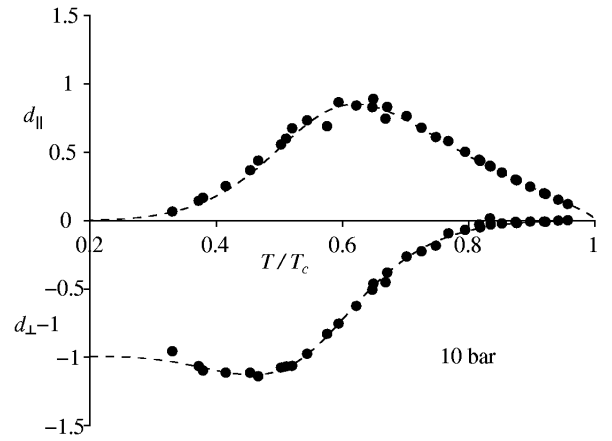


FIG. 25.  $d_{\parallel, \perp}$  as a function of temperature in  $^3\text{He-B}$  at 10 bar. Negative sign of  $d_{\perp}$  at  $T/T_c \approx 0.4-0.5$  constitutes experimental verification for the existence of Iordanskii force. Lines are fits to the experimental data. From Bevan et al. 1997b

Eq. (41) which describes temperature dependence of the friction coefficient  $d_{\perp}$  the term  $m_3 \mathcal{C}(T)$  is due to spectral flow force which is discussed in Sec. 3.3.3 and equals to zero at low temperatures. So at low temperatures  $d_{\perp} \approx -\rho_n/\rho$  (Kopnin et al. 1995), where  $\rho$  is the total density of the liquid. Negative value of  $d_{\perp}$  is solely due to the existence of the Iordanskii force. This is in accordance with the experimental data, which show that  $d_{\perp}$  does have negative value at low  $T$ , see Fig. 25. At higher  $T$  the spectral flow force becomes dominating leading to the sign reversal of  $d_{\perp}$ . Due to analogy between string and vortices outlined in this section this presents experimental verification of the analog of the gravitational Aharonov-Bohm effect on spinning cosmic string.

### 3.3. Spectral flow force and chiral anomaly

#### 3.3.1. Chiral anomaly

In the standard model of electroweak interaction there are certain quantities, like the baryon number  $Q_B$ , which are classically conserved but can be violated by quantum mechanical effects known generically as “chiral anomalies”. (Each of the quarks is assigned  $Q_B = 1/3$  while the leptons (neutrino and electron) have  $Q_B = 0$ .) The process leading to particle creation is called “spectral flow”, and can be pictured as a process in which fermions flow under an external perturbation from negative energy levels towards positive energy levels. Some fermions therefore cross zero energy and move from the Dirac sea into the observable positive energy world.

The origin for the axial anomaly can be seen from the behavior of the chiral particle in a constant magnetic field,  $\mathbf{A} = (1/2)\mathbf{B} \times \mathbf{r}$ . Chiral particle we call a particle

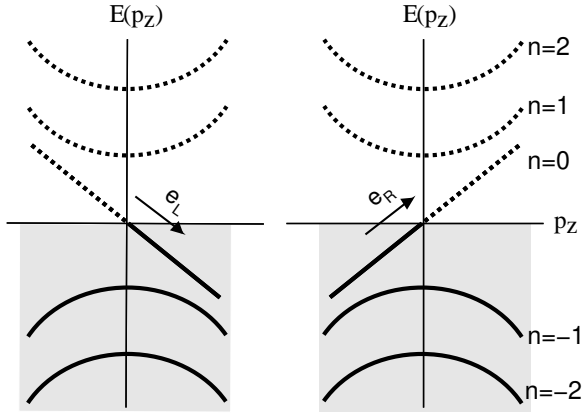


FIG. 26. The energy spectrum of a chiral particle in constant magnetic fields along  $\hat{z}$  (Landau levels). Plots on the left and the right show spectra for left and right particle respectively.

without mass but with spin  $\vec{\sigma}$  [ $=1/2$ ]. Such particle could be classified to right and left according to whether its spin is parallel or antiparallel to its momentum. The Hamiltonians for the right particle with the electric charge  $e_R$  and for the left particle with the electric charge  $e_L$  are

$$\mathcal{H} = c\vec{\sigma} \cdot (\mathbf{p} - e_R\mathbf{A}), \quad \mathcal{H} = -c\vec{\sigma} \cdot (\mathbf{p} - e_L\mathbf{A}). \quad (96)$$

As usual, motion of the particles in the plane perpendicular to  $\mathbf{B} \parallel \hat{z}$  is quantized into the Landau levels and the free motion is thus effectively reduced to one-dimensional motion along  $\mathbf{B}$  with momentum  $p_z$ . Fig. 26 shows the energy spectrum; the thick lines show the occupied negative-energy states. The peculiar feature of the spectrum is that because of the chirality of the particles the lowest ( $n = 0$ ) Landau level is asymmetric. It crosses zero only in one direction:  $E = cp_z$  for the right particle and  $E = -cp_z$  for the left one. If we now apply an electric field  $\mathbf{E}$  along  $z$ , particles are pushed from negative to positive energy levels according to the equation of motion  $\dot{p}_z = e_R E_z$  ( $\dot{p}_z = e_L E_z$ ) and the whole Dirac sea moves up (down) creating particles and electric charge from the vacuum. This motion of particles along the “anomalous” branch of the spectrum is called *spectral flow*. The rate of particle production is proportional to the density of states at the Landau level, which is

$$N_R(0) = \frac{|e_R \mathbf{B}|}{4\pi^2}, \quad N_L(0) = \frac{|e_L \mathbf{B}|}{4\pi^2} \quad (97)$$

The rate of production of particle number  $n = n_R + n_L$  and of charge  $Q = n_R e_R + n_L e_L$  from the vacuum is

$$\dot{n} = \frac{1}{4\pi^2} (e_R^2 - e_L^2) \mathbf{E} \cdot \mathbf{B}, \quad \dot{Q} = \frac{1}{4\pi^2} (e_R^3 - e_L^3) \mathbf{E} \cdot \mathbf{B}. \quad (98)$$

This is an anomaly equation for the production of particles from vacuum of the type found by Adler (1969) and

by Bell and Jackiw (1969) in the context of neutral pion decay. We see that for particle or charge creation without creation of corresponding antiparticles it is necessary to have an asymmetric branch of the dispersion relation  $E(p)$  which crosses the axis from negative to positive energy. Additionally, the symmetry between the left and right particles has to be violated:  $e_R \neq e_L$  for the charge creation and  $e_R^2 \neq e_L^2$  for the particle creation.

In the electroweak model there are two gauge fields whose “electric” and “magnetic” fields may become a source for baryonproduction: The hypercharge field  $U(1)$  and the weak field  $SU(2)$ . Anomalous zero mode branches exist in the core of a  $Z$ -string, where quarks, electrons and neutrinos are all chiral particles with known hypercharge and weak charges. If we consider a process in which one electron, two  $u$ -quarks and one  $d$ -quark are created, then lepton and baryon numbers are changed by unity while electric charge is conserved (Bevan et al. 1997a). If we sum appropriate charges for all particles according to Eq. (98) the rate of this process is

$$\dot{n}_{\text{bar}} = \dot{n}_{\text{lept}} = \frac{N_F}{8\pi^2} (-\mathbf{B}_W^a \cdot \mathbf{E}_{aW} + \mathbf{B}_Y \cdot \mathbf{E}_Y) \quad (99)$$

where  $N_F = 3$  is the number of families (generations) of fermions,  $\mathbf{B}_W^a$  and  $\mathbf{E}_{aW}$  are the colored  $SU(2)$  magnetic and electric fields, while  $\mathbf{B}_Y$  and  $\mathbf{E}_Y$  are the magnetic and electric fields of the  $U(1)$  hypercharge. While a color and hypercharge magnetic flux is always present in the  $Z$ -string core, a color and hypercharge electric field can also be present along the string if the string is moving across a background electromagnetic field (Witten 1985) or in certain other processes such as the decoupling of two linked loops (Vachaspati and Field 1994, 1995; Garriga and Vachaspati 1995). Thus parallel electric and magnetic fields in the string change the baryonic charge and can lead to cosmological baryogenesis (Barriola 1995) and to the presence of antimatter in cosmic rays (Starkman 1996).

In superconductors and in superfluid  $^3\text{He}$  an anomalous zero mode branch exists for fermions in the core of quantized vortices. For electrons in superconductors it was found first by Caroli et al. (1964), and for vortices in superfluid  $^3\text{He}$  by Kopnin (1993). One of the physically important fermionic charges in  $^3\text{He-A}$ ,  $^3\text{He-B}$  and superconductors which, like baryonic charge in the standard model, is not conserved due to the anomaly, is linear momentum. The spectral flow of momentum along the zero mode branch leads to an additional “lift” force which acts on a moving vortex.

The analogy is clearest for the continuous vortex in  $^3\text{He-A}$ , which has two quanta of the superfluid circulation,  $\nu = 2$ . This vortex is similar to the continuous  $Z$ -vortex in electroweak theory: it is characterized by a continuous distribution of the order parameter vector  $\hat{\mathbf{l}}$ , the direction of the angular momentum of the Cooper

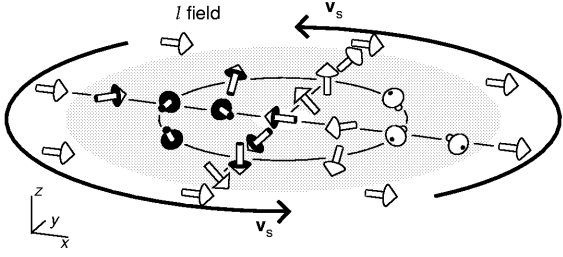


FIG. 27. The order parameter  $\hat{\mathbf{l}}$ -texture in the soft core of the continuous Anderson-Toulouse-Chechetkin vortex.

pairs (Fig. 27). When multiplied by the Fermi wavenumber  $k_F = p_F/\hbar$ , this vector acts like an effective “electromagnetic” vector potential  $\mathbf{A} = k_F \hat{\mathbf{l}}$  on the quasiparticles. The quasiparticles in  $^3\text{He-A}$ , which are close to the gap nodes, are chiral: they are either left- or right-handed (Volovik and Vachaspati 1996). As follows from BCS theory of  $^3\text{He-A}$  the sign of the of the “electric” charge  $e$ , introduced in Sec. 3.2.1, simultaneously determines the chirality of the fermions, see Eq. (166). This is clearly seen from Eq. (165) with a simple isotropic example having  $c_{\parallel} = c_{\perp} = c$ :

$$\mathcal{H} = -ec\vec{\sigma} \cdot (\mathbf{p} - e\mathbf{A}) . \quad (100)$$

A particle with positive (negative)  $e$  at the north (south) pole is left-handed (right-handed). Here  $\vec{\sigma}$  is a Bogolubov spin.

For such gapless chiral fermions the Adler-Bell-Jackiw anomaly applies and the momentum (“chiral charge”) of quasiparticles is not conserved in the presence of “electric” and “magnetic” fields, which are defined by

$$\mathbf{E} = k_F \partial_t \hat{\mathbf{l}}, \quad \mathbf{B} = k_F \nabla \times \hat{\mathbf{l}}. \quad (101)$$

In  $^3\text{He-A}$  each right-handed quasiparticle carries the momentum  $\mathbf{p}_R = p_F \hat{\mathbf{l}}$  (we reverse sign of momentum when using it as a fermionic charge), and left-handed quasiparticle has  $\mathbf{p}_L = -\mathbf{p}_R$ . According to Eq. (98) production rates for right and left handed quasiparticles are (since  $e_R^2 = e_L^2 = 1$  in this case)

$$\dot{n}_R = -\dot{n}_L = \frac{1}{4\pi} \mathbf{E} \cdot \mathbf{B}. \quad (102)$$

As a result there is a net creation of quasiparticle momentum  $\mathbf{P}$  in a time-dependent texture:

$$\partial_t \mathbf{P} = \int d^3r (\mathbf{p}_R \dot{n}_R + \mathbf{p}_L \dot{n}_L) = \frac{1}{2\pi^2} \int d^3r p_F \hat{\mathbf{l}} (\mathbf{E} \cdot \mathbf{B}) . \quad (103)$$

What we know for sure is that the total linear momentum is conserved. Then Eq. (103) means that, in the presence of the time-dependent texture, the momentum is transferred from the superfluid motion of the *vacuum* to *matter* (the heat bath of quasiparticles forming the normal component).

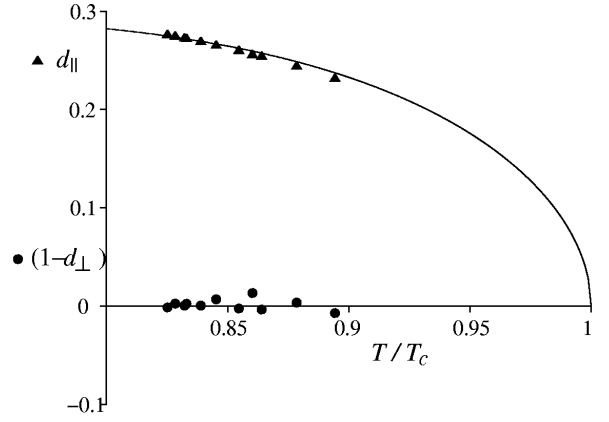


FIG. 28.  $d_{\parallel}$  and  $(1-d_{\perp})$  in the  $^3\text{He-A}$  at 29.3 bar. The curve is the theoretical fit to the data points. (From Bevan et al. 1997b).

### 3.3.2. Anomalous force acting on a continuous vortex and baryogenesis from textures

Let us consider this on the example of the simplest model of the continuous-core vortex in superfluid  $^3\text{He-A}$ . It has the following distribution of the unit vector  $\hat{\mathbf{l}}(\mathbf{r})$  which shows the direction of the point gap nodes in the smooth core

$$\hat{\mathbf{l}}(\mathbf{r}) = \hat{\mathbf{z}} \cos \eta(r) + \hat{\mathbf{r}} \sin \eta(r) , \quad (104)$$

where  $z, r, \phi$  are cylindrical coordinates. The  $\eta(r)$  is such that the  $\hat{\mathbf{l}}$ -vector in the smooth core changes from  $\hat{\mathbf{l}}(0) = -\hat{\mathbf{z}}$  to  $\hat{\mathbf{l}}(\infty) = \hat{\mathbf{z}}$ . The circulation of the superfluid velocity along the path far outside the soft core corresponds to  $\nu = 2$ :  $\oint d\mathbf{r} \cdot \mathbf{v}_s = 2\kappa$ . This means that this  $\hat{\mathbf{l}}$  texture represents the doubly quantized vortex without singularity – the continuous vortex. In the real vortex measured in the NMR experiments in the presence of external magnetic field the  $\hat{\mathbf{l}}$ -vector at infinity is fixed in the  $(x, y)$  plane (see Fig. 27 with  $\hat{\mathbf{l}}(\infty) = \hat{\mathbf{x}}$ ), but this does not change the topological structure of the vortex.

When such a continuous vortex moves in  $^3\text{He-A}$  with velocity  $\mathbf{v}_L$  it generates time dependent  $\hat{\mathbf{l}}$  texture  $\hat{\mathbf{l}} = \hat{\mathbf{l}}(\mathbf{r} - \mathbf{v}_L t)$ . Hence both an “electric” and a “magnetic” field from Eq. (101) exist and this leads to “momentogenesis”. Integration of the anomalous momentum transfer in Eq. (103) over the cross-section of the soft core of the moving vortex gives thus the additional force acting on the vortex due to spectral flow:

$$\mathbf{f}_{\text{sf}} = \partial_t \mathbf{P} = \pi \hbar \nu \mathcal{C}_0 \hat{\mathbf{z}} \times (\mathbf{v}_n - \mathbf{v}_L) . \quad (105)$$

Here  $\hat{\mathbf{z}}$  is the direction of the vortex,  $\mathcal{C}_0 = k_F^3/3\pi^2$ , and  $\mathbf{v}_n$  is the heat bath velocity. Thus we obtained the Eq. (36) with the temperature independent parameter  $\mathcal{C}(T) = \mathcal{C}_0$ .

Measurements of the mutual friction coefficients in  $^3\text{He-A}$  (Bevan et al. 1997b) provide experimental verification for the spectral flow force. According to Eq. (41)

in the A phase it should be  $d_{\perp} = (m_3\mathcal{C}_0 - \rho_n)/\rho_s$ . Value of  $m_3\mathcal{C}_0$  is the total mass density  $\rho$  in the normal phase. Its difference from  $\rho$  in superfluid phase is thus determined by the tiny effect of superfluidity on the particle density and is extremely small:  $\rho - m_3\mathcal{C}_0 \sim \rho(\Delta_0/v_F p_F)^2 = \rho(c_{\perp}/c_{\parallel})^2 \ll \rho$ . Thus one must have  $d_{\perp} \approx 1$  for all practical temperatures. The  $^3\text{He-A}$  experiments made at 29.3bar and  $T > 0.82T_c$  are consistent with this within experimental uncertainty: it was found that  $|1 - d_{\perp}| < 0.005$  as demonstrated in Fig. 28.

### 3.3.3. Anomalous force acting on a singular vortex and baryogenesis with strings

The discussion of the spectral flow in the previous sections and particularly Eq. (98) can not be directly applied to the singular vortices which are found in the  $^3\text{He-B}$  and superconductors. The reason for this is that the deviation of the magnitude of the order parameter from equilibrium value in the core of such vortices create a potential well for the core quasiparticles. In this well quasiparticles have discrete energy levels with some character separation  $\hbar\omega_0$  instead of continuous (by  $p_z$ ) spectra as have been considered above. Thus the theory of spectral flow becomes more complicated but can be constructed (Kopnin et al. 1995).

The basic idea is that discrete levels have some broadening  $\hbar/\tau$  resulting from the scattering of core excitations by free excitations in the heat bath outside the core (or by impurities in superconductors). At low temperatures when the width of levels is much less than their separation, i.e.  $\omega_0\tau \gg 1$ , the spectral flow is essentially suppressed,  $\mathcal{C}(T) = 0$ . In the opposite case of  $\omega_0\tau \ll 1$  the levels overlap and we have situation similar to the spectral flow with continuous spectra:  $\mathcal{C}(T) \approx \mathcal{C}_0$ . We may construct interpolation formula between these two cases:

$$\mathcal{C}(T) \sim \frac{\mathcal{C}_0}{1 + \omega_0^2\tau^2}. \quad (106)$$

In fact, both  $d_{\parallel}$  and  $d_{\perp}$  mutual friction coefficients are affected by this renormalization of the spectral flow force (Kopnin et al. 1995; Stone 1996):

$$d_{\parallel} - i(1 - d_{\perp}) = \frac{\rho}{\rho_s} \frac{\omega_0\tau}{1 + i\omega_0\tau} \tanh \frac{\Delta(T)}{2k_B T}. \quad (107)$$

Let us derive this equation using the Landau-type phenomenological description for the fermions in the vortex core developed by Stone (1996). For simplicity we consider the axisymmetric vortex core, the general case of the asymmetric core is discussed by Kopnin and Volovik (1998). The low-energy spectrum of Caroli-de-Gennes-Matricon quasiparticles around a vortex contains an anomalous branch of fermionic zero modes. For the

axisymmetric vortex excitations on this branch are characterized by the angular momentum  $L_z$

$$E(L_z, p_z) = -\omega_0(p_z)L_z. \quad (108)$$

For superconductors with the coherence length  $\xi$  much larger than the inverse Fermi momentum,  $p_F\xi \gg 1$ , the electron wavelength is short compared with the core size, and the quasiclassical approximation is relevant. The quasiclassical angular momentum  $L_z$  is a continuous variable; thus the anomalous branch crosses zero as a function of  $L_z$  at  $L_z = 0$  and the spectral flow can occur along this branch between the vacuum states with  $E < 0$  to the excited states with  $E > 0$ . Such spectral flow occurs during the motion of the vortex with respect to the normal component, where it is caused by the interaction with impurities in superconductors or with the thermal scattering states in superfluids. In the quasiclassical approximation, the Doppler shifted spectrum of the fermions in the moving vortex has the form

$$E(L_z, \mathbf{p}) = -\omega_0(p_z)L_z + (\mathbf{v}_s - \mathbf{v}_L) \cdot \mathbf{p}. \quad (109)$$

Here the momentum  $\mathbf{p}$  is assumed to be at the Fermi surface:  $\mathbf{p} = (p_F \sin \theta \sin \alpha, p_F \sin \theta \cos \alpha, p_F \cos \theta)$ . An azimuthal angle  $\alpha$  is the canonically conjugated to the angular momentum  $L_z$ . This allows us to write the Boltzmann equation for the distribution function,  $n(L_z, \alpha)$  at fixed  $p_z = p_F \cos \theta$ .

$$\begin{aligned} \partial_t n - \omega_0 \partial_{\alpha} n - \partial_{\alpha} ((\mathbf{v}_s - \mathbf{v}_L) \cdot \mathbf{p}) \partial_{L_z} n \\ = - \frac{n(L_z, \alpha) - n_{\text{eq}}(L_z, \alpha)}{\tau} \end{aligned} \quad (110)$$

where the collision time  $\tau$  characterizes the interaction of the bound state fermions with impurities or with the thermal fermions in the normal component outside the vortex core and equilibrium distribution function is:

$$\begin{aligned} n_{\text{eq}}(L_z, \alpha) = \\ f(E - (\mathbf{v}_n - \mathbf{v}_L) \cdot \mathbf{p}) = f(-\omega_0 L_z + (\mathbf{v}_s - \mathbf{v}_n) \cdot \mathbf{p}) \end{aligned} \quad (111)$$

where  $f(E) = (1 + \exp(E/T))^{-1}$  is the Fermi-function.

Introducing the shifted variable

$$l = L_z - (\mathbf{v}_s - \mathbf{v}_n) \cdot \mathbf{p} / \omega_0, \quad (112)$$

one obtains the equation for  $n(l, \alpha)$

$$\begin{aligned} \partial_t n - \omega_0 \partial_{\alpha} n - \partial_{\alpha} ((\mathbf{v}_n - \mathbf{v}_L) \cdot \mathbf{k}) \partial_l n \\ = - \frac{n(l, \alpha) - f(-\omega_0 l)}{\tau}, \end{aligned} \quad (113)$$

which does not contain  $\mathbf{v}_s$ . To find the force acting on the vortex from the heat bath environment, we are interested in the evolution of the total momentum of quasiparticles in the vortex core:

$$\mathbf{P} = \sum \mathbf{p} = \int_{-p_F}^{p_F} \frac{dp_z}{2\pi} \mathbf{P}(p_z), \quad \mathbf{P}(p_z) = \frac{1}{2} \int dl \frac{d\alpha}{2\pi} n(l, \alpha) \mathbf{p} \quad (114)$$

It appears that the equation for  $\mathbf{P}(p_z)$  can be written in a closed form

$$\partial_t \mathbf{P}(p_z) - \omega_0 \hat{z} \times \mathbf{P}(p_z) + \frac{\mathbf{P}(p_z)}{\tau} = -\frac{1}{4} p_F^2 \sin^2 \theta \hat{z} \times (\mathbf{v}_n - \mathbf{v}_L) (f(\Delta(T)) - f(-\Delta(T))). \quad (115)$$

Here we take into account that  $\int dl \partial_l n$  is limited by the bound states below the gap  $\Delta(T)$  of the bulk liquid: above the gap  $\Delta(T)$  the spectrum of fermions is continuous, i.e. the interlevel distance  $\omega_0 = 0$ .

In the steady state vortex motion one has  $\partial_t \mathbf{P}(p_z) = 0$ . Then, since  $f(\Delta(T)) - f(-\Delta(T)) = \tanh(\Delta(T)/2T)$ , one obtains the following contribution to the momentum from the heat bath to the core fermions due to the spectral flow of bound states below  $\Delta(T)$

$$\mathbf{F}_{\text{bsf}} = \int_{-p_F}^{p_F} \frac{dp_z}{2\pi} \frac{\mathbf{P}(p_z)}{\tau} = \frac{\kappa}{4} \tanh \frac{\Delta(T)}{2T} \times \int_{-p_F}^{p_F} \frac{dp_z}{2\pi} \frac{p_F^2 - p_z^2}{1 + \omega_0^2 \tau^2} [(\mathbf{v}_L - \mathbf{v}_n) \omega_0 \tau + \hat{z} \times (\mathbf{v}_L - \mathbf{v}_n)]. \quad (116)$$

The spectral flow of unbound states above  $\Delta(T)$  is not suppressed, the corresponding  $\omega_0 \tau = 0$ , since the distance between the levels in the continuous spectrum is  $\omega_0 = 0$ . This gives

$$\mathbf{F}_{\text{usf}} = \frac{\kappa}{4} p_F^2 \int_{-p_F}^{p_F} \frac{dp_z}{2\pi} \sin^2 \theta \left( 1 - \tanh \frac{\Delta(T)}{2T} \right) \hat{z} \times (\mathbf{v}_L - \mathbf{v}_n). \quad (117)$$

Thus the total nondissipative (transverse) and frictional (longitudinal) parts of the spectral-flow force are

$$\mathbf{F}_{\text{sf}}^\perp = \frac{\kappa}{4} \int_{-p_F}^{p_F} \frac{dp_z}{2\pi} (p_F^2 - p_z^2) \times \left[ 1 - \tanh \frac{\Delta(T)}{2T} \frac{\omega_0^2 \tau^2}{1 + \omega_0^2 \tau^2} \right] \hat{z} \times (\mathbf{v}_L - \mathbf{v}_n), \quad (118)$$

$$\mathbf{F}_{\text{sf}}^\parallel = (\mathbf{v}_L - \mathbf{v}_n) \frac{\kappa}{4} \tanh \frac{\Delta(T)}{2T} \times \int_{-p_F}^{p_F} \frac{dp_z}{2\pi} (p_F^2 - p_z^2) \frac{\omega_0 \tau}{1 + \omega_0^2 \tau^2} \quad (119)$$

In the limit  $\omega_0 \tau \ll 1$  the friction force disappears, while the transverse spectral flow force is maximal and coincides with that obtained for the continuous vortex in Eq. (105) with the same value of  $\mathcal{C}_0 = (1/4) \int_{-p_F}^{p_F} dp_z (p_F^2 - p_z^2) = p_F^3/3\pi^2$ . In general case the result in Eqs.(118),(119) is complicated since both  $\omega_0$

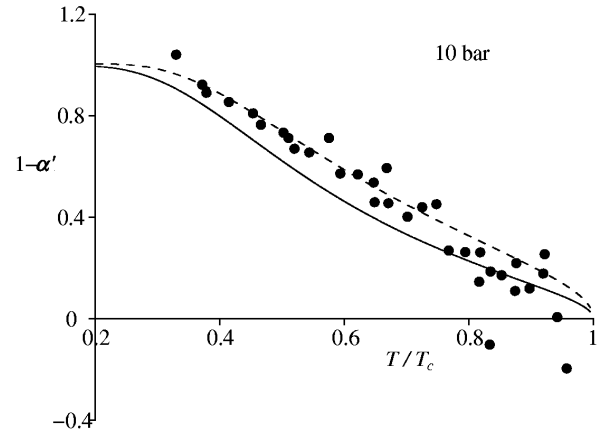


FIG. 29. Experimental values of  $1 - \alpha'$  in  $^3\text{He-B}$  at 10 bar compared with theoretical prediction Eq. (120). The full curve is for the theoretical value of  $\Delta(T)$  and the broken curve is the fit with reduced  $\Delta$ . (From Bevan et al. 1997b).

and  $\tau$  depend on  $p_z$ . However if one neglects this dependence and add the Magnus and Iordanskii forces one obtains the Eq. (107) for all  $T$ . If the temperature is not too high, so that  $\tanh \Delta(T)/2T \approx 1$ , one obtains the Eq. (106) for the renormalized spectral flow parameter.

Comparison of Eq. (107) with experiment should take into account that neither  $\omega_0$  nor  $\tau$  are known with good accuracy. However the following combination of the mutual friction coefficients does not depend on these parameters explicitly:

$$1 - \alpha' = \frac{1 - d_\perp}{d_\parallel^2 + (1 - d_\perp)^2} = \frac{\rho_s}{\rho} \left[ \tanh \frac{\Delta(T)}{2k_B T} \right]^{-1}. \quad (120)$$

This equation is compared to the experimental data on mutual friction in  $^3\text{He-B}$  (Bevan et al. 1997b) in Fig. 29. The agreement is excellent in view of the approximations in the theory.

This shows that the chiral anomaly is relevant for the interaction of condensed matter vortices (analogue of strings) with fermionic quasiparticles (analogue of quarks and leptons). For continuous vortices in  $^3\text{He-A}$  the spectral flow of fermions between the vacuum (superfluid ground state) and matter (heat bath of positive energy particles forming the normal component) dominates at any relevant temperature. For singular vortices in  $^3\text{He-B}$  it is important at  $T \sim T_c$  and vanishes at  $T \ll T_c$ .

It is interesting that for a homogeneous vacuum the fermionic charge (momentum) is conserved separately in the vacuum (ground state) and in the heat bath of excitations. Topological defects are thus the mediators of the transfer of momentum between these two subsystems. The motion of a vortex across the flow changes both the topological charge of the vacuum (say, the winding number of superflow in a torus geometry) and the fermionic charge (angular momentum in the same geometry). All

these processes are similar to those involved in the cosmological production of baryons and can thus be investigated in detail.

However, it is important to note that although the spectral flow leads to anomalous creation of fermionic charge from the vacuum, the total fermionic charge of the vacuum plus matter remains conserved. There is also no intrinsic bias in this process for the direction of the charge transfer: from vacuum to matter or in the opposite direction. Thus, the necessary conditions for the operation of this mechanism, if the non-trivial result like the apparent positive baryonic charge of the matter in our Universe is required, are the system in non-equilibrium state plus some symmetry breaking which biases the direction of the charge transfer. How such conditions may be realized in the early Universe is not clear now. But it is strongly believed that the broken P and CP invariances play crucial role.

In the  ${}^3\text{He}$  case the situation is completely under control: The relevant symmetry breaking is modeled by applying rotation or a magnetic field, while the nonequilibrium case can be achieved by applying an external superflow or acceleration.

Thus the experimental verification of momentogenesis in superfluid  ${}^3\text{He}$  supports current ideas on cosmological baryogenesis via spectral flow and points to a future where several cosmological problems can be modeled and studied in  ${}^3\text{He}$ . Now let us consider the opposite effect which leads to the analog of magnetogenesis.

#### 3.4. Analog of magnetogenesis: vortex textures generated by normal-superfluid counterflow

From Eq. (98) it follows that the magnetic field configuration can absorb the fermionic charge. If this magnetic field has a helicity, it acquires an excess of right-moving particles over the left-moving particles:

$$(n_R - n_L)_{\mathbf{A}} = \frac{1}{2\pi^2} \mathbf{A} \cdot (\nabla \times \mathbf{A}) . \quad (121)$$

The right-hand side is the so called Chern-Simons (or topological) charge of the magnetic field.

The transformation of particles into a magnetic field configuration opens the possibility for the cosmological origin of galactic magnetic fields from a system of fermions. This is the essential step in the scenario described by Joyce and Shaposhnikov (1997). In this scenario the initial excess of the right electrons,  $e_R$ , could have been generated in the early Universe. This excess could survive until the electroweak phase transition (at about  $10^{-10}$  s after the big bang) when anomalous lepton (and baryon) number violating processes become efficient to erase the excess. However it appears that well before the electroweak transition the instability develops, at which the excess of the right electrons is transformed

into a hypermagnetic field. Then, when the electroweak transition occurs, it transforms a part of the hypermagnetic field into the electromagnetic field, so that the universe contains a primordial (electromagnetic) magnetic field.

Now we discuss the corresponding process of the fermionic charge to magnetic field transformation in  ${}^3\text{He-A}$ . In our case it is the quasiparticle momentum, which plays the part of the relevant fermionic charge. The net quasiparticle momentum is generated by the relative flow of normal and superfluid components. This fermionic charge is transformed via the chiral anomaly into the order parameter texture, which as we have seen plays the part of the magnetic field. This transformation occurs as the instability of the excess of the momentum towards the formation of the  $\hat{\mathbf{l}}$ -textures and represents the counterflow instability in  ${}^3\text{He-A}$ , which has been intensively discussed theoretically and recently investigated experimentally in the Helsinki rotating cryostat (Ruutu et al. 1997b). Thus the  ${}^3\text{He-A}$  analogy closely follows the cosmological scenario described by Joyce and Shaposhnikov (1997).

Let us discuss this instability. In the presence of counterflow,  $\mathbf{w} = \mathbf{v}_n - \mathbf{v}_s$ , of the normal component of  ${}^3\text{He-A}$  liquid with respect to the superfluid, the  $\hat{\mathbf{l}}$ -vector is oriented along the flow,  $\hat{\mathbf{l}}_0 \parallel \mathbf{w}$ . We are interested in the stability condition for such homogeneous counterflow towards generation of the inhomogeneous perturbations  $\delta\hat{\mathbf{l}}$

$$\hat{\mathbf{l}} = \hat{\mathbf{l}}_0 + \delta\hat{\mathbf{l}}(\mathbf{r}, t) , \quad (122)$$

keeping in mind that the space and time dependence of  $\delta\hat{\mathbf{l}}$  correspond to ‘‘hyperclectric field’’  $\mathbf{E} = k_F \partial_t \delta\hat{\mathbf{l}}$  and a ‘‘hypermagnetic field’’  $\mathbf{B} = k_F \nabla \times \delta\hat{\mathbf{l}}$ .

It is important for our consideration that the  ${}^3\text{He-A}$  liquid is anisotropic in the same manner as a nematic liquid crystal. For the relativistic fermions this means that their motion is determined by the geometry of some effective spacetime which in  ${}^3\text{He-A}$  is described by the metric tensor in Eq. (79). As we have already discussed above, in the presence of counterflow the energy of quasiparticles is Doppler shifted by the amount  $\mathbf{p} \cdot \mathbf{w}$ . Since the quasiparticles are concentrated near the gap nodes, this energy shift is constant and opposite for two gap nodes:  $\mathbf{p} \cdot \mathbf{w} \approx \pm p_F (\hat{\mathbf{l}}_0 \cdot \mathbf{w})$ . The counterflow therefore produces what would be an effective chemical potential in particle physics, which has opposite sign for the right- and left-handed particles:

$$\mu_R = -\mu_L = p_F (\hat{\mathbf{l}}_0 \cdot \mathbf{w}) . \quad (123)$$

The kinetic energy of the counterflow is

$$E_{\text{kin}} = \frac{1}{2} \mathbf{w} \rho_{n\parallel} \mathbf{w} . \quad (124)$$

Here the density of the normal component is a tensor in the anisotropic  ${}^3\text{He-A}$ , and only the longitudinal component  $\rho_{n\parallel}$  is involved.

Let us consider the low-temperature limit  $T \ll T_c$ , where  $T_c \sim \Delta_0$  is the superfluid transition temperature. Then using expression for the longitudinal density of the normal component of  $^3\text{He-A}$  (Vollhardt and Wölfle 1990)

$$\rho_{n\parallel} = \pi^2 \rho \frac{m_3^*}{m_3} \left( \frac{k_B T}{\Delta_0} \right)^2 \quad (125)$$

and also the  $^3\text{He-A}$  equivalent of the chemical potential (123) one obtains

$$E_{\text{kin}} \approx \frac{1}{6} m_3^* k_F^3 \frac{T^2}{\Delta_0^2} (\hat{\mathbf{l}}_0 \cdot \mathbf{w})^2 \equiv \frac{1}{6} \sqrt{-g} T^2 \mu_R^2 . \quad (126)$$

In the last equality an over-all constant appears to be the square root of the determinant of an effective metric in  $^3\text{He-A}$ :  $\sqrt{-g} = 1/c_{\parallel} c_{\perp}^2 = m_3^* k_F / \Delta_0^2$ . In relativistic theories the rhs of Eq. (126) is exactly the energy density of the massless right-handed electrons in the presence of the chemical potential  $\mu_R$ . Thus the kinetic energy, stored by the counterflow, is exactly analogous to the energy stored by the right-handed electrons. The same analogy occurs between the net quasiparticle linear momentum,  $\mathbf{P} = \rho_n \mathbf{w}$ , along  $\hat{\mathbf{l}}_0$  and the chiral charge of the right electrons:

$$n_R \equiv \frac{1}{p_F} \mathbf{P} \cdot \hat{\mathbf{l}}_0 . \quad (127)$$

The inhomogeneity which absorbs the fermionic charge, is represented by a magnetic field configuration in real physical vacuum and by a  $\delta\hat{\mathbf{l}}$ -texture in  $^3\text{He-A}$ . However, Eq. (121) applies in both cases, if in  $^3\text{He-A}$  we use the standard identification  $\mathbf{A} = k_F \delta\hat{\mathbf{l}}$ .

Just as in the particle physics case, we now consider the instability towards the production of the “magnetic” texture due to the excess of chiral particles. This instability can be seen by considering the gradient energy of the inhomogeneous texture on the background of the superflow. In the geometry of the superflow, the textural contribution to the free energy of the  $\delta\hat{\mathbf{l}}$ -vector is completely equivalent to the conventional energy of the hypermagnetic field (Volovik 1992b)

$$\begin{aligned} F_{\text{grad}} &= \ln \left( \frac{\Delta_0^2}{T^2} \right) \frac{p_F^2 v_F}{24\pi^2 \hbar} (\hat{\mathbf{l}}_0 \times (\nabla \times \delta\hat{\mathbf{l}}))^2 \\ &\equiv \frac{\sqrt{-g}}{4\pi e_{\text{eff}}^2} g^{ij} g^{kl} F_{ik} F_{jl} = F_{\text{magn}} . \end{aligned} \quad (128)$$

Here  $F_{ik} = \nabla_i A_k - \nabla_k A_i$  and we again have included the effective anisotropic metric in Eq. (79) appropriate for  $^3\text{He-A}$ .

It is interesting that the logarithmic factor in the gradient energy plays the part of the running coupling  $e_{\text{eff}}^{-2} = (1/3\pi\hbar c) \ln(\Delta_0/T)$  in particle physics, where  $e_{\text{eff}}$  is the effective hyperelectric charge; while the gap amplitude  $\Delta_0$ , the ultraviolet cutoff, plays the part of the

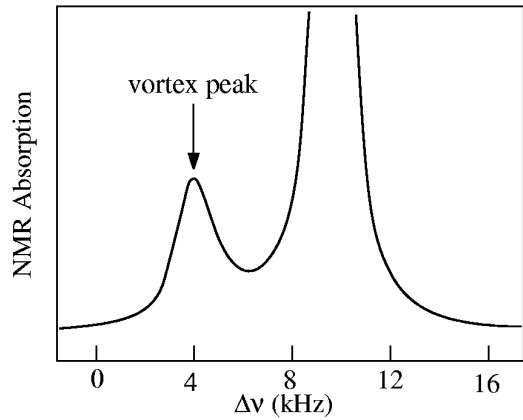


FIG. 30. The NMR signal from array of ATC vortices in the container. The position of the satellite peak indicates the type of the vortex, while the intensity is proportional to the number of vortices of this type in the cell.

Planck energy scale. Now if one has the counterflow in  $^3\text{He-A}$ , or its equivalent – an excess of chiral charge produced by the chemical potential  $\mu_R$  – the anomaly gives rise to an additional effective term in the magnetic energy, corresponding to the interaction of the charge absorbed by the magnetic field with the chemical potential. This effective energy term is:

$$\begin{aligned} F_{CS} &= (n_R - n_L) \mu_R = \frac{1}{2\pi^2} \mu_R \mathbf{A} \cdot (\nabla \times \mathbf{A}) \\ &= \frac{3\hbar}{2m} \rho (\hat{\mathbf{l}}_0 \cdot \mathbf{w}) (\delta\hat{\mathbf{l}} \cdot \nabla \times \delta\hat{\mathbf{l}}) , \end{aligned} \quad (129)$$

The right-hand side corresponds to the well known anomalous interaction of the counterflow with the  $\hat{\mathbf{l}}$ -texture in  $^3\text{He-A}$ , where  $\rho$  is the mass density of  $^3\text{He}$  (Volovik 1992b) (the additional factor of 3/2 enters due to nonlinear effects).

For us the most important property of this term is that it is linear in the derivatives of  $\delta\hat{\mathbf{l}}$ . Its sign thus can be negative, while its magnitude can exceed the positive quadratic term in Eq. (128). This leads to the helical instability where the inhomogeneous  $\delta\hat{\mathbf{l}}$ -field is formed. During this instability the kinetic energy of the quasiparticles in the counterflow (analog of the energy stored in the fermionic degrees of freedom) is converted into the energy of inhomogeneity  $\nabla \times \delta\hat{\mathbf{l}}$ , which is the analog of the magnetic energy of the hypercharge field.

When the helical instability develops in  $^3\text{He-A}$ , the final result is the formation of a  $\hat{\mathbf{l}}$ -texture, which corresponds to the free energy minimum in the rotating container. This is a periodic  $\hat{\mathbf{l}}$ -texture, where the elementary cell represents a so-called Anderson-Toulouse-Chechetkin (ATC) continuous vortex (Fig. 27). ATC vortices give rise to a characteristic satellite peak in the  $^3\text{He}$  NMR absorption spectrum: their number is directly proportional to the height of this peak (Fig. 30, see also Fig. 35

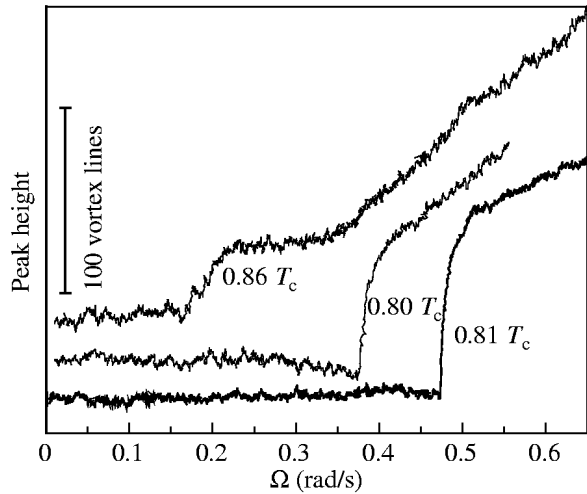


FIG. 31. Time dependence of the satellite peak height of the continuous vortices. Initially vortices are not present in the vessel. When the velocity of the counterflow  $\mathbf{w}$  in the  $\hat{\mathbf{l}}_0$  direction (corresponding to the chemical potential  $\mu_R$  of the chiral electrons) exceeds some critical value, the instability occurs and the container becomes filled with the  $\hat{\mathbf{l}}$ -texture (hypermagnetic field) forming the vortex array.

with satellite peaks from different topological objects in rotating  $^3\text{He-A}$ .

In acceleration of the container into rotation, starting from the state with vortex-free counterflow (ie. with fermionic charge, but no hypermagnetic field), the helical instability is observed as a sudden discontinuity, when the vortex satellite is formed (Fig. 31). The peak height jumps from zero to a magnitude which almost corresponds to the equilibrium vortex state, which means that the counterflow is essentially reduced. Most of the counterflow (fermionic charge) thus becomes converted into vortex texture (magnetic field).

Together with the results by Bevan et al. (1997a), this shows that the chiral anomaly is an important mechanism for the interaction of vortex textures (the analogue of the hypercharge magnetic fields and cosmic strings) with fermionic excitations (analogue of quarks and leptons). These two experiments verified both processes which are induced by the anomaly: the nucleation of fermionic charge from the vacuum observed by Bevan et al. (1997a) and the inverse process of the nucleation of an effective magnetic field from the fermion current as observed by Krusius et al. (1998).

### 3.5. Vortex mass: chiral fermions in strong magnetic field

Till now we assumed that the mass  $M_V$  of the vortex can be neglected in the vortex dynamics: The term  $M_V \partial_t \mathbf{v}_L$  in the force balance equation for the vortex contains the time derivative and thus at low frequencies of

the vortex motion it can be neglected compared to the other forces, which are directly proportional to  $\mathbf{v}_L$ . Here we estimate the vortex mass in the BCS superfluids and superconductors and relate it to the peculiar phenomena in quantum field theory. There are several contributions to the mass of the vortex. We start from the contribution, which is relevant for the Bose superfluid  $^4\text{He}$ .

#### 3.5.1. “Relativistic” mass of the vortex

In the hydrodynamic theory the mass of the vortex is nonzero due to compressibility of the liquid. Since the sound propagation in fluids is similar to the light propagation in the vacuum, the hydrodynamic energy of the vortex, soliton or other extended object moving in the liquid is connected with its hydrodynamic mass by per unit length by the “relativistic” equation,  $E = ms^2$  where the speed of sound  $s$  substitutes the speed of light (Davis 1992; Duan 1995; Kao and Lee 1995; Iengo and Jug 1995; Wexler and Thouless 1996). Thus the hydrodynamic mass of the vortex loop of length  $L$  at  $T = 0$  is according to Eq. (17):

$$M_{\text{compr}} = \frac{E_{\text{kin}}}{s^2} = \frac{\rho \kappa^2 L}{4\pi s^2} \ln \frac{L}{\xi}. \quad (130)$$

For Fermi superfluids  $s$  is of order the Fermi velocity  $v_F \sim p_F/m$  ( $m$  is the mass of the electron in metals or of the  $^3\text{He}$  atom), and the estimation for the hydrodynamic mass of the vortex loop of length  $L$  is  $M_{\text{compr}} \sim \rho a^2 L \ln L/\xi$ , where  $a$  is interatomic distance. For superfluid  $^4\text{He}$ , where the core size  $\xi \sim a$ , this hydrodynamic vortex mass is of order the mass of the liquid concentrated in the vortex core,  $\sim \rho a^2 L$ . However for superfluid phases of  $^3\text{He}$  and for superconductors, where  $\xi \gg a$ , it is much less than  $\rho \xi^2 L$  and the other contributions become important.

#### 3.5.2. Bound states contribution to the mass of singular vortex

It appears that the most important contribution to the vortex mass originates from the quasiparticle occupying the bound states in the vortex core and thus forming the normal component concentrated in the core. For the vortices in conventional superconductors and in  $^3\text{He-B}$  this contribution to the vortex mass depends on  $\omega_0 \tau$  and in the clean limit case it is proportional to the mass of the liquid in the vortex core, as was first found by Kopnin (1978) in superconductors and by Kopnin and Salomaa (1991) in superfluid  $^3\text{He-B}$ :  $M_{\text{Kopnin}} \sim \rho \xi^2 L$ . This core mass is essentially larger than the logarithmically divergent contribution, which comes from the compressibility. In spite of the logarithmic divergence, the latter contains the speed of sound in the denominator and thus is smaller

by factor  $(a/\xi)^2 \ll 1$ , where  $a$  is the interatomic distance. The compressibility mass of the vortex dominates in Bose superfluids, where the core size is small,  $\xi \sim a$ .

According to Kopnin theory the core mass comes from the fermions trapped in the vortex core (Kopnin 1978; Kopnin and Salomaa 1991; van Otterlo et al. 1995; Volovik 1997; Kopnin and Vinokur 1998). This Kopnin mass of the vortex can be derived using the phenomenological approach. Let us consider the limit of low  $T$  and the superclean regime  $\omega_0\tau \gg 1$  (Volovik 1997). If the vortex moves with velocity  $\mathbf{v}_L$  with respect to the superfluid component, the fermionic energy spectrum in the vortex frame is Doppler shifted and has the form in Eq. (109):  $E = E_0(\nu) - \mathbf{p} \cdot \mathbf{v}_L$ , where  $\nu$  stands for the fermionic degrees of freedom in the stationary vortex. The summation over fermionic degrees of freedom leads to the extra linear momentum of the vortex  $\propto \mathbf{v}_L$ :

$$\mathbf{P} = \sum_{\nu} \mathbf{p} \theta(-E) = \sum_{\nu} \mathbf{p}(\mathbf{k} \cdot \mathbf{v}_L) \delta(E_0) = M_{\text{Kopnin}} \mathbf{v}_L,$$

$$M_{\text{Kopnin}} = \frac{1}{2} \sum_{\nu} \mathbf{p}_{\perp}^2 \delta(E_0). \quad (131)$$

For the axisymmetric vortex, where  $E_0 = -L_z \omega_0(p_z)$  and  $\sum_{\nu} = \int dL_z dp_z dz / 2\pi$ , one has

$$M_{\text{Kopnin}} = L \int_{-p_F}^{p_F} \frac{dp_z}{4\pi} \frac{p_F^2 - p_z^2}{\omega_0(p_z)} \quad (132)$$

The Eq. (132) can be also obtained from the time dependent kinetic equation (110). It is the coefficient in the contribution to the longitudinal force, which is linear in external frequency  $\omega$ :  $\mathbf{F}_{\text{sf}}^{\parallel} = -i\omega M_{\text{Kopnin}} \mathbf{v}_L$ .

Note that this vortex mass is determined in essentially the same way as the normal component density in the bulk system. The Kopnin vortex mass is nonzero if the density of fermionic states is finite in the vortex core which is determined by the interlevel spacing  $\omega_0$  in the core:  $N(0) \propto 1/\omega_0$ . That gives for the Kopnin vortex mass per unit length an estimation:  $M_{\text{Kopnin}} \sim p_F^3/\omega_0 \sim \rho \xi^2$ . The more stronger connection to the normal component fraction in the core will be given in the next subsection on the example of the continuous vortex core.

### 3.5.3. Kopnin mass of continuous vortex: connection to chiral fermions in magnetic field.

The continuous-core vortex in  $^3\text{He-A}$  is the best model which helps to understand the vortex core mass. The continuous-core model can be also considered in the other Fermi superfluids and superconductors: the singular core can be smoothen, so that the  $1/r$ -singularity of the superfluid velocity is removed, by introducing the point gap nodes in the core region (Fig. 32). As a result the superfluid/superconducting state in the vortex core of any system acquires the properties of the A-phase of superfluid

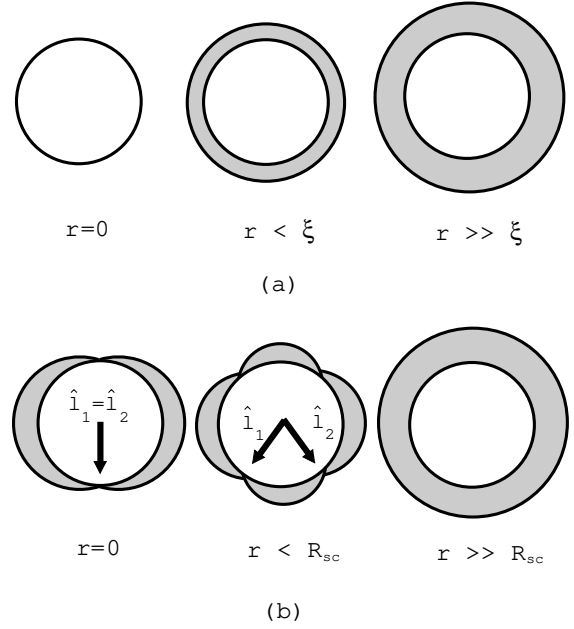


FIG. 32. Smoothing of the singular vortex core. (a) In the singular vortex the gap continuously decreases and becomes zero on the vortex axis (at  $r = 0$ ) (b) For some vortices it is energetically favourable to escape the nullification of the order parameter at  $r = 0$ . Instead, within the smooth core,  $r < R_{\text{sc}}$ , the point gap nodes appear in the spectrum of fermions (Volovik and Mineev 1982). The unit vectors  $\hat{\mathbf{I}}_1$  and  $\hat{\mathbf{I}}_2$  show the directions to the nodes at different  $r$ . Close to the gap nodes the spectrum of fermions is similar to that in  $^3\text{He-A}$ .

$^3\text{He}$  with its continuous vorticity and point gap nodes (Volovik and Mineev 1982; Salomaa and Volovik 1987). After that one can easily separate different contributions to the vortex mass. Actually this is not only the model: The spontaneous smoothening of the velocity singularity occurs in the core of both types of vortices observed in  $^3\text{He-B}$  (Salomaa and Volovik 1987); in heavy fermionic and high- $T_c$  superconductors such smoothening can occur due to admixture of different pairing states in the vortex core.

For the smoothened singly quantized vortices in  $^3\text{He-B}$  and superconductors one has two  $\hat{\mathbf{I}}$ -vectors:  $\hat{\mathbf{I}}_1$  and  $\hat{\mathbf{I}}_2$ , each for each of two spin projections. The simplest distribution of both fields is given by Eq. (104) with such  $\eta(r)$  that  $\hat{\mathbf{I}}_1(0) = \hat{\mathbf{I}}_2(0) = -\hat{\mathbf{z}}$  and  $\hat{\mathbf{I}}_1(\infty) = -\hat{\mathbf{I}}_2(\infty) = \hat{\mathbf{r}}$  (Salomaa and Volovik 1987). The region of radius  $R_{\text{sc}}$ , where the texture of  $\hat{\mathbf{I}}$ -vectors is concentrated, represents the smoothened (or soft) core of the vortex.

For the continuous vortex the normal component associated with the vortex can be considered as the local quantity, determined at each point in the vortex core. Such consideration is valid for the smooth core with the radius  $R_{\text{sc}} \gg \xi$ , where the local classical description of the fermionic spectrum can be ap-

plied. The main contribution comes from the point gap nodes, where the classical spectrum has the form  $E_0 = \sqrt{v_F^2(p - p_F)^2 + \Delta_0^2(\hat{\mathbf{p}} \times \hat{\mathbf{l}})^2}$  and  $\Delta_0$  is the gap amplitude. In the presence of the gradient of  $\hat{\mathbf{l}}$ -field, which acts on the quasiparticles as an effective magnetic field, this gapless spectrum leads to the nonzero local DOS, discussed in Sec. 3.3.1 for the relativistic chiral fermions. To apply the DOS in Eq. (97) to the case of the anisotropic  $^3\text{He-A}$ , one must make the covariant generalization of DOS introducing the general metric tensor and then substitute it by the effective  $^3\text{He-A}$  metrics which describes the anisotropy of  $^3\text{He-A}$ . The general form of the DOS of the chiral fermions in the curved space is

$$N(0) = \frac{|e|}{2\pi^2} \sqrt{-g} \sqrt{\frac{1}{2} g^{ij} g^{kl} F_{ik} F_{jl}}, \quad (133)$$

where  $F_{ik}$  is defined on p. 48. One now can apply this to the  $^3\text{He-A}$  where  $|e| = 1$ , and the metric tensor is given by Eq. (79). Neglecting the dependence of the small velocity field  $v_s$  in the smooth core, one obtains the following local DOS for the fermions in the  $\hat{\mathbf{l}}$ -texture at  $T = 0$ :

$$N(0, \mathbf{r}) = \frac{p_F^2}{2\pi^2 \Delta_A} |(\hat{\mathbf{l}} \times (\vec{\nabla} \times \hat{\mathbf{l}}))| \quad (134)$$

This DOS can be inserted to the expression for the local density of the normal component at  $T = 0$  (see Eq. (5.24) in the review by Volovik (1990)):

$$(\rho_n)_{ij}(\mathbf{r}) = \hat{l}_i \hat{l}_j p_F^2 N(0, \mathbf{r}). \quad (135)$$

For the axisymmetric continuous vortex one has

$$N(0, \mathbf{r}) = \frac{p_F^2}{2\pi^2 \Delta_A} \sin \eta |\partial_r \eta|. \quad (136)$$

The integral of this normal density tensor over the cross section of the soft core gives the Kopnin mass of the vortex in the local density representation

$$\begin{aligned} M_{\text{Kopnin}} &= \int d^2 r (\hat{\mathbf{v}}_L \cdot \hat{\mathbf{l}})^2 p_F^2 N(0, \mathbf{r}) \\ &= \frac{p_F^2}{4\pi^2 \Delta_A} \int d^2 r \sin^3 \eta(r) |\partial_r \eta| \end{aligned} \quad (137)$$

where  $\hat{\mathbf{v}}_L$  is the unit vector in the direction of vortex velocity. The same equation for the mass can be obtained from Eq. (132) using the exact expression for the inter-level distance  $\omega_0(p_z)$  (Volovik 1997).

Since  $v_F/\Delta_0 \sim \xi$  one obtains that the Kopnin mass of the continuous vortex  $\sim \rho \xi R_{\text{sc}}$ , i.e. it is linear in the dimension  $R_{\text{sc}}$  of the core (Kopnin 1995). Thus it follows that the area law for the vortex mass is valid only for vortices with the core size of order  $\xi$  (i.e.  $R_{\text{sc}} \sim \xi$ ).

Note that the vortex mass discussed comes from the normal component trapped by the vortex and thus moving with the vortex velocity,  $\mathbf{v}_n = \mathbf{v}_L$ . In this consideration it was assumed that  $\omega_0 \tau \gg 1$ . In this limit the

normal component in the core and the normal component in the heat bath do not interact with each other and thus can move with different velocities. The local hydrodynamic energy of the normal component trapped by the vortex is

$$F = \frac{1}{2} (\rho_n)_{ij}(\mathbf{r}) (\mathbf{v}_L - \mathbf{v}_s)_i (\mathbf{v}_L - \mathbf{v}_s)_j \quad (138)$$

This can be rewritten in the form, which is valid also for the chiral fermions:

$$F = \frac{\mu_R^2 + \mu_L^2}{8\pi^2} \sqrt{-g} \sqrt{\frac{1}{2} g^{ij} g^{kl} F_{ik} F_{jl}} \quad (139)$$

where, as before in Eq. (123), the chemical potential of the left and right fermions in  $^3\text{He-A}$  are expressed in terms of the counterflow:  $\mu_R = -\mu_L = p_F(\hat{\mathbf{l}} \cdot \mathbf{w})$ . The Eq. (139) represents the magnetic energy of the chiral particles with finite chemical potential in strong magnetic field  $B \gg \mu^2$ .

#### 3.5.4. Associated hydrodynamic mass

Recently the problem of another vortex mass of the hydrodynamics origin was raised by Sonin et al. (1998). It is the so-called backflow mass discussed by Baym and Chandler (1983), which also can be proportional to the core area. Here we compare these two contributions in the superclean regime and at low  $T \ll T_c$  using the model of the continuous core. The associated (or induced) mass appears when, say, an external body moves in the superfluid. This mass depends on the geometry of the body. For the moving cylinder of radius  $R$  it is the mass of the liquid displaced by the cylinder,

$$M_{\text{associated}} = \pi R^2 \rho, \quad (140)$$

which is to be added to the actual mass of the cylinder to obtain the total inertial mass of the body. In superfluids this part of superfluid component moves with external body and thus can be associated with the normal component. The similar mass is responsible for the normal component in porous materials and in aerogel, where some part of superfluid is hydrodynamically trapped by the pores. It is removed from the overall superfluid motion and thus becomes the part of the normal component.

In the case when the vortex is trapped by the wire of radius  $R_{\text{wc}} \gg \xi$ , such that the vortex core is represented by the wire, the Eq. (140) gives the vortex mass due to the backflow around the moving core. This is the simplest realization of the backflow mass of the vortex discussed by Baym and Chandler (1983). For such vortex with the wire-core the Baym-Chandler mass is the dominating mass of the vortex. The Kopnin mass which can result from the normal excitations trapped near the surface of the wire is essentially less.

Let us now consider the Baym-Chandler mass for the free vortex at  $T = 0$  using again the continuous-core model. In the wire-core vortex this mass arises due to the backflow caused by the inhomogeneity of  $\rho_s$ :  $\rho_s(r > R_{\text{wc}}) = \rho$  and  $\rho_s(r < R_{\text{wc}}) = 0$ . Similar but less severe inhomogeneity of  $\rho_s = \rho - \rho_n$  occurs in the continuous-core vortex due to the nonzero local normal density in Eq. (135). Due to the profile of the local superfluid density the external flow is disturbed near the core according to continuity equation

$$\nabla \cdot (\rho_s \mathbf{v}_s) = 0 \quad . \quad (141)$$

If the smooth core is large,  $R_{\text{sc}} \gg \xi$ , the deviation of the superfluid component in the smooth core from its asymptotic value outside the core is small:  $\delta\rho_s = \rho - \rho_s \sim (\xi/R_{\text{sc}})\rho \ll \rho$  and can be considered as perturbation. Thus if the asymptotic value of the velocity of the superfluid component with respect of the core is  $\mathbf{v}_{s0} = -\mathbf{v}_L$ , the disturbance  $\delta\mathbf{v}_s = \nabla\Phi$  of the superflow in the smooth core is given by:

$$\rho\nabla^2\Phi = v_{s0}^i \nabla^j (\rho_n)_{ij} \quad . \quad (142)$$

The kinetic energy of the backflow gives the Baym-Chandler mass of the vortex

$$M_{\text{BC}} = \frac{\rho}{v_{s0}^2} \int d^2r (\nabla\Phi)^2 \quad , \quad (143)$$

In the simple approximation, when the normal component in Eq. (135) is considered as isotropic, one obtains

$$M_{\text{BC}} = \frac{1}{2\rho} \int d^2r \rho_n^2(r) \sim \rho\xi^2 \quad . \quad (144)$$

The Baym-Chandler mass does not depend on the core radius  $R_{\text{sc}}$ , since the large area  $R_{\text{sc}}^2$  of integration in Eq. (144) is compensated by small value of the normal component in the rarefied core,  $\rho_n \sim \rho(\xi/R_{\text{sc}})$ . That is why if the smooth core is large,  $R_{\text{sc}} \gg \xi$ , this mass is parametrically smaller than the Kopnin mass in Eq. (137).

In conclusion, both contributions to the mass of the vortex result from the mass of the normal component trapped by the vortex. The difference between Kopnin mass and Baym-Chandler backflow mass is only in the origin of the normal component trapped by the vortex. The relative importance of two masses depends on the vortex core structure: (1) For the free continuous vortex with the large core size  $R_{\text{sc}} \gg \xi$ , the Kopnin mass dominates:  $M_{\text{Kopnin}} \sim \rho R_{\text{sc}} \xi \gg M_{\text{BC}} \sim \rho\xi^2$ . (2) For the vortex trapped by the wire of radius  $R_{\text{wc}} \gg \xi$ , the Baym-Chandler mass is proportional to the core area,  $M_{\text{BC}} \sim \rho R_{\text{wc}}^2$ , and is parametrically larger than the Kopnin mass. (3) For the free vortex core with the core radius  $R \sim \xi$  the situation is not clear since the continuous core

approximation does not work any more. But extrapolation of the result in Eq. (144) to  $R \sim \xi$  suggests that the Baym-Chandler mass can be comparable with Kopnin mass.

#### 4. VORTICES IN ${}^3\text{He}$ AND THEIR ANALOGUES IN HIGH ENERGY PHYSICS

Above the critical phase-transition temperature  $T_c$ , liquid  ${}^3\text{He}$  is in its symmetric phase: it has all the symmetries allowed in nonrelativistic condensed matter. The continuous symmetries, whose breaking are relevant for the topological classification of the defects in the non-symmetric phases of  ${}^3\text{He}$ , form the symmetry group

$$\mathbf{G} = SO(3)_{\mathbf{L}} \times SO(3)_{\mathbf{S}} \times U(1)_{\mathbf{N}} \quad . \quad (145)$$

Here  $SO(3)_{\mathbf{L}}$  is the group of solid rotations of coordinate space. The spin rotations of the group  $SO(3)_{\mathbf{S}}$  may be considered as a separate symmetry operations if one neglects the spin-orbital interaction, the magnetic dipole interaction between the nuclear spins which is tiny in comparison with the energies characterizing the superfluid transition. The group  $U(1)_{\mathbf{N}}$  is the *global* symmetry group of gauge transformations, which stems from the conservation of the particle number  $N$  for the  ${}^3\text{He}$  atoms in their ground states.  $U(1)$  is an exact symmetry if one neglects extremely rare processes of the excitations and ionization of the  ${}^3\text{He}$  atoms, as well as the transformation of  ${}^3\text{He}$  nuclei under external radiation.

The broken symmetry states below  $T_c$  are characterized by the order parameter, the  $3 \times 3$  matrix  $\mathbf{A} = A_{\alpha i}$ , which transforms as a vector under a spin rotation for given orbital index ( $i$ ) – and as a vector under an orbital rotation for given spin index ( $\alpha$ ). The transformation of  $A_{\alpha i}$  under the action of the elements of the group  $G$  can be written in the following symbolic form:

$$\mathbf{GA} = e^{2i\tilde{\alpha}} \mathbf{SAL}^{-1} \quad . \quad (146)$$

where  $\tilde{\alpha}$  is the parameter of the *global* gauge transformation;  $\mathbf{S}$  and  $\mathbf{L}$  are matrices of spin and orbital rotations.

There are several models in high energy physics with a similar group  $\mathbf{G}$ , which is broken at low  $T$ :

(i) In the model for the chiral symmetry breaking in QCD the group  $\mathbf{G}$  is the global group (Weinberg 1996)

$$\mathbf{G} = SU(2)_{\mathbf{L}} \times SU(2)_{\mathbf{R}} \times U(1)_A \quad . \quad (147)$$

Here  $SU(2)_{\mathbf{L}}$  and  $SU(2)_{\mathbf{R}}$  are isotopic rotations of the left and right  $u$  and  $d$  quarks correspondingly;  $U(1)_A$  is the anomalous chiral symmetry. Each of these symmetries is approximate and (except for  $U(1)_A$ ) becomes exact in the limit of the zero mass of  $u$  and  $d$  quarks. In some models the groups  $SU(2)_{\mathbf{L}}$  and  $SU(2)_{\mathbf{R}}$  are extended to  $SU(3)_{\mathbf{L}}$  and  $SU(3)_{\mathbf{R}}$ , corresponding to three quark flavours  $u$ ,  $d$  and  $s$ .

(ii) In the dense baryonic matter the symmetry breaking can lead to the color superfluidity of baryons (Ying 1998; Alford et al. 1998; Wilczek 1998a). The starting point for such phase transition can be the group (Wilczek 1998a)

$$\mathbf{G} = SU(3)_{\text{color}} \times SU(3)_{\text{flavour}} \times U(1)_{\mathbf{B}} , \quad (148)$$

where  $SU(3)_{\text{color}}$  is the local group of strong interactions and  $U(1)_{\mathbf{B}}$  corresponds to the conservation of the baryonic charge.

(iii) In one of the Pati-Salam type extensions of the Standard model of the electroweak interactions the group  $\mathbf{G}$  is

$$\mathbf{G} = SU(2)_{\mathbf{L}} \times SU(2)_{\mathbf{R}} \times U(1)_{\mathbf{Y}} . \quad (149)$$

Here  $SU(2)_{\mathbf{L}}$  and  $SU(2)_{\mathbf{R}}$  are the local isotopic rotations and  $U(1)_{\mathbf{Y}}$  is the local  $U(1)$  symmetry which corresponds to the conservation of the hypercharge.

#### 4.1. Vortices in ${}^3\text{He-B}$

##### 4.1.1. Symmetry breaking in ${}^3\text{He-B}$ and analogous phases in high energy physics

Each of the discussed groups  $\mathbf{G}$  contains  $U(1)$  and the product of two similar groups ( $SU(2) \times SU(2)$ ,  $SU(3) \times SU(3)$  or  $SO(3) \times SO(3)$ ). Such group  $\mathbf{G}$  has one interesting symmetry breaking pattern, in which the  $U(1)$  group is broken completely, while the product of two other groups breaks down to the diagonal group. In  ${}^3\text{He}$  such symmetry breaking corresponds to the phase transition into the superfluid B phase, where the spin and orbital momenta are locked together:

$$SO(3)_{\mathbf{L}} \times SO(3)_{\mathbf{S}} \times U(1)_{\mathbf{N}} \rightarrow \mathbf{H}_B = SO(3)_{\mathbf{S+L}} \quad (150)$$

For the triplet  $p$ -pairing, it is the only possible superfluid phase which has an isotropic gap in the quasiparticle spectrum and thus no gap nodes. The order parameter is isotropic: in the simplest realization it has the form

$$A_{\alpha i}^{(0)} = \Delta_B \delta_{\alpha i} . \quad (151)$$

All other degenerate states of the B-phase are obtained by action of the symmetry group  $\mathbf{G}$

$$(\mathbf{G}\mathbf{A}^{(0)})_{\alpha i} = \Delta_B e^{i\Phi} R_{\alpha i} , \quad (152)$$

where  $R_{\alpha i}$  is the real  $3 \times 3$  matrix of 3D rotations;  $\Phi$  is the phase of the superfluid condensate of Cooper pairs, which manifests the breaking of  $U(1)$  group; and  $\Delta_B$  is the magnitude of the order parameter, which determines the gap in the fermionic energy spectrum:

$$\epsilon^2(\mathbf{p}) = v_F^2(p - p_F)^2 + \Delta_B^2 . \quad (153)$$

The  ${}^3\text{He-B}$  has 4 Goldstone bosons, propagating oscillations of  $\Phi$  (sound) and three propagating oscillations of the matrix  $R_{\alpha i}$  (spin waves).

The similar symmetry breaking pattern was discussed by Wilczek (1998a) for the colour superfluidity of the quark condensate in dense baryonic matter:

$$SU(3)_{\text{color}} \times SU(3)_{\text{flavour}} \times U(1)_{\mathbf{B}} \rightarrow SU(3)_{c+f} , \quad (154)$$

Here the color and flavour are locked together similar to spin and orbital momenta in  ${}^3\text{He-B}$ . The breaking of the baryonic  $U(1)_{\mathbf{B}}$  group manifests the superfluidity of the baryonic quark matter.

The analogy between the QCD chiral phase transition and the  ${}^3\text{He-B}$  phase of superfluid  ${}^3\text{He}$  was discussed in the book by Vollhardt and Wölfle (1990), pages 172–173. The symmetry breaking, which is supposed to occur in QCD at  $T_c \sim 100 - 200\text{MeV}$ , is

$$SU(2)_{\mathbf{L}} \times SU(2)_{\mathbf{R}} \times U(1)_{\mathbf{A}} \rightarrow SU(2)_{\mathbf{S+R}} \quad (155)$$

The simplest and general  $2 \times 2$  matrix order parameters of the quark-antiquark chiral condensate are

$$\mathbf{A}^{(0)} = \Delta \tau^0 , \quad (156)$$

$$\mathbf{A} = \mathbf{g}\mathbf{A}^{(0)} = (\sigma\tau^0 + i\vec{\pi} \cdot \vec{\tau}) e^{i\eta} , \quad \sigma^2 + \vec{\pi}^2 = \Delta^2 \quad (157)$$

Here  $\tau^0$  and  $\vec{\tau}$  are the Pauli matrices;  $\Delta$  is the magnitude of the order parameter, which determines the mass of  $u$  and  $d$  quarks; and  $\eta$  is the phase of the chiral condensate. In the hypothetical ideal case, when the initial symmetry  $\mathbf{G}$  is exact, the situation would be similar to  ${}^3\text{He-B}$  with 4 Goldstone bosons:  $\eta$ -mode (analogue of sound) and three pions  $\vec{\pi}$  (analogues of three spin waves).

##### 4.1.2. Mass vortex vs axion string

The homotopy group describing the linear topological defects in  ${}^3\text{He-B}$  is

$$\pi_1(\mathbf{G}/\mathbf{H}_B) = \pi_1(U(1)) + \pi_1(SO(3)) = Z + Z_2 . \quad (158)$$

The group  $Z$  of integers describes the conventional singular vortices with integer winding number  $\nu$  of the phase  $\Phi$  around the vortex core. The simplest realization of such vortices is  $\Phi = \nu\phi$ , where  $\phi$  is an azimuthal angle in the cylindrical coordinate frame. Since  $\mathbf{v}_s = (\hbar/2m_3)\vec{\nabla}\Phi$  is the superfluid velocity of the mass flow, these vortices have circulating mass flow around the core and are called the mass vortices. In the chiral condensate phase they are equivalent to the  $\eta$ -vortices or axion strings discussed by Zhang et al. (1998) and Brandenberger and Zhang (1999).

### 4.1.3. Spin vortex vs pion string

The  $Z_2$  group in  $^3\text{He-B}$  describes the singular spin vortices, with the summation rule  $1 + 1 = 0$  for the topological charge  $\nu$ . The simplest realization of these vortices is

$$R_{\alpha i} = (1 - \cos \theta) \delta_{\alpha i} + \hat{z}_\alpha \hat{z}_i \cos \theta - \varepsilon_{\alpha i k} \hat{z}_k \cos \theta, \quad \theta = \nu \phi. \quad (159)$$

The rule  $1 + 1 = 0$  means that the vortex with  $\nu = 2$  is topologically unstable, i.e. it can be continuously unwound. In the chiral condensate, where the groups  $SU(2)$  substitute the groups  $SO(3)$  of  $^3\text{He}$ , the homotopy group  $\pi_1(\mathbf{G}/\mathbf{H}) = \pi_1(U(1)) = Z$  supports the topological stability only for the phase  $\eta$ -vortices. The pion vortices, with winding of the  $\vec{\pi}$  field around the core, are topologically unstable. The pion strings were discussed by Zhang et al. (1998) and Brandenberger and Zhang (1999): In the simplest realization the order parameter of the pion string is

$$\pi_1 = \pi_2 = 0, \quad \sigma + i\pi_3 = \frac{\Delta(r)}{\sqrt{2}} e^{i\phi} \quad (160)$$

it is equivalent to the (unstable)  $\nu = 2$  spin vortex in  $^3\text{He-B}$ .

### 4.1.4. Spin vortex as domain wall bounded by string

Since each of the  $SO(3)$  subgroups of the group  $\mathbf{G}$  in  $^3\text{He}$  or the  $SU(2)$  ( $SU(3)$ ) chiral symmetries in QCD are approximate, some or all of the Goldstone bosons have a mass. In  $^3\text{He-B}$  the spin-orbital (dipole-dipole) energy explicitly depends on the parameter  $\theta$  in Eq. (159):  $F_D = g_D(\cos \theta + \frac{1}{4})^2$ . Such a ‘‘pion’’ mass of the spin waves essentially modifies the spin vortex: This vortex becomes a termination line for the planar object, which is a stationary soliton in the order parameter field  $R_{\alpha i}$ . All the winding of the angle  $\theta$  around the spin vortex occurs within this soliton, see Fig. 17, bottom. The topologically similar phenomenon of cosmic walls bounded by cosmic strings was discussed by Hindmarsh and Kibble (1995b). In contrast to the mass current vortices, the spin vortex, even if it is topologically stable, i.e. with  $\nu = 1$ , does not appear to be a global minimum energy state in any situation. Nevertheless, it persists as a metastable structure in special circumstances, when it is combined with the mass vortex and forms the spin-mass vortex, see Sec. 2.9.4.

### 4.1.5. Nonaxisymmetric vortex vs Witten superconducting string

The very first measurement in rotation, a cw NMR experiment sensitive to the order parameter texture, re-

vealed as a function of temperature and pressure a first order phase transition with unusual supercooling and superheating properties, which separates two singular mass vortices with the same topology ( $\nu = 1$ ) but different core structures. This discovery illustrated that singular vortices have a complex core structure, unlike in  $^4\text{He-II}$  or conventional s-state superconductors, where the superfluid order parameter distribution goes to zero on approaching the center of the vortex core.

Two stable vortex core structures first have been identified theoretical as two different stationary minimum energy solutions as a function of pressure in the Ginzburg-Landau regime. Both structures have broken parity in the core, but in addition in one of the vortices the axial symmetry is broken in the core, resulting in a dumbbell-like double core structure. The spontaneous breaking of the axial  $U(1)$  symmetry was later verified by observation of the effect of Goldstone mode resulting from such symmetry breaking: the twist of the deformed vortex core, has been excited in NMR experiments (Kondo et al. 1991).

In cosmic strings the analogous breaking of  $U(1)$  symmetry in the core results in the superconducting current along the twisted core (Witten 1985). The instability towards the symmetry breaking in the core can be triggered by fermions living in the core, see Naculich (1995) for cosmic strings and Makhlin and Volovik (1995) for condensed matter vortices.

## 4.2. Vortices in $^3\text{He-A}$

### 4.2.1. Symmetry breaking in $^3\text{He-A}$ and analogous phases in high energy physics

The symmetry breaking pattern, which characterizes the phase transition from the normal liquid  $^3\text{He}$  to the A phase of  $^3\text{He}$ , is

$$\begin{aligned} \mathbf{G} &= SO(3)_{\mathbf{S}} \times SO(3)_{\mathbf{L}} \times U(1)_{\mathbf{N}} \rightarrow \\ \mathbf{H}_A &= SO(2)_{\mathbf{S}_z} \times U(1)_{\mathbf{L}_z - \frac{1}{2}\mathbf{N}} \times Z_2. \end{aligned} \quad (161)$$

The order parameter in the A phase vacuum state is anisotropic both in spin and orbital (coordinate) spaces: in the simplest realization it has the form

$$A_{\alpha i}^{(0)} = \Delta_A \hat{z}_\alpha (\hat{x}_i + i\hat{y}_i). \quad (162)$$

All other degenerate states of the A-phase are obtained by action of the symmetry group  $\mathbf{G}$

$$(\mathbf{G}\mathbf{A}^{(0)})_{\alpha i} = \Delta_A \hat{d}_\alpha (\hat{e}_{1i} + i\hat{e}_{2i}), \quad (163)$$

Here  $\hat{\mathbf{d}}$  is a unit vector of uniaxial anisotropy in spin space;  $\hat{\mathbf{e}}_1$  and  $\hat{\mathbf{e}}_2$  are two mutually orthogonal unit vectors, their vector product  $\hat{\mathbf{e}}_1 \times \hat{\mathbf{e}}_2 = \hat{\mathbf{e}}_3 \equiv \hat{\mathbf{I}}$  determines the uniaxial anisotropy of the liquid in coordinate space.

The symmetry  $\mathbf{H}_A$  of the vacuum state in Eq. (163) contains:

(i) The  $SO(2)_{\mathbf{S}_z}$  subgroup of the  $SO(3)_{\mathbf{S}}$  group: it is the group of spin rotations about axis  $\hat{\mathbf{d}}$ , which does not change the order parameter.

(ii) The diagonal subgroup  $U(1)_{\mathbf{L}_z - \frac{1}{2}\mathbf{N}}$  of the group  $SO(3)_{\mathbf{L}} \times U(1)_{\mathbf{N}}$ : the vacuum state in Eq. (163) is invariant under the orbital rotation  $SO(2)_{\mathbf{L}_z}$  about axis  $\hat{\mathbf{l}}$  if it is accompanied by the proper gauge transformation from  $U(1)_{\mathbf{N}}$  group. A very similar symmetry breaking pattern occurs in the Standard model of the electroweak interactions

$$SU(2)_{\mathbf{T}} \times U(1)_{\mathbf{Y}} \rightarrow U(1)_{\mathbf{T}_3 + \frac{1}{2}\mathbf{Y}}. \quad (164)$$

where  $SU(2)_{\mathbf{T}}$  is the group of the weak isotopic rotations with the generator  $\mathbf{T}$  and  $\mathbf{T}_3 + (1/2)\mathbf{Y}$  is the generator of electric charge.

(iii) The  $Z_2$  is the symmetry of Eq. (163) under combined  $\pi$ -rotations in spin and orbital spaces: rotation of the spin axis,  $\hat{\mathbf{d}}$ , by  $\pi$  about an axis perpendicular to  $\hat{\mathbf{d}}$  followed by rotation of the vectors  $\hat{\mathbf{e}}_1$  and  $\hat{\mathbf{e}}_2$  by  $\pi$  about  $\hat{\mathbf{l}}$  in orbital space.

#### 4.2.2. Chiral fermions

The Bogoliubov-Nambu Hamiltonian for the fermionic excitations of the  ${}^3\text{He-A}$  vacuum is:

$$\mathcal{H}_A = \frac{p^2 - p_F^2}{2m_3} \tilde{\tau}_3 + \frac{\Delta_A}{p_F} (\vec{\sigma} \cdot \hat{\mathbf{d}}) (\tilde{\tau}_1 \hat{\mathbf{e}}_1 \cdot \mathbf{p} - \tilde{\tau}_2 \hat{\mathbf{e}}_2 \cdot \mathbf{p}). \quad (165)$$

Here  $\vec{\sigma}$  and  $\tilde{\tau}_a$  are the Pauli matrices in spin space and in the Bogoliubov-Nambu particle-hole space correspondingly. The square of the Hamiltonian matrix  $\mathcal{H}_A^2 = \epsilon^2(\mathbf{p})$  gives the square of the quasiparticle energy spectrum in Eq. (77).

The quasiparticle spectrum in Eq. (165) has two point zeroes in momentum space (point nodes): at  $\mathbf{p} = ep_F \hat{\mathbf{l}}$  ( $e = \pm 1$ ). These nodes are the source of chiral anomaly in  ${}^3\text{He-A}$ , since in the vicinity of each zero the spectrum of the fermions is that of the Weyl chiral relativistic fermions. For a given spin projection  $\vec{\sigma}$ , the Hamiltonian matrix near the nodes is

$$\mathcal{H} = -e \sum_a c_a \tilde{\tau}^a \hat{e}_a^i (p_i - eA_i), \quad (166)$$

where  $A_i = p_F \hat{l}_i$  is the vector potential of the effective electromagnetic field; and ‘‘speeds of light’’, the slopes in the linear spectrum of fermionic quasiparticles, are  $c_3 \equiv c_{\parallel} = v_F$ ,  $c_1 = c_2 \equiv c_{\perp} = \Delta_A/p_F$ . The square of this Hamiltonian matrix leads (after the Doppler shift is included) to Eq. (78) for the relativistic massless particle

moving in electromagnetic and gravity fields. The gravitational metric tensor in Eqs. (78,79) is determined by the dreibein  $(\hat{\mathbf{e}}_1, \hat{\mathbf{e}}_2, \hat{\mathbf{e}}_3 \equiv \hat{\mathbf{l}})$  in a usual manner:

$$g^{ik} = \sum_{a=1}^3 c_a^2 \hat{e}_a^i \hat{e}_a^k, \quad (167)$$

In high energy physics there are several systems with (3+1)-dimensional chiral fermions as the low energy excitations:

(i) In the Standard Model all the fermions (quarks and leptons) are chiral in the symmetric phase above the electroweak transition.

(ii) The  $\beta$ -phase of ‘‘color superfluid’’ quark condensate in a dense baryonic matter also contains the gap node at shifted momentum  $\mathbf{p} = \vec{\phi} \neq 0$  in the quark energy spectrum, where  $\vec{\phi}$  is the order parameter of quark superfluid (Ying 1998). Close to this node the low-energy fermions are chiral.

#### 4.2.3. Topological classification

The electroweak model does not support topologically stable strings. The fundamental homotopy group of the electroweak vacuum manifold

$$(SO(3)_{\mathbf{T}} \times U(1)_{\mathbf{Y}}) / U(1)_{\mathbf{T}_3 + \frac{1}{2}\mathbf{Y}} = SU(2). \quad (168)$$

is trivial:  $\pi_1 = 0$ . In contrast, the A-phase manifold has nontrivial fundamental group

$$\pi_1(\mathbf{G}/\mathbf{H}_A) = \pi_1((SO(3) \times S^2)/Z_2) = Z_4. \quad (169)$$

which contains four elements. This means that there are 4 topologically distinct classes of strings in  ${}^3\text{He-A}$ . Each can be described by the topological charge  $\nu$  which takes only 4 values, which we choose to be 0,  $\pm 1/2$  and 1 with summation modulo 2 (ie.  $1+1=0$ ).

The simplest realization of the linear defect with an integer charge  $\nu$  is a vortex with integer winding number  $\nu$ . Such vortices have the following structure outside the core

$$A_{\alpha i} = \Delta_A \hat{z}_{\alpha} (\hat{e}_1^i + i\hat{e}_2^i), \quad \hat{\mathbf{e}}_1 + i\hat{\mathbf{e}}_2 = e^{i\nu\phi} (\hat{\mathbf{x}} + i\hat{\mathbf{y}}). \quad (170)$$

with quantized circulation  $\oint d\mathbf{r} \cdot \mathbf{v}_s = \kappa\nu$ , where the superfluid velocity is  $\mathbf{v}_s = (\kappa/2\pi) \hat{e}_1^i \vec{\nabla} \hat{e}_2^i$  and the circulation quantum is  $\kappa = \pi\hbar/m_3$ .

#### 4.2.4. Z and W strings

As in the B phase, the vortex with phase winding  $\nu = 2$  (as well as with other even  $\nu$ ) is topologically unstable

and can be continuously unwound. The topologically unstable  $\nu = 2$  vortex in Eq. (170) corresponds to the unit winding  $Z$ -string in the Standard electroweak model, while another realization of the topologically unstable defect

$$A_{\alpha i} = \Delta_A \hat{z}_\alpha (\hat{z}_i + i(\hat{x}_i \cos 2\phi + \hat{y}_i \sin 2\phi)) \quad (171)$$

corresponds to the  $W$ -string solution (Volovik and Vachaspati 1996).

#### 4.2.5. Alice string – half-quantum vortex

The asymptotic form of the order parameter in vortices with fractional circulation number  $\nu = \pm 1/2$  (or, simply, half-quantum vortices) is given by

$$A_{\alpha j} = \Delta_A e^{\pm i\phi/2} \hat{d}_\alpha (\hat{x}_j + i\hat{y}_j) , \quad (172)$$

where

$$\hat{\mathbf{d}} = \hat{\mathbf{x}} \cos \frac{\phi}{2} + \hat{\mathbf{y}} \sin \frac{\phi}{2}. \quad (173)$$

On circumnavigating such a vortex, the change of the sign of the order parameter due to the phase winding by  $\pi$ , is compensated by the change of sign of the vector  $\hat{\mathbf{d}}$ . So, it is the  $\nu = 1/2$  mass vortex topologically confined with  $\nu = 1/2$  spin vortex. As in  $^3\text{He-B}$ , such spin-mass vortex is the termination line of the topological  $Z_2$ -solitons. This property allows identification of this object in future experiments.

The  $\nu = 1/2$  vortex is the counterpart of Alice strings considered in particle physics (Schwarz 1982): a particle that goes around an Alice string flips its charge. In  $^3\text{He-A}$  the quasiparticle going around a  $1/2$  vortex flips its  $U(1)_{\mathbf{S}_3}$  charge, that is, its spin. As a consequence, several phenomena (e.g. global Aharonov-Bohm effect) discussed in the particle physics literature have corresponding discussions in the condensed matter literature (see Khazan (1985), Salomaa and Volovik (1987) for  $^3\text{He-A}$  and March-Russel et al. (1992), Davis and Martin (1994) in particle physics). Note that in  $^3\text{He-A}$  also the particle-like topological object, the hedgehog, flips its  $\pi_2$  topological charge around the  $1/2$  vortex (Volovik and Mineev 1977).

The vortex with  $\nu = 1/2$  was predicted to exist in superconductors with  $d$ -wave pairing by Geshkenbein et al. (1987). It has been observed in high-temperature superconductors by Kirtley et al. (1996). As in superfluid  $^3\text{He}$ , this fractional vortex is topologically connected with the wall defect: it is attached to the tricrystal line, which is the junction of three grain boundaries (Geshkenbein et al. 1987; Kirtley et al. 1996). Such vortex can also exist without grain boundaries if it is attached to the linear topological defect of the crystal lattice – disclination.

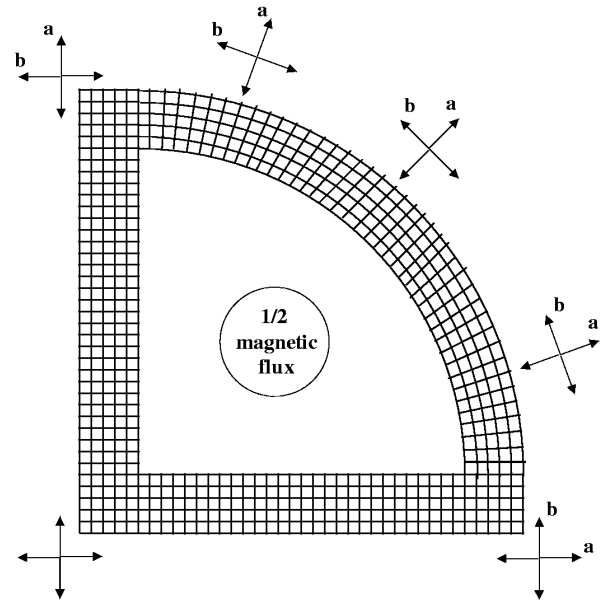


FIG. 33. Structure of the  $\nu = 1/2$  vortex in the loop of the tetragonal crystal with  $d$ -wave pairing. The loop contains  $1/2$  of the quantum of magnetic flux.

Fig. 33 illustrates such example for the  $d$ -wave superconductivity in the tetragonal crystal. The  $d$ -wave order parameter in the depicted crystal loop is

$$A_{ik} = \Delta e^{2i\phi} (a_i a_k - b_i b_k) , \quad (174)$$

$$\mathbf{a} = \hat{\mathbf{x}} \cos \phi + \hat{\mathbf{y}} \sin \phi , \quad \mathbf{b} = \hat{\mathbf{y}} \cos \phi - \hat{\mathbf{x}} \sin \phi . \quad (175)$$

When circumnavigating a crystal loop the angle  $\phi$  changes from 0 to  $\pi/2$ . The change of the sign of the order parameter due to the change of the phase is compensated by transformation of the axis  $\mathbf{a}$  to the axis  $\mathbf{b}$ . The empty space inside the loop thus represents the common core of the  $\nu = 1/2$  vortex and disclination.

This  $\nu = 1/2$  vortex carries  $1/2$  of the magnetic flux quantum  $\Phi_0 = h/2e$ , the same as was measured for the vortex attached to the tricrystal line (Kirtley et al. 1996). In principle the flux number does not necessarily coincide with the winding number  $\nu$ , thus the objects with the fractional flux below  $\Phi_0/2$  are also possible (Volovik and Gor'kov 1984). They can arise if the time inversion symmetry is broken (Sigrist et al. 1989, 1995).

In  $^3\text{He-B}$  the experimentally identified non-axisymmetric  $\nu = 1$  vortex (Kondo et al. 1991) can be considered as a pair of  $1/2$  vortices, connected by the nontopological wall (Thuneberg 1986; Salomaa and Volovik 1987; Salomaa and Volovik 1989; Volovik 1990).

#### 4.2.6. Torsion string

The  $\nu = 1$  class of the linear topological defects in  ${}^3\text{He-A}$  contains different objects, which have analogies in strings in high energy physics and gravity. Let us start with  $\nu = -1$  vortex in Eq. (170)

$$A_{\alpha i} = \Delta_A \hat{z}_\alpha (\hat{e}_1^i + i\hat{e}_2^i), \quad \hat{e}_1 = \hat{\mathbf{r}}, \quad \hat{e}_2 = \hat{\phi}. \quad (176)$$

If the fully “relativistic” quasiparticle Hamiltonian  $\mathcal{H}$  in Eq. (166) is considered, then the metric in Eq. (167) produced by this dreibein is completely flat outside the vortex core:  $g^{ik} = c_{\parallel}^2 \hat{z}^i \hat{z}^k + c_{\perp}^2 (\delta^{ik} - \hat{z}^i \hat{z}^k)$ . However the dreibein itself has a topologically nontrivial winding about the vortex and becomes zero on the vortex axis. Such vortex is analogous to the torsion defects discussed in the gravity theory (Hanson and Regge 1978; d’Auria and Regge 1982), where they play the same part as Abrikosov vortices in superconductors. The transformation  $\mathcal{H} \rightarrow e^{-i\tilde{\tau}_3 \phi/2} \mathcal{H} e^{i\tilde{\tau}_3 \phi/2}$  eliminates the winding of the dreibein around the torsion string. However the new wave functions  $\Psi \rightarrow e^{-i\tilde{\tau}_3 \phi/2} \Psi$  change sign after rotation around the string.

#### 4.2.7. Spinning string

Let us now take into account the initial nonrelativistic Hamiltonian for the general quasiparticle in Eq. (165). Then the transformation  $\mathcal{H} \rightarrow e^{-i\tilde{\tau}_3 \phi/2} \mathcal{H} e^{i\tilde{\tau}_3 \phi/2}$ , which eliminates the winding of the dreibein, produces the Doppler shift in the quasiparticle spectrum due to the superfluid velocity  $\mathbf{v}_s = -(\kappa/2\pi r)\hat{\phi}$  circulating around the vortex:  $\mathcal{H} \rightarrow \mathcal{H} + \mathbf{p} \cdot \mathbf{v}_s$ . In the “relativistic” limit close to the gap nodes this leads to Eq. (78) for the particle in gravitational field, which metric in Eq. (79) contains the element  $g^{0i} = -v_s^i$ . Let us recall that in the gravity theory the element  $\mathbf{g} = -g^{0i}$  plays the part of the vector potential of the gravimagnetic field  $\mathbf{B}_g = \vec{\nabla} \times \mathbf{g}$ . In the case of  ${}^3\text{He-A}$  this field  $\mathbf{B}_g = \vec{\nabla} \times \mathbf{v}_s = \kappa\nu\delta_2(\mathbf{r})$  is concentrated on the vortex axis as in the case of the cosmic spinning string. That is why the vortex serves as an analogue of the spinning cosmic string. It represents the Aharonov-Bohm tube with the gravimagnetic field. The scattering of quasiparticles on this tube due to the gravitational analogue of the Aharonov-Bohm effect leads to Iordanskii force acting on the vortex from the quasiparticles, as was discussed in Sec. 3.2.

#### 4.2.8. Disgyration as negative-mass string

The  $\nu = 1$  class of the topologically stable defects also contains disgyrations – singularities in the  $\hat{\mathbf{l}}$  vector field. The simplest ones are the radial disgyration, with the radial distribution of  $\hat{\mathbf{l}}$ :

$$\hat{e}_1 = \hat{\phi}, \quad \hat{e}_2 = \hat{\mathbf{z}}, \quad \hat{\mathbf{l}} = \hat{\mathbf{r}}, \quad (177)$$

and the axial disgyration, with the axial  $\hat{\mathbf{l}}$ :

$$\hat{e}_1 = \hat{\mathbf{z}}, \quad \hat{e}_2 = \hat{\mathbf{r}}, \quad \hat{\mathbf{l}} = \hat{\phi}. \quad (178)$$

The effective metric for the quasiparticles moving outside the core

$$g^{ik}(\text{radial}) = c_{\parallel}^2 \hat{r}^i \hat{r}^k + c_{\perp}^2 (\delta^{ik} - \hat{r}^i \hat{r}^k), \quad (179)$$

$$g^{ik}(\text{axial}) = c_{\parallel}^2 \hat{\phi}^i \hat{\phi}^k + c_{\perp}^2 (\delta^{ik} - \hat{\phi}^i \hat{\phi}^k). \quad (180)$$

The interval of the effective space corresponding to the inverse metric  $g_{ik}$  is

$$ds^2(\text{radial}) = dt^2 - \frac{1}{c_{\perp}^2} dz^2 - \frac{1}{c_{\parallel}^2} \left( dr^2 + \frac{c_{\parallel}^2}{c_{\perp}^2} r^2 d\phi^2 \right), \quad (181)$$

$$ds^2(\text{axial}) = dt^2 - \frac{1}{c_{\perp}^2} dz^2 - \frac{1}{c_{\parallel}^2} \left( dr^2 + \frac{c_{\perp}^2}{c_{\parallel}^2} r^2 d\phi^2 \right). \quad (182)$$

The space outside the core is flat, but the proper length of the circumference of radius  $r$  around the axis is  $2\pi r(c_{\parallel}/c_{\perp})$  for the radial disgyration, which is much larger than  $2\pi r$ , and  $2\pi r(c_{\perp}/c_{\parallel})$  for the axial disgyration, which is much smaller than  $2\pi r$ . This the so-called conical singularity gives rise to the Riemann curvature concentrated at the axis of disgyration ( $r = 0$ ) (Sokolov and Starobinsky 1977; Banados et al. 1992):

$$\mathcal{R}_{r\phi}^{r\phi}(\text{radial}) = 2\pi \left( 1 - \frac{c_{\perp}}{c_{\parallel}} \right) \delta_2(\mathbf{r}), \quad (183)$$

$$\mathcal{R}_{r\phi}^{r\phi}(\text{axial}) = 2\pi \left( 1 - \frac{c_{\parallel}}{c_{\perp}} \right) \delta_2(\mathbf{r}). \quad (184)$$

The conical singularity is the property of any massive local string in high energy physics. The curvature in Eq. (184) corresponds to a supermassive string, while that in Eq. (183) can come only from the string with the negative mass.

The real defect within the topological class  $\nu = 1$ , which is measured in  ${}^3\text{He-A}$  at finite temperature and finite magnetic fields, is the object, which represents the vortex at large distance from the core, but continuously transforms to the disgyration when the core is approached (Fig. 34). Such a continuous change of the order parameter allows us to identify this vortex in NMR experiments (see Fig. 35 with NMR signals from different vortices).

#### 4.2.9. Continuous vortices — textures

Singular vortices with even circulation number,  $\nu = 2k$ , belong to the class  $\nu = 0$ . They are topologically unstable and can be continuously dissolved, which means

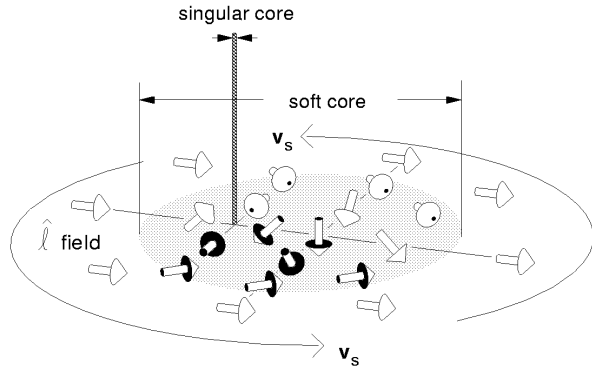


FIG. 34. Structure of the  $\nu = 1$  vortex in  ${}^3\text{He-A}$  at finite  $T$  and finite magnetic field appropriate for NMR experiments. Outside of the soft core this object is a pure  $\nu = 1$  vortex. Close to the hard core it transforms to disgyration in the  $\hat{\mathbf{d}}$  field, which belongs to the same topological class  $\nu = 1$ .

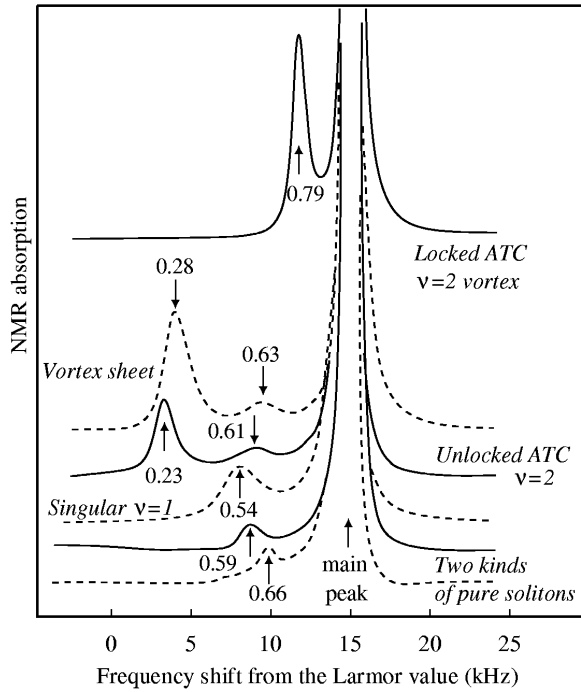


FIG. 35. NMR signature of different topological objects in rotating  ${}^3\text{He-A}$ . Each kind of vortices and solitons gives rise to a characteristic satellite peak in the  ${}^3\text{He}$  NMR absorption spectrum. The height of the peak corresponding to a given type of vortex is directly proportional to the number of such vortices in the cell. The height of the soliton and vortex sheet peaks is proportional to the surface area of the corresponding solitons. Unlocked and locked ATC  $\nu = 2$  vortices have the same topology of the  $\hat{\mathbf{d}}$  texture, but different topology of the  $\hat{\mathbf{l}}$  texture.

that the singularity on the vortex axis can be continuously removed. What is left is called “texture” – the continuously distributed (non-singular) order parameter

within the vacuum manifold. Textures are characterized by continuous vorticity (Mermin and Ho 1976; Ho 1978), which plays the part of the gravimagnetic field  $\mathbf{B}_g$ :

$$\mathbf{B}_g = \vec{\nabla} \times \mathbf{v}_s = \frac{\hbar}{4m_3} \varepsilon_{ijk} \hat{l}_i \vec{\nabla}_j \hat{l}_k \times \vec{\nabla} \hat{l}_k. \quad (185)$$

If the order parameter is fixed at infinity, the final stage of the initially singular  $\nu = \pm 2$  vortex is the continuous doubly quantized vortex, example of which is the Anderson-Toulouse-Chechetkin vortex in Fig. 27. In a modified form two topologically different vortices of this type have been observed in NMR experiments (see Fig. 35). In the particle physics literature, the analog of Anderson-Toulouse-Chechetkin vortex is known as Preskill’s semicolored skyrmion (Preskill 1992).

#### 4.2.10. Vortex sheet

Symmetry-breaking phase transitions in superfluid  ${}^3\text{He}$  give many example of the confinement of one object to another of higher dimensionality. Such topological confinement can be divided into three types. (i) An object may serve as a boundary for a higher dimensional object. An example of this is an observed soliton terminating on spin-mass vortex in  ${}^3\text{He-B}$  (Sec. 2.9.4). (ii) An object has an end on a higher dimensional object. We shall discuss this example in Sec. 4.2.11. (iii) An object may exist only within another object, from where it cannot escape to the world outside. A well-known example of the latter type is a Bloch line within a domain wall in ferromagnets (Chen 1977; Dedukh et al. 1985; Nikiforov and Sonin 1983). The latter kind of confinement was observed in rotating  ${}^3\text{He-A}$  and represents the vortex sheet (Parts et al. 1994; Heinilä and Volovik 1995). The higher dimensional object in this configuration is a topologically stable domain wall, called soliton. The corresponding one dimensional object is a specific type of quantized vortex line, which exists only within the soliton. A soliton with an array of such vortices forms a vortex sheet.

Historically, vorticity concentrated in sheets was suggested by Onsager (1954) and London (1946) to describe the superfluid state of  ${}^4\text{He}$  under rotation. It turned out, however, that a vortex sheet is unstable towards break-up into separate quantized vortex lines in  ${}^4\text{He}$ . Nevertheless, a later calculation of the spacing between vortex sheets by Landau and Lifshitz (1955), who did not impose a quantization requirement on the sheets, happens to be exactly to the point for the vortex sheet in  ${}^3\text{He-A}$ .

In  ${}^3\text{He-A}$  the vortex sheet is topologically stable, because its base is represented by the topologically stable soliton: a surface separating domains having parallel and antiparallel orientations of  $\hat{\mathbf{l}}$  and  $\hat{\mathbf{d}}$  vectors (Fig. 36). The core of the soliton has a smooth bending of  $\hat{\mathbf{l}}$ , so that within the soliton there are two degenerate states, which

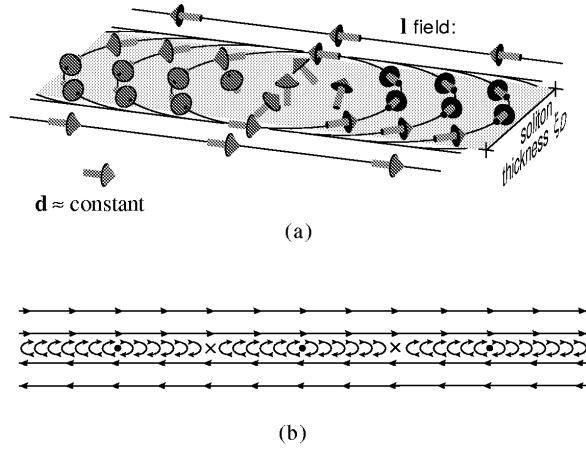


FIG. 36. Vortex sheet in  ${}^3\text{He-A}$ . (a) Topologically stable soliton, a surface separating domains having parallel and antiparallel orientations of  $\hat{\mathbf{I}}$  and  $\hat{\mathbf{d}}$  vectors, has two degenerate states, which can be obtained from each other by a symmetry operation. The degeneracy gives rise to a topological object, a kink, separating two states. The kink has no singularity in the  $\hat{\mathbf{I}}$  field and has nonzero vorticity, corresponding to continuous  $\nu = 1$  vortex. (b) Vortex sheet, the chain of these  $\nu = 1$  vortex kinks, which can live only within the soliton, is formed in the rotating vessel under special conditions.

can be obtained from each other by a symmetry operation. The degeneracy gives rise to a topological object, a kink, separating two states. The kink has no singularity in the  $\hat{\mathbf{I}}$  field and is equivalent to the Bloch line. According the Mermin-Ho relation Eq. (185) the core of the “Bloch line” has nonzero vorticity, so that it represents the continuous  $\nu = 1$  vortex. It is important that outside the soliton the  $\nu = 1$  vortices are singular. That is why the continuous  $\nu = 1$  vortices can live only within the soliton and cannot escape from the soliton.

The similar effect of vortices topologically confined in the domain walls has been discussed for unconventional superconductors ( ; Shung et al. 1998; Kita 1999). Each trapped vortex has the fractional flux and thus can live only within the wall.

#### 4.2.11. Strings terminating on walls

The linear defect living within the wall defect is only one of numerous examples of the topological connections between defects of different dimensionalities observed and to be observed in superfluid  ${}^3\text{He}$ . The topological classification of such connections has been discussed by Trebin and Kutka (1995), Misirpashaev (1991), and Volovik (1992a). Among them – classification of strings terminating on walls and point defects confined to the walls (boojums); topological constraints on the crossing the wall by point and line defects, etc. An experimental evidence of the B-phase  $\nu = 1$  vortex line terminating on

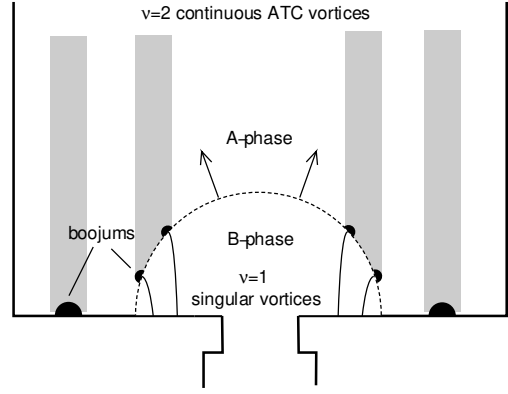


FIG. 37. B-phase  $\nu = 1$  vortices terminating on the growing interface between A and B phases in rotating superfluid  ${}^3\text{He}$ . The end point of the  $\nu = 1$  vortex is the point defect, which resembles the gravimagnetic monopole, whose Dirac string is the B-phase vortex.

the phase boundary between B phase and A-phase has been found in rotating  ${}^3\text{He}$  (Krusius et al. 1994), Fig. 37. In high energy physics such configurations, which have got the name “Dirichlet topological defects” (Carroll and Trodden 1998), were discussed for QCD theory: a QCD string emanating from a quark can end on an axionic domain wall (Campos et al. 1998).

#### 4.2.12. Gravimagnetic monopole

In the special case of a vortex crossing A-B phase boundary the end point of the  $\nu = 1$  vortex line, the boojum, resembles the gravimagnetic monopole discussed by Lynden-Bell and Nouri-Zonoz (1998): On the A-phase side the  $\hat{\mathbf{I}}$  vector, the superfluid velocity  $\mathbf{v}_s$  and its vorticity  $\mathbf{B}_g$ , which plays the part of the gravimagnetic field, are

$$\hat{\mathbf{I}} = \hat{\mathbf{r}}, \quad \mathbf{v}_s = \frac{\hbar}{2m_3} \frac{1 - \cos\theta}{r \sin\theta} \hat{\phi}, \quad \mathbf{B}_g = \vec{\nabla} \times \mathbf{v}_s = \frac{\hbar}{2m_3} \frac{\mathbf{r}}{r^3}. \quad (186)$$

Here  $r, \theta, \phi$  are spherical coordinates. On the B-phase side one has

$$\mathbf{B}_g = \vec{\nabla} \times \mathbf{v}_s = \frac{\pi\hbar}{m_3} \delta_2(\mathbf{r}). \quad (187)$$

Expressions in Eqs. (186,187) are simple model which only reproduces topology of relevant fields. Thus the vorticity  $\mathbf{B}_g$  (analog of gravimagnetic flux), which propagates along the vortex in the B phase towards the end point (boojum) propagates radially and divergenceless from the boojum into the A phase. So, the B phase  $\nu = 1$  vortex plays the part of Dirac string.

The analogues of gravimagnetic monopoles can appear in  ${}^3\text{He-A}$  also when the topologically unstable singular  $\nu = 2$  vortex breaks. In a similar manner the  $Z$ -string in the Standard model breaks into pieces terminating on pairs of magnetic monopoles and antimonopoles.

## 5. CONCLUSION

The quantum physical vacuum – the former empty space – is in a reality a richly structured and asymmetric medium. Because this new quantum ether is complicated material with many degrees of freedom, one can learn how to analyze it by studying other such materials – condensed matter (Wilczek 1998b). Fermi superfluids, especially  ${}^3\text{He-A}$ , are the best condensed matter, which provide a rich source for such a modelling. The most pronounced property of  ${}^3\text{He-A}$  is that in addition to the numerous bosonic fields (collective modes of the order parameter which play the part of the gauge fields in electromagnetic, weak and strong interactions) it contains gapless fermionic quasiparticles, which are similar to the elementary excitations of quantum physical vacuum (leptons and quarks).

It is important that the quantum physical vacuum belongs to the same class of the fermionic condensed matter as  ${}^3\text{He-A}$ : both contain the topologically stable nodes in the energy spectrum of the fermionic excitations. As a result both fermionic systems display, for example, the gravitational and gauge fields as the collective bosonic modes of the fermionic system. The other fermionic systems belong either to the class, which is characterized by the Fermi surfaces (such as normal metals and normal Fermi liquid), or to the class with the gap in the fermionic spectrum (such as conventional superconductors and  ${}^3\text{He-B}$ ), while the high-temperature superconductors belong to the marginal class with the topologically unstable lines of gap nodes. Thus  ${}^3\text{He-A}$  (together with  ${}^3\text{He-A}_1$ ) remains the only condensed matter frame in which the properties of the physical vacuum can be fully probed, even with laboratory experiments.

Zeroes in the fermionic spectrum, such as Fermi surfaces (surfaces of zeroes) and Fermi points (point zeroes) play an extremely important role in the low-energy physics of the quantum vacuum and condensed matter. In condensed matter, the gapless fermions interacting with the Bose fields of the order parameter lead to the anomalous behavior of superfluids and superconductors at low temperature,  $T \ll T_c$ , such as spectral flow in the vortex dynamics, non-analytic behavior of the current and gradient energy, nonlinear and nonlocal Meissner effect, etc. The counterpart of this behavior in high energy physics manifests itself in the axial anomaly, baryogenesis, zero charge effect, running coupling constants, photon mass, etc. It is the zeroes in the fermionic spectrum,

through which the conversion of the vacuum degrees of freedom into that of the matter takes place.

Similar zeroes, but in the real space, occur in the cores of the topological defects, among which the quantized vortices (cosmic strings in the high energy physics) play an important role. Actually the real-space zeroes and the momentum-space zeroes are described by the same topology extended to the  $8=4+4$ -dimensional space. For example, from the topological point of view the Fermi surface represents the vortex singularity of the Green's function in the  $\omega, \mathbf{p}$  space, where  $\omega$  is the Matsubara frequency. The Green's function  $G(\omega, p) = 1/(i\omega + v_F(p - p_F))$  displays a vortex in the  $\omega, p$  plane with the winding number  $\nu = 1$ . This makes the Fermi surface topologically stable and robust under perturbations of the Fermi system. Even though the pole in the Green's function can disappear under some perturbations, the Fermi surface will survive in the marginal and Luttinger superfluids. The latter thus belong to the same class of the Fermi systems as the Landau Fermi-liquid.

In the same manner the gapped superfluids and superconductors behave in the vicinity of the vortex core as superfluid  ${}^3\text{He-A}$  in bulk. The point gap nodes appear to be the common feature. Due to the common topological origin of point nodes, the fermions near the gap nodes in gapless Fermi superfluids and superconductors and the low energy fermions localized in cores of vortices in conventional gapped superconductors produce similar anomalous effects.

The vortices play an important part not only at low temperature, but also in the physics of the broken symmetry phase transitions. The proliferation of vortex loops with infinite size destroys the superfluid long range order above the phase transition. In the nonequilibrium phase transition from the symmetric nonsuperfluid phase, discussed here, the infinite vortex cluster in the normal state survives after the rapid quench and becomes the origin of the remanent vorticity in the superfluid state. We believe that it is this mechanism, which leads to the observed vorticity in our experiments with neutrons.

## ACKNOWLEDGEMENTS

We would like to dedicate this work to our godfathers Tom Kibble and Wojciech Zurek. We are indebted to Yu. Bunkov, A. Gill, H. Godfrin, H.E. Hall, J.R. Hook, T. Jacobson, N. Kopnin, A. Leggett, Yu. Makhlin, P. Mazur, B. Plaçaïs, J. Ruohio, V. Ruutu, E. Thuneberg, T. Vachaspati, G. Williams, Wen Xu, and X. Zhang. Much of the cowork with these colleagues was made possible by a grant from the EU Human Capital and Mobility visitor program (no. CHGECT94-0069). The collaboration has been inspired by the European Science Foundation network on "Topological Defects in Cosmology and Condensed Matter Physics".

## REFERENCES

- Aarts, R.G.K.M and A.T.A.M de Waele, 1994, *Phys. Rev. B* **50**, 10069.
- Adams, J.S., S.R. Bandler, S.M. Brouer, R.E. Lanou, H.J. Maris, T. More and G.M. Seidel, 1995, *Phys. Lett. B* **341**, 431.
- Adler, S., 1969, *Phys. Rev.* **177**, 2426.
- Aharonov, Y. and D. Bohm, 1959, *Phys. Rev.* **115**, 485.
- Albert, D.Z., 1982, *Phys. Rev. B* **25**, 4810.
- Alford, M., K. Rajagopal and F. Wilczek, 1998, *Phys. Lett. B* **422**, 247.
- Amelino-Camelia, G., J.D. Bjorken and S.E. Larsson, 1997, *Phys. Rev. D* **56**, 6942.
- Antunes, N.D., L.M.A. Bettencourt and M. Hindmarsh, 1998, *Phys. Rev. Lett.* **80**, 908.
- Antunes, N.D., L.M.A. Bettencourt and W.H. Zurek, 1999, *Phys. Rev. Lett.* **82**, 2824.
- Antunes, N.D. and L.M.A. Bettencourt, 1998, *Phys. Rev. Lett.* **81**, 3083.
- Aranson, I.S., N.B. Kopnin and V.M. Vinokur, 1999, *Phys. Rev. Lett.* **83**, 2600.
- Awschalom, D.D. and K.W. Schwarz, 1984, *Phys. Rev. Lett.* **52**, 49.
- Banados, M., C. Teitelboim and J. Zanelli, 1992, *Phys. Rev. Lett.* **69**, 1849.
- Barenghi, C.F., D.C. Samuels, G.H. Bauer and R.J. Donnelly, 1997, *Phys. Fluids* **9**, 2631.
- Barriola, M., 1995, *Phys. Rev. D* **51**, 300.
- Bäuerle, C., Yu.M. Bunkov, S.N. Fisher, H. Godfrin and G.R. Pickett, 1996, *Nature* **382**, 332.
- Bäuerle, C., Yu.M. Bunkov, S.N. Fisher, H. Godfrin and G.R. Pickett, 1998a, *J. Low Temp. Phys.* **110**, 13.
- Bäuerle, C., Yu.M. Bunkov, S.N. Fisher and H. Godfrin, 1998b, *Phys. Rev. B* **57**, 14381.
- Baym, G. and E. Chandler, 1983, *J. Low Temp. Phys.* **50**, 57.
- Bell, J.S. and R. Jackiw, 1969, *Nuovo Cim. A* **60**, 47.
- Bevan, T.D.C., A.J. Manninen, J.B. Cook, A.J. Armstrong, J.R. Hook and H.E. Hall, 1995, *Phys. Rev. Lett.* **74**, 750.
- Bevan, T.D.C., A.J. Manninen, J.B. Cook, J.R. Hook, H.E. Hall, T. Vachaspati and G.E. Volovik, 1997a, *Nature* **386**, 689.
- Bevan, T.D.C., A.J. Manninen, J.B. Cook, H. Alles, J.R. Hook and H.E. Hall, 1997b, *J. Low Temp. Phys.* **109**, 423.
- Bjorken, J.D., 1997, *Acta Phys. Polon. B* **28**, 2773.
- Bowick, M.J., L. Chandar, E.A. Schiff and A.M. Srivastava, 1994, *Science* **263**, 943.
- Bradley, D.I., S.N. Fisher and W.M. Hayes, 1998, *J. Low Temp. Phys.* **113**, 687.
- Brandenberger, R.H. and X. Zhang, 1999, *Phys. Rev. D* **59**, 081301.
- Bray, A., 1994, *Adv. Phys.* **43**, 357.
- Bunkov, Yu.M. and O.D. Timofeevskaya, 1998a, *Phys. Rev. Lett.* **80**, 4927.
- Bunkov, Yu.M. and O.D. Timofeevskaya, 1998b, *J. Low Temp. Phys.* **110**, 45.
- Campos, A., K. Holland and U.-J. Wisse, 1998, *Phys. Rev. Lett.* **81**, 2420.
- Carmi, R., E. Polturak and G. Koren, 2000, *Phys. Rev. Lett.* **84**, 4966.
- Caroli, C., P.G. de Gennes and J. Matricon, 1964, *Phys. Lett.* **9**, 307.
- Carroll, S.M. and M. Trodden, 1998, *Phys. Rev. D* **57**, 5189.
- Chattopadhyay, B., M.C. Mahato and S.R. Shenoy, 1993, *Phys. Rev. B* **47**, 15159.
- Chen, Chih-Wen, 1977, *Magnetism and Metallurgy of Soft Magnetic Materials* (North-Holland, Amsterdam).
- Chuang, I., R. Durrer, N. Turok and B. Yurke, 1991, *Science* **251**, 1336.
- Cleary, R.M., 1968, *Phys. Rev.* **175**, 587.
- d'Auria, R. and T. Regge, 1982, *Nucl. Phys. B* **195**, 308.
- Davis, A.C. and A.P. Martin, 1994, *Nucl. Phys. B* **419**, 341.
- Davis, R.L., 1992, *Physica B* **178**, 76.
- Davis, R.L. and E.P.S. Shellard, 1989, *Phys. Rev. Lett.* **63**, 2021.
- Dedukh, L.M., B.I. Nikitenko and E.B. Sonin, 1985, *Uspekhi Fiz. Nauk* **145**, 158; [*Sov. Phys. – Uspekhi* **28**, 100 (1985)].
- Demircan, E., P. Ao and Q. Niu, 1995, *Phys. Rev. B* **52**, 476.
- Deser, S., R. Jackiw and G. 't Hooft, 1984, *Ann. Phys.* **152**, 220.
- Dodd, M.E., P.C. Hendry, N.S. Lawson, P.V.E. McClintock and C.D.H. Williams, 1998, *Phys. Rev. Lett.* **81**, 3703.
- Donnelly, R.J., 1991, *Quantized Vortices in Helium II* (Cambridge University Press, Cambridge, UK).
- Duan, J.M., 1995, *Phys. Rev. Lett.* **75**, 974.
- Dziarmaga, J., 1998, *Phys. Rev. Lett.* **81**, 1551.
- Dziarmaga, J., 1999, *Phys. Rev. Lett.* **82**, 4749.
- Einasto, J., M. Einasto, S. Gottlöber, V. Müller, V. Saar, A.A. Starobinsky, E. Tago, D. Tucker, H. Andernach and P. Frisch, 1997, *Nature* **385**, 139.
- Eltsov, V.B., A.Ya. Parshin and I.A. Todoshchenko, 1998, *J. Low Temp. Phys.* **113**, 525.
- Fetter, A.L., 1964, *Phys. Rev.* **136A**, 1488.
- Gal'tsov, D.V. and P.S. Letelier, 1993, *Phys. Rev. D* **47**, 4273.
- Garriga, J. and T. Vachaspati, 1995, *Nucl. Phys. B* **438**, 161.
- Geller, M.J. and J.P. Huchra, 1989, *Science* **246**, 897.
- Geshkenbein, V., A. Larkin and A. Barone, 1987, *Phys. Rev. B* **36**, 235.
- Gill, A.J. and T.W. Kibble, 1996, *J. Phys. A: Math. Gen.* **29**, 4289.
- Giovannini, M. and E.M. Shaposhnikov, 1997, *Phys. Rev. Lett.* **80**, 22.
- Goldner, L.S. and G. Ahlers, 1992, *Phys. Rev. B* **45**, 13129.
- Greywall, D.S., 1986, *Phys. Rev. B* **33**, 7520.
- Guillou, J.C. Le and J. Zinn-Justin, 1980, *Phys. Rev. B* **21**, 3976.
- Hanson, A.J. and T. Regge, 1978, *Torsion and quantum gravity*, in: *Proceedings of the Integrative Conference on Group Theory and Mathematical Physics*, University of Texas at Austin, 1978.
- Harari, D. and A.P. Polychronakos, 1988, *Phys. Rev. D* **38**, 3320.
- Heinilä, M. and G.E. Volovik, 1995, *Physica B* **210**, 300.
- Hindmarsh, M. and T. Kibble, 1995a, *Rep. Progr. Phys.* **58**, 477.
- Hindmarsh, M.B. and T.W.B. Kibble, 1995b, *Rep. Progr. Phys.* **58**, 477.
- Ho, T.-L., 1978, *Phys. Rev. B* **18**, 1144.
- Ibaceta, D. and E. Calzetta, 1999, *Phys. Rev. E* **60**, 2999.

- Iengo, R. and G. Jug, 1995, Phys. Rev. B **52**, 7537.
- Iordanskii, S.V., 1964, Ann. Phys. **29**, 335.
- Iordanskii, S.V., 1965, Zh. Exp. Teor. Fiz. **49**, 225; [Sov. Phys. JETP, **22**, 160 (1966)].
- Jensen, B. and J. Kuvcera, 1993, J. Math. Phys. **34**, 4975.
- Joyce, M. and M. Shaposhnikov, 1997, Phys. Rev. Lett. **79**, 1193.
- Kagan, Yu. and B.V. Svistunov, 1994, Zh. Exper. Teor. Fiz. **105**, 353; [Sov. Phys. JETP **78**, 187 (1994)].
- Kajantie, K., M. Karjalainen, M. Laine, J. Peisa and A. Rajantie, 1998, Phys. Lett. B **428**, 334.
- Kao, H.-C. and K. Lee, 1995, Phys. Rev. D **52**, 6050.
- Karra, G. and R.J. Rivers, 1998, Phys. Rev. Lett. **81**, 3707.
- Keto, J.W., F.J. Soley, M. Stockton and W.A. Fitzsimmons, 1974, Phys. Rev. A **10**, 872.
- Khazan, M.V., 1985, Pis'ma Zh. Eksp. Teor. Fiz. **41**, 396; [JETP Lett. **41**, 486 (1985)].
- Kibble, T.W., 1976, J. Phys. A **9**, 1387.
- Kibble, T.W. and G.E. Volovik, 1997, Pis'ma Zh. Exp. Teor. Fiz. **65**, 96; [JETP Lett. **65**, 102 (1997)].
- Kirtley, J.R., C.C. Tsuei, M. Rupp, J.Z. Sun, L.S. Yu-Jahnes, A. Gupta, M.B. Ketchen, K.A. Moler and M. Bhushan, 1996, Phys. Rev. Lett. **76**, 1336.
- Kita, T., 1999, Phys. Rev. Lett. **83**, 1846.
- Kleinert, H., 1989, Gauge Fields in Condensed Matter (World Scientific, Singapore).
- Kondo, Y., J.S. Korhonen, M. Krusius, V.V. Dmitriev, Yu.M. Mukharskiy, E.B. Sonin and G.E. Volovik, 1991, Phys. Rev. Lett. **67**, 81.
- Kondo, Y., J.S. Korhonen, M. Krusius, V.V. Dmitriev, E.V. Thuneberg and G.E. Volovik, 1992, Phys. Rev. Lett. **68**, 3331.
- Koplik, J. and H. Levine, 1993, Phys. Rev. Lett. **71**, 1375.
- Kopnin, N.B., 1978, Pis'ma Zh. Exp. Teor. Fiz. **27**, 417; [JETP Lett. **27**, 390 (1978)].
- Kopnin, N.B., 1993, Phys. Rev. B **47**, 14354.
- Kopnin, N.B., 1995, Physica B **210**, 267.
- Kopnin, N.B., G.E. Volovik and Ü. Parts, 1995, Europhys. Lett. **32**, 651.
- Kopnin, N.B. and M.M. Salomaa, 1991, Phys. Rev. B **44**, 9667.
- Kopnin, N.B. and E.V. Thuneberg, 1999, Phys. Rev. Lett. **83**, 116.
- Kopnin, N.B. and V.M. Vinokur, 1998, Phys. Rev. Lett. **81**, 3952.
- Kopnin, N.B. and G.E. Volovik, 1998, Phys. Rev. B **57**, 8526.
- Kopu, J., R. Schanen, R. Blaauwgeers, V.B. Eltsov, M. Krusius, J.J. Ruohio and E.V. Thuneberg, 2000, J. Low Temp. Phys., in press.
- Korhonen, J.S., A.D. Gongadze, Z. Janu, Y. Kondo, M. Krusius, Yu.M. Mukharskiy and E.V. Thuneberg, 1990, Phys. Rev. Lett. **65**, 1211.
- Korhonen, J.S., Y. Kondo, M. Krusius, E.V. Thuneberg and G.E. Volovik, 1993, Phys. Rev. B **47**, 8868.
- Krusius, M., E.V. Thuneberg and Ü. Parts, 1994, Physica B **197**, 376.
- Krusius, M., T. Vachaspati and G.E. Volovik, 1998, preprint cond-mat/9802005.
- Laguna, P. and W.H. Zurek, 1997, Phys. Rev. Lett. **78**, 2519.
- Landau, L. and E. Lifshitz, 1955, Dokl. Akad. Nauk. **100**, 669.
- Lee, K.-M., 1994, Phys. Rev. D **49**, 4265.
- Leggett, A.J., 1992, J. Low Temp. Phys. **87**, 571.
- Linde, A., 1990, Particle physics and inflationary cosmology (Harwood Acad. Publ., Switzerland).
- Lipa, J.A., D.R. Swanson, J.A. Nissen, T.C.P. Chui and U.E. Israelsson, 1996, Phys. Rev. Lett. **76**, 944.
- Lipa, J.A., D.R. Swanson, J.A. Nissen, P.R. Williamson, Z.K. Geng, D.A. Stricker, T.C.P. Chui, U.E. Israelsson and M. Larson, 1998, J. Low Temp. Phys. **113**, 849.
- London, H., 1946, in: Report of Intern. Conf. on Fund. Particles and Low Temp., Vol. II (Physical Society, London) p. 48.
- Lynden-Bell, D. and M. Nouri-Zonoz, 1998, Rev. Mod. Phys. **70**, 427.
- Makhlin, Yu.G. and G.E. Volovik, 1995, Pis'ma Zh. Exp. Teor. Fiz. **62**, 719; [JETP Lett. **62**, 737 (1995)].
- March-Russel, J., J. Preskill and F. Wilczek, 1992, Phys. Rev. D **50**, 2567.
- Mazur, P.O., 1986, Phys. Rev. Lett. **57**, 929.
- Mazur, P.O., 1987, Phys. Rev. Lett. **59**, 2380.
- Mazur, P.O., 1996, preprint hep-th/9611206.
- Mermin, N.D. and T.-L. Ho, 1976, Phys. Rev. Lett. **36**, 594.
- Meyer, J.S. and T. Sloan, 1997, J. Low Temp. Phys. **108**, 345.
- Mino, Y., M. Sasaki and T. Tanaka, 1997, preprint gr-qc/9705073.
- Misirpashaev, T. Sh., 1991, Sov. Phys. JETP **72**, 973.
- Naculich, S.G., 1995, Phys. Rev. Lett. **75**, 998.
- Nelson, D.R. and J.M. Kosterlitz, 1977, Phys. Rev. Lett. **39**, 1201.
- Nemirovskii, S.K. and W.M. Fiszdon, 1994, Physica B **197**, 290.
- Nikiforov, A.V. and E.B. Sonin, 1983, Zh. Eksp. Teor. Fiz. **85**, 642; [Sov. Phys. JETP **58**, 373 (1983)].
- Onsager, L., 1949, Nuovo Cimento **6**, Suppl. 2, 249.
- Onsager, L., 1954, (unpublished), see F. London, Superfluids, Vol. II, (John Wiley and Sons, Inc., New York) p. 151.
- Packard, R.E., 1998, Rev. Mod. Phys. **70**, 641; and references therein.
- Parts, Ü., Y. Kondo, J.S. Korhonen, M. Krusius and E.V. Thuneberg, 1993, Phys. Rev. Lett. **71**, 2951.
- Parts, Ü., E.V. Thuneberg, G.E. Volovik, J.H. Koivuniemi, V.M.H. Ruutu, M. Heinilä, J.M. Karimäki and M. Krusius, 1994, Phys. Rev. Lett. **72**, 3839.
- Parts, Ü., V.M. Ruutu, J.H. Koivuniemi, Yu.M. Bunkov, V.V. Dmitriev, M. Fogelström, M. Huebner, Y. Kondo, N.B. Kopnin, J.S. Korhonen, M. Krusius, O.V. Lounasmaa, P.I. Soininen and G.E. Volovik, 1995, Europhys. Lett. **31**, 449.
- Preskill, J., 1992, Phys. Rev. D **46**, 4218.
- Rajantie, A., 1998, Physica B **255**, 108.
- Rajantie, A., K. Kajantie, M. Karjalainen, M. Laine and J. Peisa, 1998, preprint hep-lat/9807042.
- Rivers, R.J., 2000, Phys. Rev. Lett. **84**, 1248.
- Roberge, A., 1989, Finite Density Effects in Gauge Theories, Ph. D. thesis, University of British Columbia.
- Ruutu, V.M., V.B. Eltsov, A.J. Gill, T.W. Kibble, M. Krusius, Yu.G. Makhlin, B. Plaçais, G.E. Volovik and Wen Xu, 1996a, Nature **382**, 334.
- Ruutu, V.M., Ü. Parts, B. Plaçais, Wen Xu, G.E. Volovik and M. Krusius, 1996b, Czechoslovak J. Phys. **46**, Suppl. S1, 15.

- Ruutu, V.M., Ü. Parts, J.H. Koivuniemi, N.B. Kopnin and M. Krusius, 1997a, *J. Low Temp. Phys.* **107**, 93.
- Ruutu, V.M.H., J. Kopu, M. Krusius, U. Parts, B. Plaçaais, E.V. Thuneberg and Wen Xu, 1997b, *Phys. Rev. Lett.* **79**, 5058.
- Ruutu, V.M., V.B. Eltsov, M. Krusius, Yu.G. Makhlin, B. Plaçaais and G.E. Volovik, 1998a, *Phys. Rev. Lett.* **80**, 1465.
- Ruutu, V.M., J.J. Ruohio, M. Krusius, B. Plaçaais and E.B. Sonin, 1998b, *Physica B* **255**, 27.
- Salomaa, M.M. and G.E. Volovik, 1987, *Rev. Mod. Phys.* **59**, 533.
- Salomaa, M.M. and G.E. Volovik, 1989, *J. Low Temp. Phys.* **74**, 319.
- Samuels, D.C., 1992, *Phys. Rev. B* **46**, 11714.
- Schiffer, P., M.T. O'Keefe, M.D. Hildreth, H. Fukuyama and D.D. Osheroff, 1992, *Phys. Rev. Lett.* **69**, 120.
- Schiffer, P.E., D.D. Osheroff and A.J. Leggett, 1995, in: *Prog. Low Temp. Phys.*, Vol. XIV, ed W. Halperin (Elsevier Science B. V., Amsterdam) p. 159; and references therein.
- Schiffer, P. and D.D. Osheroff, 1995, *Rev. Mod. Phys.* **67**, 491.
- Schwarz, A.S., 1982, *Nucl. Phys. B* **208**, 141.
- Schwarz, K.W., 1978, *Phys. Rev. B* **18**, 245.
- Schwarz, K.W., 1985, *Phys. Rev. B* **31**, 5782.
- Schwarz, K.W., 1988, *Phys. Rev. B* **38**, 2398.
- Shelankov, A., 1998a, preprint cond-mat/9802158.
- Shelankov, A., 1998b, *Europhys. Lett.* **43**, 623.
- Shung, E., T.F. Rozenbaum and M. Sigrüst, 1998, *Phys. Rev. Lett.* **80**, 1078.
- Sigrüst, M., 1989, *Phys. Rev. Lett.* **63**, 1727.
- Sigrüst, M., T.M. Rice and K. Ueda, 1989, *Phys. Rev. Lett.* **63**, 1727.
- Sigrüst, M., D.B. Bailey and R.B. Laughlin, 1995, *Phys. Rev. Lett.* **74**, 3249.
- Sokolov, D.D. and A.A. Starobinsky, 1977, *Doklady AN SSSR* **234**, 1043; [*Sov. Phys. — Doklady*, **22**, 312 (1977)].
- Sonin, E.B., 1975, *Zh. Exp. Teor. Fiz.* **69**, 921; [*Sov. Phys. JETP* **42**, 469 (1976)].
- Sonin, E.B., 1997, *Phys. Rev. B* **55**, 485.
- Sonin, E.B., V.H. Geshkenbein, A. van Otterlo and G. Blatter, 1998, *Phys. Rev. B* **57**, 575.
- Starkman, G.D., 1996, *Phys. Rev. D* **53**, 6711.
- Staruszkiewicz, A., 1963, *Acta Phys. Polon.* **24**, 734.
- Stockton, M., J.W. Keto and W.A. Fitzsimmons, 1971, *Phys. Rev. A* **5**, 372.
- Stone, M., 1996, *Phys. Rev. B* **54**, 13222.
- Tang, Y.H., I. Hahn, H.M. Bozler and C.M. Gould, 1991, *Phys. Rev. Lett.* **67**, 1775.
- Thorne, K.S. and J.B. Hartle, 1985, *Phys. Rev. D* **31**, 1815.
- Thuneberg, E.V., 1986, *Phys. Rev. Lett.* **56**, 359.
- Tough, J.T., 1982, in: *Prog. Low Temp. Phys.*, Vol. XIII, ed W. Halperin (Elsevier Science B. V., Amsterdam) p. 133; and references therein.
- Toyoki, H., 1994, *J. Phys. Soc. Japan* **63**, 446.
- Trebin, H.-R. and R. Kutka, 1995, *J. Phys. A: Math. Gen.* **28**, 2005.
- Tsubota, M. and H. Yoneda, 1995, *J. Low Temp. Phys.* **101**, 815.
- Unruh, W.G., 1976, *Phys. Rev. D* **14**, 870.
- Vachaspati, T., 1994, in: *Proc. NATO Workshop "Electroweak Physics and the Early Universe"*, Sintra, Portugal, Vol. 338 of Series B: Physics (Plenum Press, New York).
- Vachaspati, T. and G.B. Field, 1994, *Phys. Rev. Lett.* **73**, 373.
- Vachaspati, T. and G.B. Field, 1995, *Phys. Rev. Lett.* **74**, 1258.
- Vachaspati, T. and A. Vilenkin, 1984, *Phys. Rev. D* **30**, 2036.
- van Otterlo, A., M.V. Feigel'man, V.B. Geshkenbein and G. Blatter, 1995, *Phys. Rev. Lett.* **75**, 3736.
- Varoquaux, E., O. Avenel, P. Hakonen and Yu. Mukharsky, 1998, *Physica B* **255**, 55; and references therein.
- Vollhardt, D. and P. Wölfle, 1990, *The Superfluid Phases of Helium 3* (Taylor & Francis).
- Volovik, G.E., 1990, in: *Helium Three*, eds W. Halperin and L. Pitaevskii (Elsevier Science B. V., Amsterdam) p. 27.
- Volovik, G.E., 1992a, *Physica B* **178**, 160.
- Volovik, G.E., 1992b, *Exotic Properties of Superfluid <sup>3</sup>He* (World Scientific, Singapore).
- Volovik, G.E., 1996, *Czechoslovak J. Phys.* **46**, Suppl. S6, 3048.
- Volovik, G.E., 1997, *Pis'ma Zh. Exp. Teor. Fiz.* **65**, 201; [*JETP Lett.* **65**, 217 (1997)].
- Volovik, G.E., 1998, *Physica B* **255**, 86.
- Volovik, G.E. and L.P. Gor'kov, 1984, *Pis'ma Zh. Eksp. Teor. Fiz.* **39**, 550; [*JETP Lett.* **39**, 674 (1984)].
- Volovik, G.E. and V.P. Mineev, 1977, *Zh. Eksp. Teor. Fiz.* **72**, 2256; [*Sov. Phys. JETP* **45**, 1186 (1977)].
- Volovik, G.E. and V.P. Mineev, 1982, *Zh. Exp. Teor. Fiz.* **83**, 1025; [*Sov. Phys. JETP* **56**, 579 (1982)].
- Volovik, G.E. and T. Vachaspati, 1996, *Int. J. Mod. Phys. B* **10**, 471.
- Weinberg, S., 1996, *The Quantum Theory of Fields* (Cambridge University Press, Cambridge, UK).
- Wexler, C., 1997, *Phys. Rev. Lett.* **79**, 1321.
- Wexler, C. and D.J. Thouless, 1996, preprint cond-mat/9612059.
- Wheatley, J.C., 1975, *Rev. Mod. Phys.* **47**, 415.
- Wilczek, F., 1998a, *Nucl. Phys. A* **642**, 1.
- Wilczek, F., 1998b, *Physics Today* **51**, N1 (January), 11.
- Williams, G.A., 1993a, *Phys. Rev. Lett.* **71**, 392.
- Williams, G.A., 1993b, *J. Low Temp. Phys.* **93**, 1079.
- Williams, G.A., 1999, *Phys. Rev. Lett.* **82**, 1201.
- Witten, E., 1985, *Nucl. Phys. B* **249**, 557.
- Xu, Wen, B. Plaçaais, V.M. Ruutu and M. Krusius, 1996, *Czechoslovak J. Phys.* **46**, Suppl. S1, 11.
- Yates, A. and W.H. Zurek, 1998, *Phys. Rev. Lett.* **80**, 5477.
- Ying, S., 1998, *Ann. Phys.* **266**, 295.
- Zapotocky, M., P.M. Goldbart and N. Goldenfeld, 1995, *Phys. Rev. E* **51**, 1216.
- Zhang, X., T. Huang and R.H. Brandenberger, 1998, *Phys. Rev. D* **58**, 027702.
- Zurek, W.H., 1985, *Nature* **317**, 505.
- Zurek, W.H., 1996, *Phys. Rep.* **276**, 177.